STUDY ON THE GROWTH OF NiSi/SiC CORE – SHELL NANOWIRES BY HOT – WIRE CHEMICAL VAPOR DEPOSITION AND ITS APPLICATION IN SUPERCAPACITOR

NAJWA BINTI HAMZAN

FACULTY OF SCIENCE
UNIVERSITY OF MALAYA
KUALA LUMPUR

2017

University of Malaya

STUDY ON THE GROWTH OF NiSi/SiC CORE - SHELL NANOWIRES BY HOT – WIRE CHEMICAL VAPOR DEPOSITION AND ITS APPLICATION IN SUPERCAPACITOR

NAJWA BINTI HAMZAN

DISSERTATION SUBMITTED IN FULFILMENT OF THE REQUIREMENTS FOR THE DEGREE OF MASTER OF SCIENCE

DEPARTMENT OF PHYSICS
FACULTY OF SCIENCE
UNIVERSITY OF MALAYA
KUALA LUMPUR

2017

University of Malaya

UNIVERSITY OF MALAYA

ORIGINAL LITERARY WORK DECLARATION

Name of Candidate : **NAJWA BINTI HAMZAN**

I.C/Passport No :

Matric No : **SGR 130117**

Name of Degree : **MASTER OF SCIENCE**

Title of Project Paper/Research Report/Dissertation/Thesis ("this Work"):

" STUDY ON THE GROWTH OF NiSi/SiC CORE – SHELL NANOWIRES BY HOT – WIRE CHEMICAL VAPOR DEPOSITION AND ITS APPLICATION IN SUPERCAPACITOR"

Field of Study: **NANOMATERIALS**

I do solemnly and sincerely declare that:

(1) I am the sole author/writer of this Work;
(2) This Work is original;
(3) Any use of any work in which copyright exists was done by way of fair dealing and for permitted purposes and any excerpt or extract from, or reference to or reproduction of any copyright work has been disclosed expressly and sufficiently and the title of the Work and its authorship have been acknowledged in this Work;
(4) I do not have any actual knowledge nor do I ought reasonably to know that the making of this work constitutes an infringement of any copyright work;
(5) I hereby assign all and every rights in the copyright to this Work to the University of Malaya ("UM"), who henceforth shall be owner of the copyright in this Work and that any reproduction or use in any form or by any means whatsoever is prohibited without the written consent of UM having been first had and obtained;
(6) I am fully aware that if in the course of making this Work I have infringed any copyright whether intentionally or otherwise, I may be subject to legal action or any other action as may be determined by UM.

Candidate's Signature Date:

Subscribed and solemnly declared before,

Witness's Signature Date:

Name:

Designation:

University of Malaya

ABSTRACT

This work reports on the investigation of NiSi/SiC core – shell nanowires grown by hot – wire chemical vapor deposition technique on crystalline Si (c-Si) and Ni foil substrates. This work was divided into two parts. In the first part, the effect of different substrate temperatures (350°C to 530°C) on growth and structural properties of the nanowires were studied with SiH_4 to CH_4 gas flow rates fixed at 1:2. These core-shell nanowires were found to be grown at substrate temperatures above 350°C. The nanowires consisted of single crystalline NiSi core and polycrystalline SiC nanocolumn shell. Increase of the substrate temperature enhances the growth of high density vertically aligned nanowires with increment of 2%. The electrochemical properties of NiSi/SiC core-shell nanowires also have been investigated. The specific capacitance of the NiSi/SiC core-shell nanowires obtained from the cyclic voltammetry curve was about 75 mF/cm^2, which was nearly three times higher than the intrinsic NiSi nanowires (21 mF/cm^2) and four times higher than the blank Ni foil (17 mF/cm^2). In the second part, the effects of different CH_4 flow rate (0.5 sccm to 3.5 sccm) on the growth, structural and electrochemical properties of the nanowires were investigated. The nanowires were found to be grown at CH_4 flow rate above 0.5 sccm. The microstructures studies of these nanowires have demonstrated a single crystalline NiSi core and polycrystalline SiC nanocolumn shell, respectively. In addition, CH_4 flow rates also affect the diameter of core and thickness of shell of nanowires.The diameter of core and thickness of shell of nanowires noticeably increased with the increased in CH_4 flow rates from 0.5 sccm to 3.5 sccm. The diameter of core of nanowire increased from 19.48 nm to 20.00 nm while thickness of shell of nanowire increased from 54.58 nm to 120.00 nm. The NiSi/SiC core-shell nanowire electrode at 2.0 sccm exhibited an excellent electrochemical performance as compared to other flow rates. The core - shell nanowire electrode has achieved a maximum specific capacitance of 234.13 mF/cm^2.

University of Malaya

ABSTRAK

Kerja ini membincangkan penyiasatan ke atas NiSi/SiC teras – kulit nanowayar yang telah dihasilkan dengan menggunakan teknik wayar – panas pemendapan wap kimia ke atas hablur Si dan kertas logam Ni. Kerja ini telah dibahagikan kepada dua bahagian. Pada bahagian pertama, kesan suhu substrat yang berbeza (350°C ke 530°C) ke atas pertumbuhan dan sifat-sifat struktur nanowayar telah dikaji dengan SiH_4 kepada aliran CH_4 telah ditetapkan pada nisbah kadar 1:2. Nanowayar teras – kulit telah didapati ditanam pada suhu substrat 350°C ke atas. Nanowayar ini terdiri daripada hablur tunggal NiSi teras dan polihabluran SiC teras turusnano. Peningkatan suhu substrat meningkatkan lagi pertumbuhan nanowayar berkepadatan tinggi secara menegak sejajar dengan tambahan sebanyak 2%. Sifat-sifat elektrokimia NiSi/SiC teras – kulit nanowayar juga telah disiasat dalam kajian ini. Kapasitan khusus NiSi/SiC teras – kulit nanowayar diperolehi daripada lengkung votammetri kitaran adalah kira-kira 75 mF/cm^2, iaitu hampir tiga kali lebih tinggi daripada nanowayar NiSi intrinsic (21 mF/cm^2). Pada bahagian kedua, kesan daripada kadar aliran CH_4 yang berbeza (0.5 sccm ke 3.5 sccm) ke atas pertumbuhan, sifat-sifat struktur dan elektrokimia nanowayar telah dikaji. Nanowayar didapati tumbuh pada kadar aliran 0.5 sccm ke atas. Kajian mikrostruktur nanowayar ini menunjukkan nanowayar terdiri daripada hablur tunggal NiSi teras dan polihabluran teras SiC turusnano. Disamping itu, kadar aliran CH_4 juga member kesan ke atas diameter teras dan ketebalan kulit nanowayar. Peningkatan kadar aliran CH_4 dari 0.5 sccm ke 3.5 sccm, meningkatkan lagi diameter teras dan ketebalan kulit nanowayar. Diameter teras nanowayar meningkat dari 19.48 nm kepada 20.00 nm sementara ketebalan teras nanowayar meningkat dari 54.58 nm ke 120.00 nm. NiSi/SiC teras – kulit nanowayar elektrod pada 2.0 sccm menunjukkan kecermerlangan prestasi elektrokimia berbanding aliran yang lain. NiSi/SiC teras-kulit nanowayar pada 2.0 sccm telah mencapai kapasitan khusus yang maksimum pada 234.13 mF/cm^2.

University of Malaya

ACKNOWLEDGEMENTS

In the name of Allah, the most gracious, the most merciful. All praise and thanks to Allah, the Lord of existence, for the strength, patience, faith and bless to make the completion of this dissertation come true.

First and foremost, special thanks to my beloved parents, En. Hamzan bin Abd Aziz and Pn. Salmiyah binti Mohd Yunan, for their love, support, encouragement and endless prayers.

I wish to extend my sincere gratitude and appreciation to my supervisor Dr Goh Boon Tong and Dr Huang Nay May for their guiding and advising throughout this work. Their continuous support and encouragement are important for me to accomplish any work done in this thesis.

I also would like to thank all the members of low Dimensional Materials Research Centre, Department of Physics in University of Malaya for helping me during my experiments. Thank you for guiding me, gives suggestions and ideas for my research report.

This work was supported by Ministry of higher Education of Malaysia, for Exploratory Research Grant Scheme (ERGS) of ER003-2013 and also Postgraduate Research Grant (PPP) of PG084-2014A.

University of Malaya

TABLE OF CONTENTS

University of Malaya

University of Malaya

University of Malaya

University of Malaya

LIST OF FIGURES

University of Malaya

University of Malaya

University of Malaya

University of Malaya

University of Malaya

University of Malaya

LIST OF TABLES

University of Malaya

LIST OF SYMBOLS AND ABBREVIATIONS

C : Carbon

Cu : Copper

c-Si : Crystal Silicon

CH_4 : Methane

CVD : Chemical Vapor Deposition

DI : Deionized

EDX : Energy-Dispersion X-ray Spectroscopy

FWHM : Full Width Half Maximum

FESEM : Field Scanning Electron Microscopy

H_2 : Hydrogen

HRTEM : High Resolution Transmission Electron Microscopy

LA : Longitudinal Acoustic

LO : Longitudinal Optic

MFC : Mass Flow Controller

rf : Radio Frequency

sccm : Standard Cubic Centimeters Per Minute

SiH_4 : Silane

TEM : Transmission Electron Microscopy

t_d : Deposition Time

T_s : Substrate Temperature

University of Malaya

LIST OF APPENDICES

University of Malaya

CHAPTER 1: INTRODUCTION

1.1 Background

Since the discovery of carbon nanotubes in 1991 by Iijima, one dimensional (1D) nanostructures such as nanowires and nanorods have received much attention due to their potential applications as the building blocks of nanoscale devices. These 1D semiconductor nanostructures mostly Si-based nanowires and nanorods have demonstrated outstanding physical, mechanical, chemical, optical, and electrical properties (Chen et al., 2013; Weng et al., 2014; Yu et al., 2009). These unique and excellent properties have enabled Si-based nanowires to achieve excellent performance in solar cells, thermoelectric devices, photoelectronics, and energy storage devices mainly of lithium-ion batteries and supercapacitors (Liu et al., 2010; Long et al., 2012).

Among various energy storage devices, the supercapacitors also called electrochemical capacitors (ECs), have attracted much attention among others energy storage devices due to their excellent performance such as high power densities (>10 kW/kg), long cycles lives (>10^6 cycles) and a wide range of working temperatures (-70 to +100°C) (Korenblit et al., 2012; Lin et al., 2011). Figure 1.1 shows the Ragone plot of power density versus energy density for the most important energy storage systems. Fuel cells and batteries are often considered to be high-energy systems, while ECs (also known as supercapacitors or ultracapacitors) and conventional electrostatic capacitors are considered to be high-power systems. Based on this figure, it's clearly shows that the electrochemical capacitors fill the gap between batteries and conventional solid state and electrolytic capacitors. They store hundreds or thousands of times more charge. Though, they have lower in energy density (5-10Wh/kg) than batteries (100-250 Wh/kg), ECs can provide the ability to store and release the energy within time frame of a few seconds, compared to tens of minutes or more needed to charge/discharge for batteries (Service, 2006).

University of Malaya

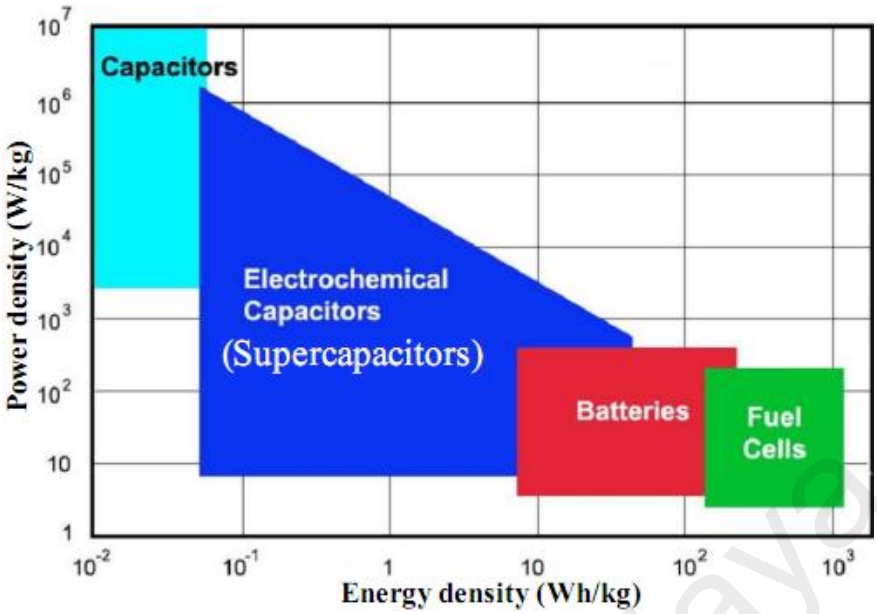

Figure 1.1: Ragone plot for various electrical energy storage devices. (Service, 2006)

In the past decade, carbon materials such as activated carbon (Fang & Binder, 2006), carbon nanofibers (Yuan et al., 2011), carbon nanotubes (Masarapu et al., 2009), and graphene (Hsia et al., 2014), and transition metal oxides/hydroxides (Cao et al., 2004) have been widely studied as electrode materials for supercapacitors due to their high specific surface areas, low cost and excellent conductivity. However, these electrode materials generally suffer several drawbacks which resulting to the reduction in their device performances and efficiencies. For instance, carbon materials have low energy density and easily to oxidize at high operating temperatures with a presence of oxygen ambient severely limits their practical applications (Yu et al., 2013). In addition, they also suffer from the drawback of costly and tedious fabrication processes that restrict its commercial application. For transition metal oxides/hydroxides electrodes, they have relatively low power density and poor cycling stability due to inadequate conductivity, and those electrodes normally encounter a degradation of electroactive materials during Faradic redox reactions thereby reducing the life cycles of the devices (Shi et al., 2014).

University of Malaya

Among inorganic semiconductor material, silicon carbide (SiC) is well known to be a stable material in many harsh physicochemical environments, includes high temperature oxidizing environment, high pressure and high power as well as space environments (Maboudian et al., 2013). SiC nanowires also have been widely reported for their excellent properties such as superior mechanical properties, high thermal conductivity, low thermal-expansion coefficient, good thermal-shock resistance, as well as its chemical stability and electron affinity, which allow them to be an excellent candidate that can be used in supercapacitors (Gu et al., 2015; Hu et al., 2016; Zhuang et al., 2015). Because of its excellent electrochemical performance, high surface area and compatibility with various electrolytes, SiC supercapacitor electrodes with different morphology and structure had shown high surface efficiency, rate capability and cycle lifetime based on previous reports. For example, Yang et al. (2012) demonstrated that the nanaocrystalline 3C-SiC films synthesized by microwave plasma CVD technique have the potential to be used as an electrode material for electrochemical applications. They shows a wide potential window (-1 to 3V), a low and stable capacitance current with repeated sweeps. Moreover, Chen et al. (2014) reported the high purity and uniformity of 3C–SiC nanowire film with film thickness of 100-200 μm. The 3C-SiC nanowires film was grown on graphite paper by carbothermal reduction method showing specific capacitance were 25.6 mF/cm^2 at 0.2 A/cm^2.

The use of 1D nanostructures as the electrodes of supercapacitors has drawn great attention recently because they can provide short diffusion path lengths for ions, leading to high charge–discharge rates (Li et al., 2014; Zhang et al., 2012). Compared with the single-phase intrinsic nanostructures, the 1D core-shell nanostructures have attracted more attention because of their ability to improve the electrochemical performance of the electrode through fast ion diffusion, stress relaxation and electron and mass transport (Huang et al., 2013). Generally, the core materials would create stable and

University of Malaya

efficient pathways for electron transport while the shell materials can significantly increase the surface area and provide more electrochemical active sites (Huang et al., 2014; Zhang et al., 2015). As a result such core-shell nanowires can shorten the distance for electrolyte ion diffusion and open up more efficient pathways for electron transport (Wang et al., 2014). However, in the core-shell structure, the active sites of core nanowires are largely invalidated by the shell layer, which prevents full utilization of the electrochemical reactivity of the core nanowires. Hence, shell thickness plays a vital role in order to provide better facile access for electrolyte ions in which can improve the electrochemical performance of the nanowires. Thus, proper control of the microstructure and the thickness of the shell are absolutely required to extract superior performance from the capacitor (Soam et al., 2016; Zou et al., 2015).

Choudhary et al. (2016) reported that, rational structure design of electrode also plays an important role to its electrochemical performance. Direct growth of nanowires (active electrode materials) on metallic substrates such as Ni foil (current collectors) can also enhance mechanical robustness while reducing capacitive loss at their interfaces. Moreover, based on their research, growth of nanowires on metallic substrates can enlarged the surface area of electrodes eventually lead to improved specific capacitance owing to the increased amount of charges store on their surfaces.

1.2 Problem statement

Although SiC nanowires have been extensively studied as one of the most promising active materials for supercapacitors, it still suffers from several drawbacks due to its intrinsic single-phase properties such as poor electrical conductivity, low ionic transport rate. These disadvantages had made the SiC nanowire electrode facing a low rate of capability and a poor cycling stability (Wang et al., 2014). In addition, based on the previous researches, the SiC nanowires also exhibited remarkably low specific capacitance at 0.4 $mFcm^{-2}$, 0.092 $mFcm^{-2}$, and 0.24 mF/cm^2 (Alper et al., 2013; Chang

University of Malaya

et al., 2015; Vincent et al., 2012). Such low capacitance severely limits their energy storage capacity and also rate of capability (Kim & Kim, 2014).

Besides that, according to Soam et al. (2016), for the core-shell structure, the electrical properties of the shell inherently contribute to the resultant electrical conductivity of core nanowire and thus playing a decisive role on the capacitance value for a given single-crystalline core diameter. Hence, the larger thickness of the shell causes a significant potential drops across it owing to its poor electrical conductivity, thereby leading to the low value of the capacitance.

1.3 Motivations of This Research

In order to overcome all the limitation intrinsic single-phase SiC nanowires, growth of hybrid core-shell nanowires has been considered as one of the effective strategies to enhance the electrochemical performance of the nanowires. The hybrid core-shell nanowires can shorten the distance for electrolyte ion diffusion and open up more efficient pathways for electron transport which can enhance the electrochemical performance of supercapacitors (Fu et al., 2016).

Alper et al. (2012), fabricated Si nanowires coated with SiC as micro-supercapacitor electrodes through the low-pressure CVD method enabling the electrodes to achieve a capacitance value of up to 1.7 mF/cm^2 while Zhang et al. (2015) synthesized SiC@SiO_2 nanocables/MnO_2 core-shell structures which showed the highest specific capacitance at 15 mF/cm^2. These results remarkably show higher specific capacitance over the single SiC nanowires.

In this research, the incorporation of highly metallic properties of single-crystalline NiSi nanowires as core electrodes into the NiSi/SiC core-shell is expected to enhance their electrical properties. The highly metallic characteristic of NiSi core electrodes could be used as current collector that creates an effective conductive pathway for electron transport between the SiC shell. NiSi/SiC core-shell nanowires were

University of Malaya

synthesized by using HWCVD technique. This is because the HWCVD technique is one of the most promising techniques for the low- temperature, high deposition rate and large-area deposition of SiC based thin film materials (Agarwal, 2015; Nazarudin et al., 2015).

To enhance the supercapacitor performance, proper control of the microstructure and the thickness of the core and shell of the nanowires are absolutely required to extract superior performance from the capacitor. Thus, different parameters were used in this research in order to enhance the supercapacitor performances of the nanowires. In addition, direct growth of nanowires on Ni foils substrate that acts as current collectors can also enhanced mechanical robustness while reducing capacitive loss at their interfaces.

1.4 Objectives of This Research

The research objectives can be summarized clearly as follows:

1. To investigate the effects of substrate temperature and CH_4 flow rate on the morphological, microstructure, crystallinity and structural properties of NiSi/SiC core-shell nanowires.
2. To propose the growth mechanism of NiSi/SiC core-shell nanowires.
3. To determine the supercapacitor performances of NiSi/SiC core-shell nanowires.

1.5 Overview of Thesis

The thesis is written in five chapters; literature review (Chapter 2), preparation of NiSi/SiC core-shell nanowires (Chapter 3), results of each characterization on the NiSi/SiC core-shell nanowires accompanied by discussion (Chapters 4), and wind up with conclusion and suggestions for future works (Chapter 5).

Chapter 1 presents a brief introduction to this research work then followed by Chapter 2 which highlights literature reviews related to this study. Details about setup

University of Malaya

of the home-built hot-wire CVD system and operating procedures of the system for NiSi/SiC core-shell NWs for deposition are demonstrated in Chapter 3. Chapter 4 discusses the results of morphological, structural and supercapacitor properties of NiSi/SiC core-shell nanowires deposited by hot-wire CVD system at different deposition conditions. The factors that influence the supercapacitor performance also fully described in this chapter. Finally, conclusion and suggestions for future work are presented.

University of Malaya

CHAPTER 2: LITERATURE REVIEW

2.1 Nanowires

2.1.1 Introduction

Nanowires constituted of an important class of 1D nanostructures which provide models to study the relations between electrical transport, optical and other properties with dimensionality and size confinement (Philip, 2011). They are also expected to play important roles as interconnects and functional components in the fabrication of nanoscale electronic, and optoelectronic devices and electrochemical applications. Nanowires refer to one-dimensional wire, rod, tip, whisker and cone-like structures with diameter of less than 100 nm (Yan et al., 2009). Many different types of nanowires exist including metallic (e.g., Ni, Ag or different alloys based on metals), semiconducting (e.g., Si, GaN, etc), insulating (e.g., SiO_2 and TiO_2) and molecular nanowires (e.g., organic DNA or inorganic) (Lefèvre, 2012).

Figure 2.1 show FESEM images of different types of nanowires. Figure 2.1(a) shows FESEM image of Ag nanowires with length of ~15 μm and diameter of 60–100 nm while Figure 2.1(b) depicts the FESEM image of Si nanowires obtained from Ni/SiO_2 blocks. The straight nanowires have wide diameter distributions ranging from 80 to 350 nm. Figure 2.1(c) illustrates the FESEM image of vertical organic nanowires of diaminoanthraquinone (DAAQ) molecules with lengths between 3 μm and 6 μm and diameters between 200 nm and 400 nm while Figure 2.1(d) demonstrated the top-view SEM image of typical morphology of SiO_2 nanowires with diameters ranging from 20 to 40 nm and lengths above 10 μm.

Among the various types of nanowires, semiconductor nanowires have been studied extensively for over two decades for their novel electronic, photonic, thermal, electrochemical and mechanical properties. Their ability to be integrated into electronic devices and to interface with other microscopic and nanoscopic systems in nature, and

University of Malaya

their high surface-to-volume ratio, have led them into various sensing, optoelectronic and energy storage applications by utilizing their unique 1D structures (Chikkaraddy et al., 2016). Figure 2.2 shows a significant increasing in the development of semiconductor nanowires research with nearly an exponential increase in the record of publications.

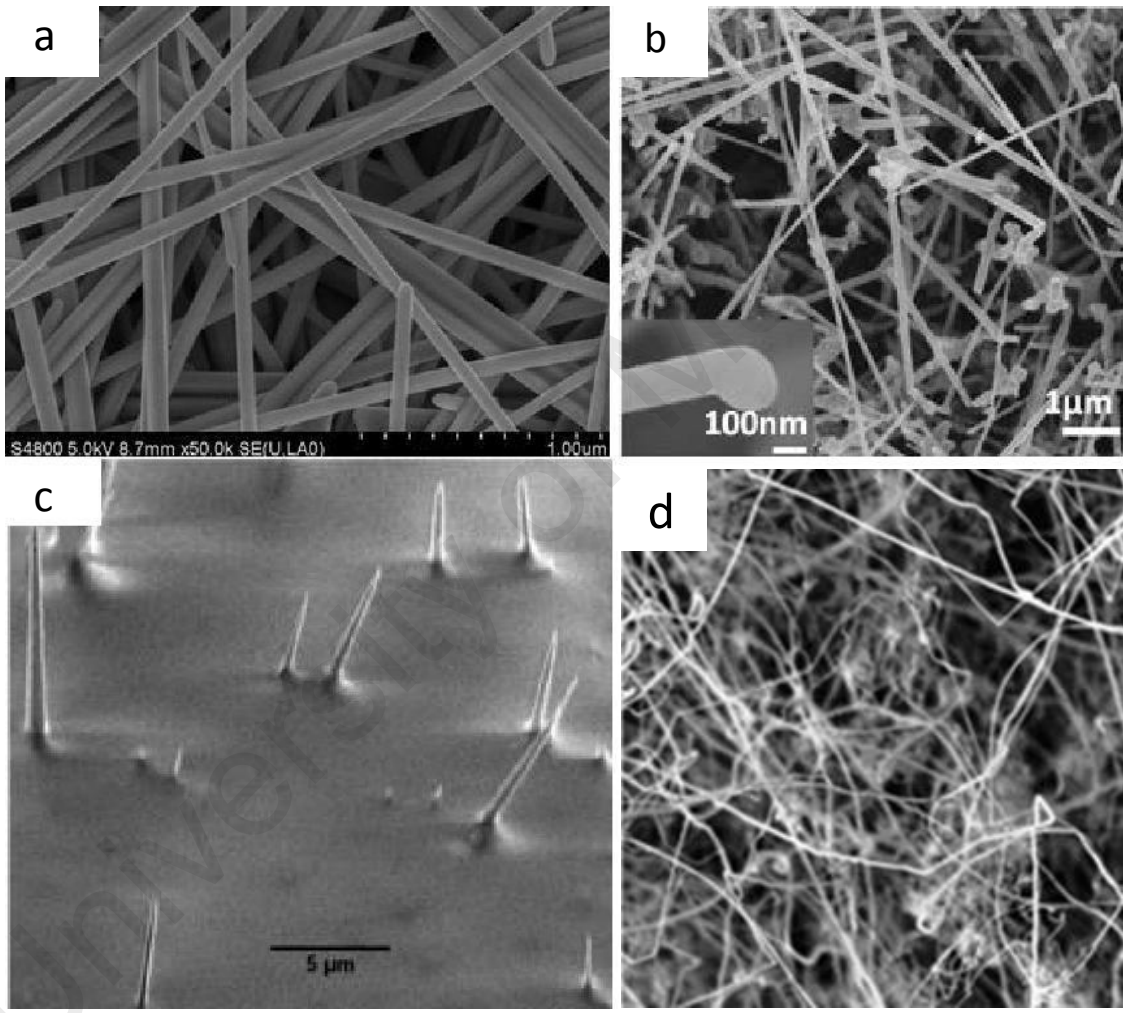

Figure 2.1: FESEM images of (a) Ag nanowires. (b) Si nanowires. (c) Vertical organic nanowires of diaminoanthraquinone (DAAQ) molecules. (d) SiO_2 nanowires. (Chikkaraddy et al., 2016; Fang et al., 2016; Gomez-Martinez et al., 2016; Zhu et al., 2016)

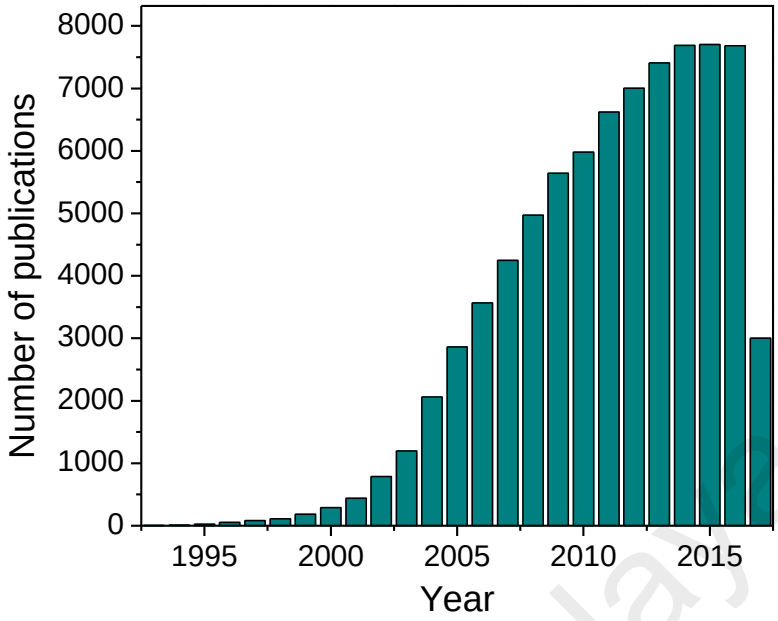

Figure 2.2: Number of publications by year to "nanowire(s) from 1995–2017. (Data extracted on 15th June 2017 through the Institute of Scientific Information (ISI) database)

2.2 Growth Mechanism Models

In order to study various properties of nanowires and their application in different fields and industries, several challenges have to be addressed. The main challenges in application of nanostructures are the controlled synthesis with controlled size, morphology, microstructure and chemical composition. In order to achieve this, comprehensive literature reviews on the growth mechanisms of nanowires are essentially important.

2.2.1 Vapor-Liquid-Solid (VLS)

The VLS mechanism is a 1D crystal growth mechanism that is assisted by a metal catalyst. It results in the creation of whiskers, rods, and wires. The VLS mechanism was proposed in 1964 by Wagner and Ellis as an explanation for silicon whisker growth from the gas phase in the presence of liquid gold droplets that formed on top surface of silicon substrate (Yang et al., 2015). The widely used VLS growth mechanism provides a direct control of nanowire diameter and length, and can be applied to a variety of

University of Malaya

materials including single and compound semiconductors from the group IV, III–V, and II–VI systems (Choi, 2012).

A lot of research conducted about this mechanism. For instance, in 1992, Hiruma and co-workers showed that the VLS growth mechanism could produce semiconductor crystals with nanoscale diameters, or nanowires (Wang et al., 2006). Shortly thereafter in 1997, Westwater and co-workers grew Si nanowires with diameters of tens of nanometers and lengths up to tens of microns using VLS growth mechanism (Wiesmann et al., 1979). A year later, Morales and Lieber used laser ablation to grow very small diameter Si and Ge nanowire diameters using Fe catalysts. This latter reported catalyzed a rapid expansion in nanowire research that was motivated in part by the potential advantages of highly scaled 1D semiconductors in device applications (Fan et al., 2006). The principle of Si whisker growth was schematically explained by Wang et al. (2008) as shown in Figure 2.3(a). At first, the Au particles deposited on the surface of a Si substrate react with vapor phase Si to form Au-Si alloy droplets at certain temperature. As shown in the Au-Si phase diagram in Figure 2.3(b), the melting temperature of the Au-Si alloy at the eutectic point was very slow (about 363°C) compared with that of Au or Si. In the case of Si deposition from vapor mixture of $SiCl_4$ and H_2, the reaction between SiH_4 and H_2 happens when temperature was higher than the 800°C without the assistance of catalyst. Below this temperature, almost no deposition of Si occurs on the substrate surface.

When the temperature above the eutectic temperature (363°C), the Au particles form Si-Au eutectic droplets on the Si surfaces, and the reduction of Si occurs at the Au-Si droplets due to a catalytic effect. The Au-Si droplets absorb Si from the vapor phase resulting in a supersaturated state. Since the melting point of Si was at 1414°C which much higher than eutectic temperature of Au-Si alloy at 363°C, Si atom precipitate from the supersaturated droplets and bond at the liquid-solid interface, and the liquid droplet

University of Malaya

rises from the Si substrate surface. The absorption, diffusion and precipitation processes of Si as schematically showed by the path 1, 2, and 3 as shown in Figure 2.3(c).

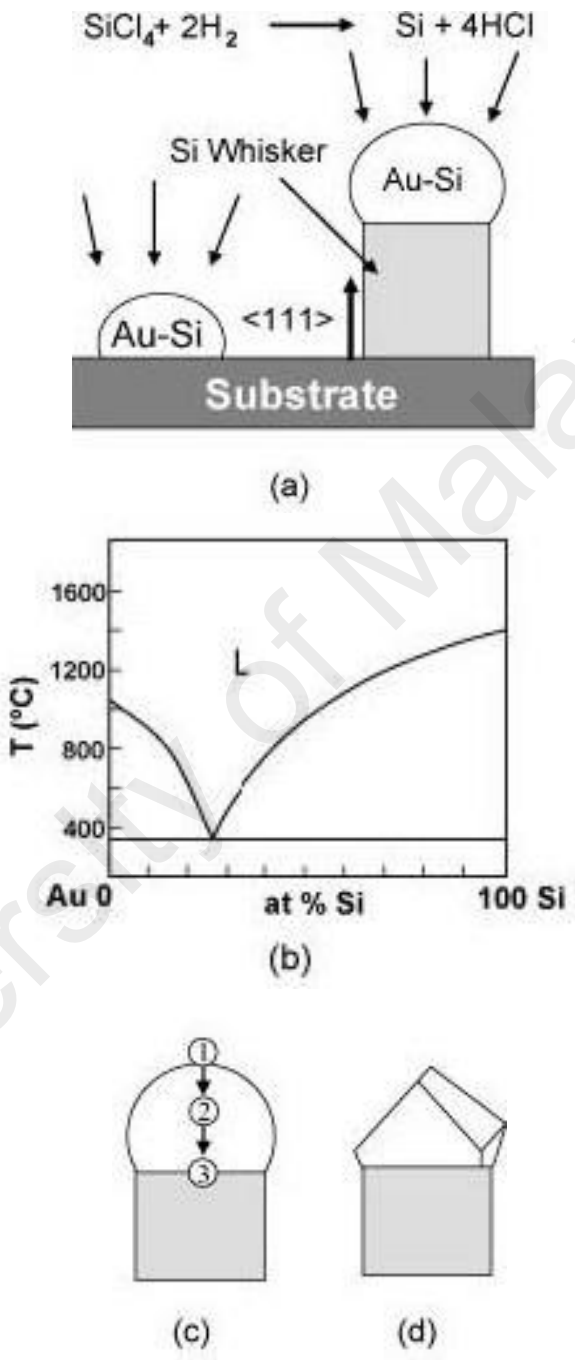

Figure 2.3: Schematic illustration of Si whisker growth from vapor phases via Au–Si catalytic droplets: (a) The Au–Si droplet formed on a Si substrate. (b) The Au–Si phase diagram. (c) The diffusion path of the source materials through a metal droplet. (d) The whisker growth can be catalyzed with a solid catalyst. (Wang et al., 2006)

University of Malaya

2.2.2 Vapor-Solid-Solid (VSS)

Initially, the study of VLS mechanism used Au as a catalyst for growth of nanowires especially Si and Ge nanowires due to its low eutectic temperatures. However, the adverse influence of Au on the electrical properties of Si and Ge has motivated research into alternative catalyst metals such as Pt, Ag, Pd, Cu and Ni (Kamins et al., 2000; Kang et al., 2008). On the other hands, the eutectic temperatures for most metal catalyst were higher than those of the Au-Si or Au-Ge eutectics. This has led to investigation of vapor-solid-solid (VSS) growth of nanowires at sub-eutectic temperatures, where catalyst nanoparticles should remain solid throughout the growth process (Lensch-Falk et al., 2009).

For Si nanowires, the VSS growth was first reported in 2000 when Kamins and his co-workers deposited Ti as the metal catalyst with either SiH_4 or $SiCl_2H_2$ as the silicon precursors using CVD methods. The nanoparticles found at the tip of each nanowire were identified as $TiSi_2$ (Kamins et al., 2000). Eight years later, Hofmann et al. (2008) utilized in-situ transmission electron microscopy (TEM), to observed VSS growth of Si nanowires by using Pd as the catalyst and Si_2H_6 as the Si precursor. The catalyst nanoparticle was found to be Pd_xSi. Growth was observed to occur by ledge propagation where the nucleation of each new ledge was the rate limiting step. This first in-situ observation of VSS growth provided new insights into the mechanism of the incorporation of atoms into the Si nanowire.

Lensch-Falk et al. (2009) reported that the metal-catalyzed anistropic growth can be broken into four steps as shown in Figure 2.4: i) delivery of precursor species to the substrate, ii) precursor decomposition, iii) diffusion in or on the catalyst particle, and iv) incorporation of adatoms into the growing nanowire. Each of these steps introduces specific requirements for appreciable VSS growth to be realized. First, sufficient source material must be delivered to the substrate for growth to occur. For CVD growth with

University of Malaya

molecular precursors, precursor species must decompose at certain temperatures in order to provide a sufficient flux of adatoms to the catalyst and nanowires surfaces (Figure 2.4(a)). Next, Ge or Si adatoms (precursor species) must be delivered to the growth interface by bulk or surface diffusion.

While the Si or Ge atoms moving to the growth interface, diffusion of metal catalyst away from semiconductor growth interface occurs. Thus elongation of the Si nanowire at the catalyst/Si interface to be occurs (Figure 2.4(b)). Finally, anisotropic growth requires the preferential incorporation of adatoms at one interface (Figure 2.4(c)). It appears that metal seed particles in general, whether solid or liquid, locally reduce kinetic barriers to growth of the semiconductor phase. If there was a kinetic barrier to nucleation of new planes at the metal semiconductor interface, this process can be rate limiting for VSS nanowire growth.

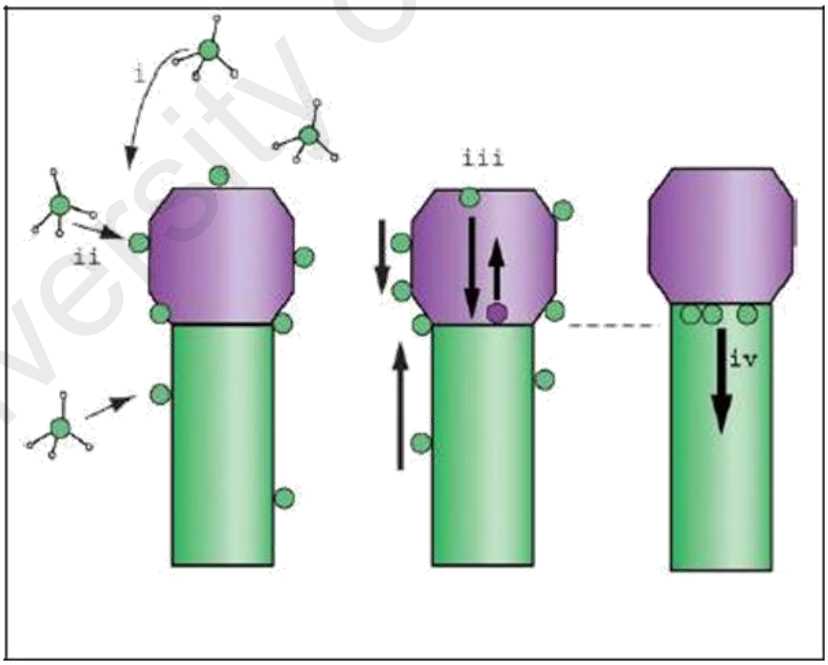

Figure 2.4: Schematic of VSS nanowire growth. (a) Delivery of the precursor to the nanowire surface (i) and decomposition of this precursor. (ii) (b) Atoms are delivered to the metal catalyst/nanowire interface by surface or bulk diffusion processes. (iii) (c) Si or Ge atoms are incorporated at the growth interface (metal catalyst/nanowire interface) leading to anisotropic growth (iv). (Lensch-Falk et al., 2009)

University of Malaya

2.2.3 Solid-Phase Diffusion

Based on phase diagram, temperature measurements and temperature-size effects, the growth of nanowires usually be concluded occurs via VSS mechanism. However, there were some reports shows that metal-catalyzed growth of nanowires in which metal nanoparticle remained in the solid phase during the nanowires growth (Campos et al., 2008; Persson et al., 2004). Many of metals nanoparticles such as Ti, Co, and Ni, form silicides with the potential for solid-phase seeding of nanowires (Tuan et al., 2005b). This growth mechanism was proposed to be solid-phase diffusion mechanism. A few researches had demonstrated the solid-phase diffusion mechanism on Si, Ge and ZnO nanowires (Campos et al., 2008; Tuan et al., 2005a, 2005b). Molnár et al. (2009) clearly summarized the main differences between VLS and solid- phase diffusion mechanism, which includes the main physical principles, the field of validity and typical material systems as shown in Table 2.1.

Table 2.1: Summarized the main differences between VLS and solid-phase diffusion mechanism. (Molnár et al., 2009)

Model	Main physical principles	Grown from	Controlled by	Character of the main process	Time dependence
VLS	Surface tension solubility	Liquid	Material flow in liquid	Non-equilibrium	Yes
Solid-phase diffusion	Diffusion	Solid	Diffusion	Near equilibrium	No

Tuan et al. (2005a) reported that Ni nanocrystals promoted Si nanowires synthesis in supercritical toluene at temperatures as low as 450°C, which was more than 350°C below the lowest temperature Ni-Si eutectic, and concluded that Ni nanocrystal-seeded Si nanowires growth can occur by a solid-phase diffusion mechanism from the metal particle. They demonstrated the formation of Si nanowires from silane precursors in

University of Malaya

organic solvents at ~460°C and ~20 MPa. The Ni nanocrystals have induced crystallization and catalyze the precursor (i.e., arylsilanes, alkylsilanes, trisilane) decomposition.

Figure 2.5 shows SEM images of Si nanowires. The reaction temperature had a significant influenced on the quality of the nanowires. The best growth temperature at this pressure was 460°C, producing straight crystalline nanowires longer than 10 μm with Si diamond cubic crystal structure and few dislocation defects (Figure 2.5(c)). The inset in Figure 2.5(c) shows an example of a Ni nanoparticle at the tip of a nanowire. Ni nanocrystals with 5~6 nm diameter produced nanowires with slightly larger diameter, between 7 and 25 nm. It can be seen that the Ni nanocrystals promoted Si nanowire growth by a solid-phase diffusion mechanism. At 580°C (Figure 2.5(e)) and above, nanowires do not form. At the higher reaction temperatures, homogeneous Si particulated formation competes with heterogeneous nanowire growth.

Based on SEM images, they provided an overview of formation of Si nanowires using solid-phase diffusion mechanism. Figure 2.6(a) shows homogeneous MPS decomposition occurring by disproportionation versus heterogeneous MPS, octylsilane, and trisilane decomposition catalyzed by the Ni surface. Octylsilane and trisilane required heterogeneous catalytic decomposition on the Ni surface to form nanowires, whereas MPS can undergo homogeneous disproportionation to silane, which can then give rise to nanowire growth. Figure 2.6(b) shows the Si atoms diffused into the Ni nanocrystal until reaching saturation. Then silicon nanowire nucleates and crystallizes from the Ni/Si alloy interface (Figure 2.6(c)), growing to produce the high aspect ratio nanowire illustrated in Figure 2.6(d).

University of Malaya

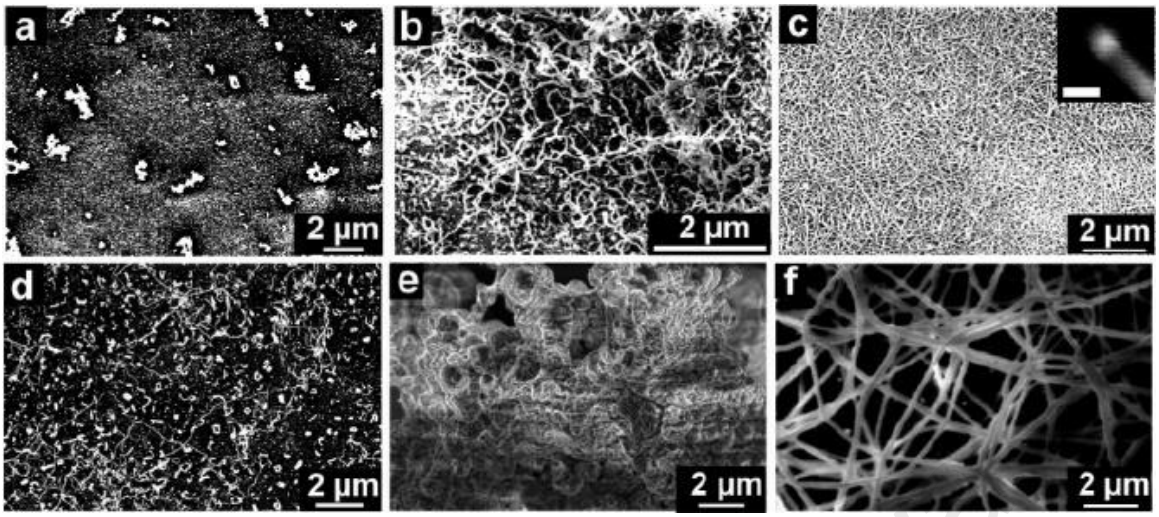

Figure 2.5: SEM images of Si nanowires synthesized from MPS in toluene at 23.4 MPa (10 min, 27.4 mM MPS [Si]/[Ni]) 100) at (a) 340°C (b) 400°C (c) 460°C (d) 520°C (e) 580°C (f) 460°C. (Tuan et al., 2005a)

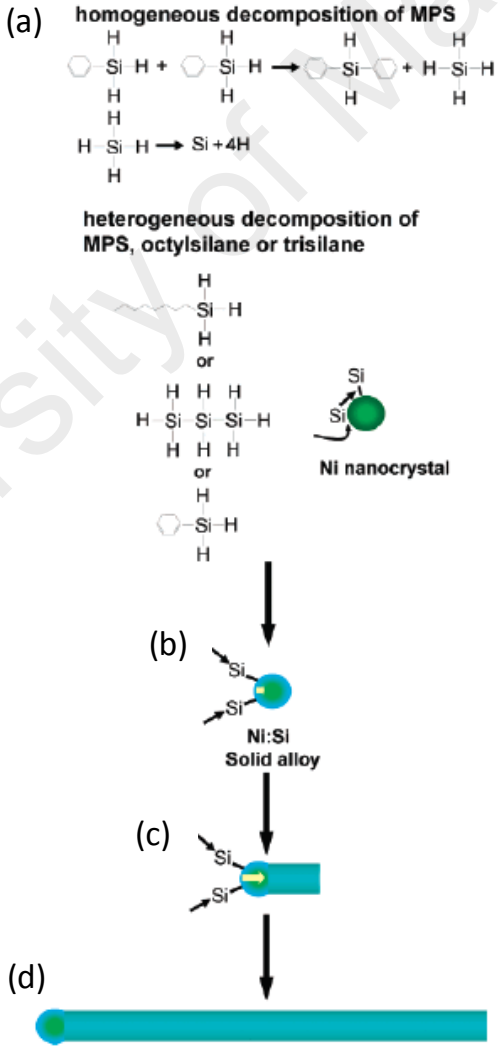

Figure 2.6: (a-d) Si nanowire growth via solid-phase diffusion mechanism.(Tuan et al., 2005a)

University of Malaya

2.3 Growth Techniques

2.3.1 Introduction

CVD is defined as the deposition of a solid on a heated surface from a chemical reaction in the vapor phase (Kodas, 1994). Chemical vapor deposition has a number of key advantages in depositing metal films if compared to other thin film deposition techniques such as physical vapor deposition. These advantages include conformal coverage (the ability to coat a surface with complex topography with a layer of uniform thickness), selective deposition (the ability to deposit a coating on one surface, often referred to as the growth surface and not on another. the non-growth surface), and low deposition temperatures (which can be a primary concern for thermally sensitive substrates) (Park & Sudarshan, 2001).

2.3.2 Low-Pressure Chemical Vapor Deposition (LPCVD)

Low-pressure chemical vapor deposition (LPCVD) technique is one of the most common CVD techniques that have been used widely to grow nanowires for supercapacitors application (Alper et al., 2013; Gu et al., 2015; Vincent et al., 2012). However, this technique suffers several disadvantages that limit their supercapacitor performance and its commercial values as such as high cost production, low deposition rates, poor flexibility and high temperature usually above 600°C for the process flexibility (Morosanu, 2013; Stoffel et al., 1996). Figure 2.7 shows a schematic diagram of typical a hot-wall LPCVD reactor used in poly-SiC growth. The LPCVD process has a quartz tube that being placed in a spiral heater that starts with pressure very low pressure around 0.1 Pa. The tube is then heated to the desired temperature that is in between 300 to 400°C and the gaseous species that consists of dilution gas and the reactive gas is inserted into the tube at the pressure predetermined between 10-1000 Pa. This working gas will react with the substrate and create a solid phase material on the substrate. After the working gas enters the tube it spreads out around the hot substrates

University of Malaya

that are already in the tube at the same temperature. The substrate temperature is extremely important and influences what reactions take place (Grob, 2013).

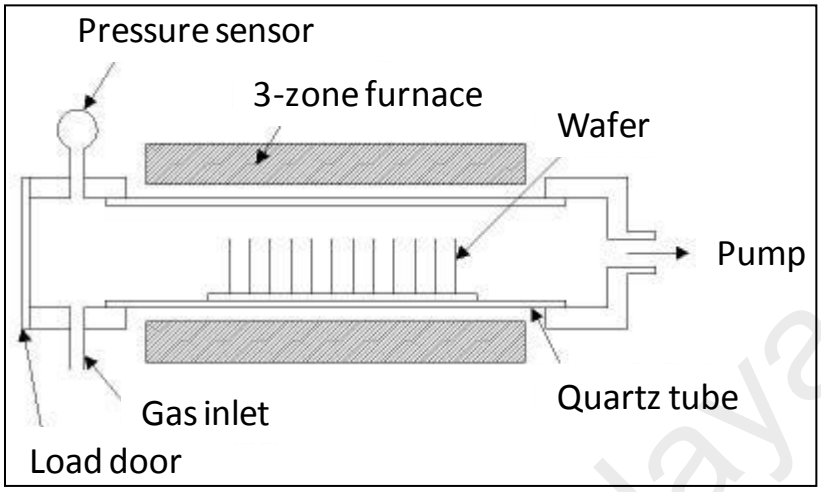

Figure 2.7: A schematic diagram of a LPCVD reactor used in poly-SiC growth. (Grob, 2013)

2.3.3 Hot-Wire Chemical Vapor Deposition (HWCVD)

Hot-wire CVD was first introduced and patented as 'thermal CVD' by Wiesman and his colleagues in 1979. They reported that a –Si: H thin films could be formed by cracking molecules of SiH_4 has with carbon or tungsten foil heated to 1400-1600°C (Wiesmann et al., 1979). Unfortunately, this work did not attract much attention because the quality of their films was much worse than the obtained by PECVD at that time. Approximately 6 years later, thermal CVD was used by Matsumura and Tachibana from Japan Advance Institute of Science at Technology (JAIST) for the preparation of fluorinated amorphous silicon. They succeeded in obtaining high quality a-Si: H by decomposing a silane-hydrogen gas mixture with a tungsten wire (Matsumura, 1998). He called the method as Catalytic CVD (Cat-CVD) technique. The preparation of hydrogenated amorphous silicon (a-Si:H) was further investigated by Doyle from University of Colorado in the late 1980's showing a high deposition rate as the prominent feature. He called the method as Evaporative Surface Decomposition (ESD) (Doyle et al., 1988). Mahan and co-workers at the National Renewable Energy

University of Malaya

Laboratory (NREL) extensively studied the properties of a-Si:H obtained by this technique and contributed to increase the research in this field. They first called the method as Hot-wire Chemical Vapor Deposition (HWCVD) (Mahan et al., 1991) which seems commonly found in the literature.

The principle of the success of HWCVD in obtaining these high quality films is that the feedstock gases are very efficiently cracked into atomic radicals at the surface of the hot filament (usually tungsten or tantalum), if this is held at a temperature higher than 1500°C. The reactive species are subsequently transported to the substrates in a low pressure ambient, which enables a high deposition rate without gas phase particle formation (Ruud, 2002). Matsumura, who had continued developing this technique in parallel, demonstrated in 1991 the possibility of obtaining nc-Si:H films by this method at substrate temperatures only around 300°C (Matsumura, 1991).

HWCVD has been extensively studied mainly for silicon thin films with amorphous, microcrystalline, and polycrystalline properties (Ruud, 2002). Recent studies showed this technique has become one of the most promising techniques for low temperature, high deposition rate and large-area deposition for SiC based thin films materials (Jha & Agarwal, 2015; Pawbake et al., 2016). The filament temperature (T_f) is considered an important since it directly affects decomposition of SiH_4 gas, which produces the different radicals species for the deposition (Chong et al., 2011a).

In HWCVD process, at T_f>1500°C, SiH_4 molecules are dissociatively absorbed on the surface of tungsten filament in a form of Si and H. The Si- and H-bonded to tungsten are then catalytically cracked and desorbed into Si and H radicals following the process as reported by Tonokura et al. (2002):

$$SiH_4(g) \rightarrow Si(g) + 4H(g) \qquad 2.1$$

The presence of H radicals can result in the interactions with SiH_4 molecules as (Nozaki et al., 2001):

University of Malaya

$$H(g) + SiH_4(g) \rightarrow SiH_3(g) + H_2(g) \quad 2.2$$

The SiH_3 radical does not react with SiH_4 molecules due to its higher stability. Hence, the SiH_3 and Si_2H_4 radicals are generally two candidates corresponding to the growth.

Filament temperature also has significantly affect decomposition efficiency of CH_4. According to Komura et al. (2007), decomposition of CH_4 takes place mainly through gas-phase reaction:

$$CH_4(g) + H(g) \rightarrow CH_3(g) + H_2(g) \quad 2.3$$

For filament temperature, $T_f > 1800^oC$, any increase in H_2 dilution directly increase the decomposition of SiH_4 and H_2 thus generating high densities of SiH_3 radicals and atomic H. The formation of reactive atomic H thus enhanced the decomposition of CH_4 through gas phase reaction.

XRD spectra of the samples deposited at different T_s are shown in Figure 2.8. The spectrum for the c-Si substrate as a background was also inserted in the figure as a reference. Appearance of sharp diffraction peaks at $2\theta = 28.4^o$, 47.3^o, 56.4^o, 69.6^o and 76.8^o which correspond to the crystalline silicon orientation planes of (111), (220), (311), (400) and (331), respectively, indicating that the films are highly crystalline in structure. Furthermore, appearance of the diffraction broadening at 38.2^o corresponds to Au orientation plane of (111) confirms the presence of Au nanocrystallites in the films (Chong et al., 2011b).

Figure 2.9 shows the deposition rate of the film vs. the filament temperature for films that deposited at 10 Pa, with a SiH_4 flow of 20 sccm and a hydrogen flow of 300 sccm (Van der Werf et al., 2003). From this figure, it clearly shows that deposition rate increased linearly as filament temperature increased due to high dissociation rate of SiH_4 on the filament surface.

University of Malaya

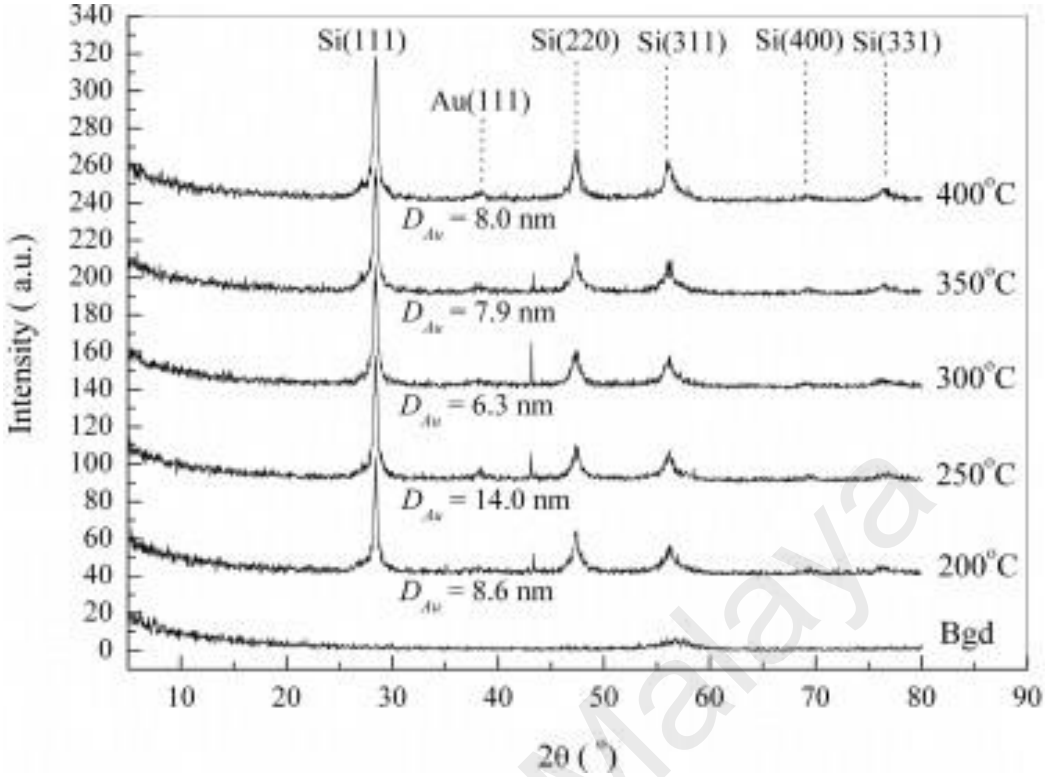

Figure 2.8: XRD spectra of gold- catalyzed silicon nanostructures synthesized at different T_s. (Chong et al., 2011b)

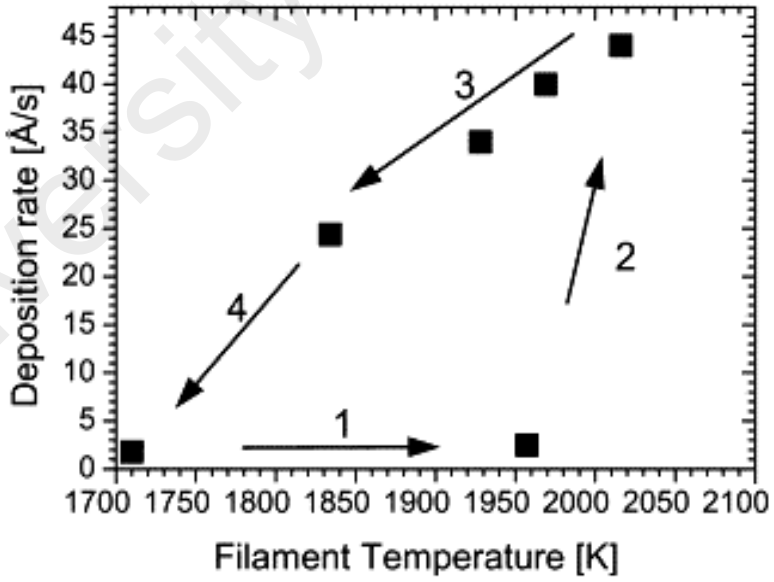

Figure 2.9: The deposition rate (top) and power dissipation due to exposure to gas (bottom) vs. the filament temperature for films deposited at 10 Pa, with a silane flow of 20 sccm and a hydrogen flow of 300 sccm. The arrows show the direction of the temperature change. (Van der Werf et al., 2003)

University of Malaya

2.4 NiSi Nanowires

2.4.1 Introduction

Metal silicides are intermetallic compounds between metals and silicon. The silicon atoms dissolve into the metal lattices, which results in withdrawal of electron density from the metals by the electronegative Si element. Such materials have diverse physical and chemical properties that are both useful and fundamentally significant (Chen et al., 2014). Among various silicides, Nickel silicides consisting of Si and Ni have low contact resistance, and excellent field emission properties are considered as a promising material in Si-based microelectronics and optoelectronics (Lin et al., 2015). Ni-rich silicides, such as Ni_2Si nanowires, are attractive nanoscale building blocks for interconnects and fully silicided gate applications in nanoelectronics due to its low electrical properties and their high work functions (~4.8 eV). Besides, nickel silicides also have a very high melting point and excellent electrochemical properties, that can been use in low-power memory devices, and for energy storage devices mainly of lithium-ion batteries and supercapacitors (Jiang et al., 2016).

2.4.2 Formation of NiSi

The Ni-Si system is one of the binary alloys that form the multi-component Ni-based metal systems. The phase diagram of the Ni-Si system has been studied many times, and it has been evaluated by Nash and Nash (1987). The evaluated phase diagram compiled by Massalski et al. (1990) as shown in Figure 2.10. The phase diagram was composed of 14 phases. These include the two terminal solid solutions of Si in Ni, and of Ni in Si along with the liquid phase, and 11 intermediate phases. These 11 intermediate phases are: $Ni_3Si(\beta_1)$, $Ni_3Si(\beta_2)$, $Ni_3Si(\beta_3)$, $Ni_2Si(\theta)$, $Ni_3Si_2(\varepsilon L)$, $Ni_3Si_2(\varepsilon H)$, $Ni_5Si_2(\gamma)$ $Ni_2Si(\delta)$, NiSi, $NiSi_2(\alpha)$ and $NiSi_2(\beta)$.

University of Malaya

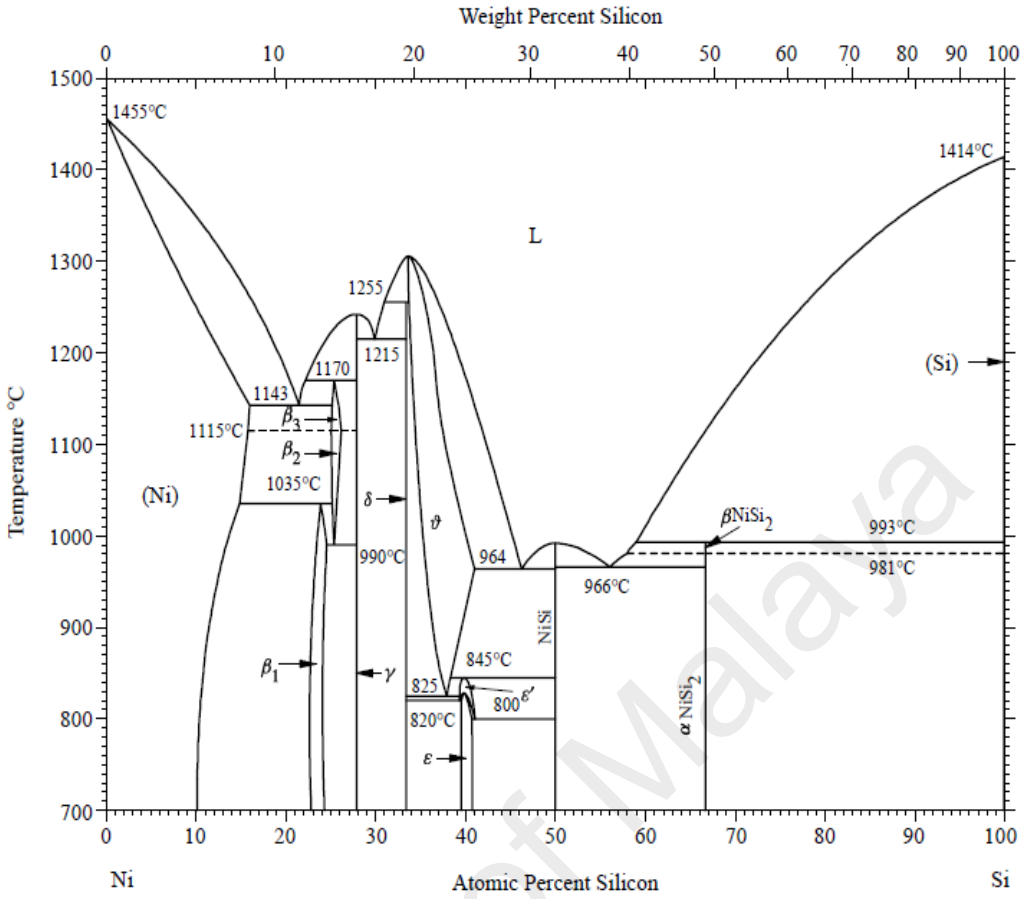

Figure 2.10: The Ni–Si phase diagram compiled. (Massalski et al., 1990)

2.4.3 Physical properties

The reduction of material's size to nanoscale dimensions has often resulted in new physical phenomena and interesting applications such as optoelectronic and energy storage devices. Table 2.2 shows some physical properties of the six Ni silicide phases stable at room temperature. They are crystal structure, lattice constants, resistivity and melting points. The melting point of the silicides provides an indication of the morphological stability of thin films. A low melting point most likely leads to substantial atomic diffusion of the constituents already at a low temperature. As a result, degradation of the silicide film occurs at low temperatures (Lavoie et al., 2004).

University of Malaya

Table 2.2: Properties of Ni_xSi_y phases. (Lavoie et al., 2004)

Phases	Crystal structure	Lattice constants (Å)	Resistivity (μΩ cm)	Melting points (°C)
Ni_3Si	Cubic	a=3.505	80-90	1170
$Ni_{31}Si_{12}$	Cubic	a=6.671; c =12.288	90-150	1242
Ni_2Si	Hexagonal	a =7.39, b =9.90; c =7.03	24-30	1306
Ni_3Si_2	Orthorhombic	a=12.22;b= 10.80; c=5.659	60-70	845
NiSi	Orthorhombic	a=5.233; b=3.258; c=5.659	10.5-18	992
$NiSi_2$	Cubic	a= 5.416	34-50	993

Many research has been done in order to studies their structure, diameter, length and chemical compositions of single crystalline NiSi nanowires at different parameters (Lin et al., 2015; Tu, 2013). For instance, Lin et al. (2015) studies the morphological changes with various substrate temperatures by using horizontal hot-wall furnace for the chemical vapor deposition (CVD) process. Figure 2.11 shows SEM images and XRD spectrum of NiSi nanowires grown at 750°C, 850°C and 950°C, respectively. As shown in Figure 2.11(a&b), high density nanowires arrays with lengths of over 60 μm were observed at 750°C and 850°C grown vertically with respect to the silicon substrates. When substrate temperatures increased up to 950°C (Figure 2.11(c)), nanowires tended to grow horizontally with lower densities and lengths of over 100 μm. This may be attributed to the fact that the increasing weight with the increasing length of single nanowires can no longer be supported by the root, leading to the horizontal growth of the nanowires. Figure 2.11(d) shows the nanowires grown at 400°C where only Ni peaks were detected based on the XRD analysis. The XRD analyses of the samples at growth temperatures of 750–950°C were shown in Figure 2.11(e). The diffraction peaks of the 750°C sample were for the $Ni_{31}Si_{12}$ phase. When substrate temperature increased

University of Malaya

up to 850°C, the peaks mainly corresponded to the Ni_2Si phase. At substrate temperature of 950°C, the $NiSi_2$ peaks were dominating.

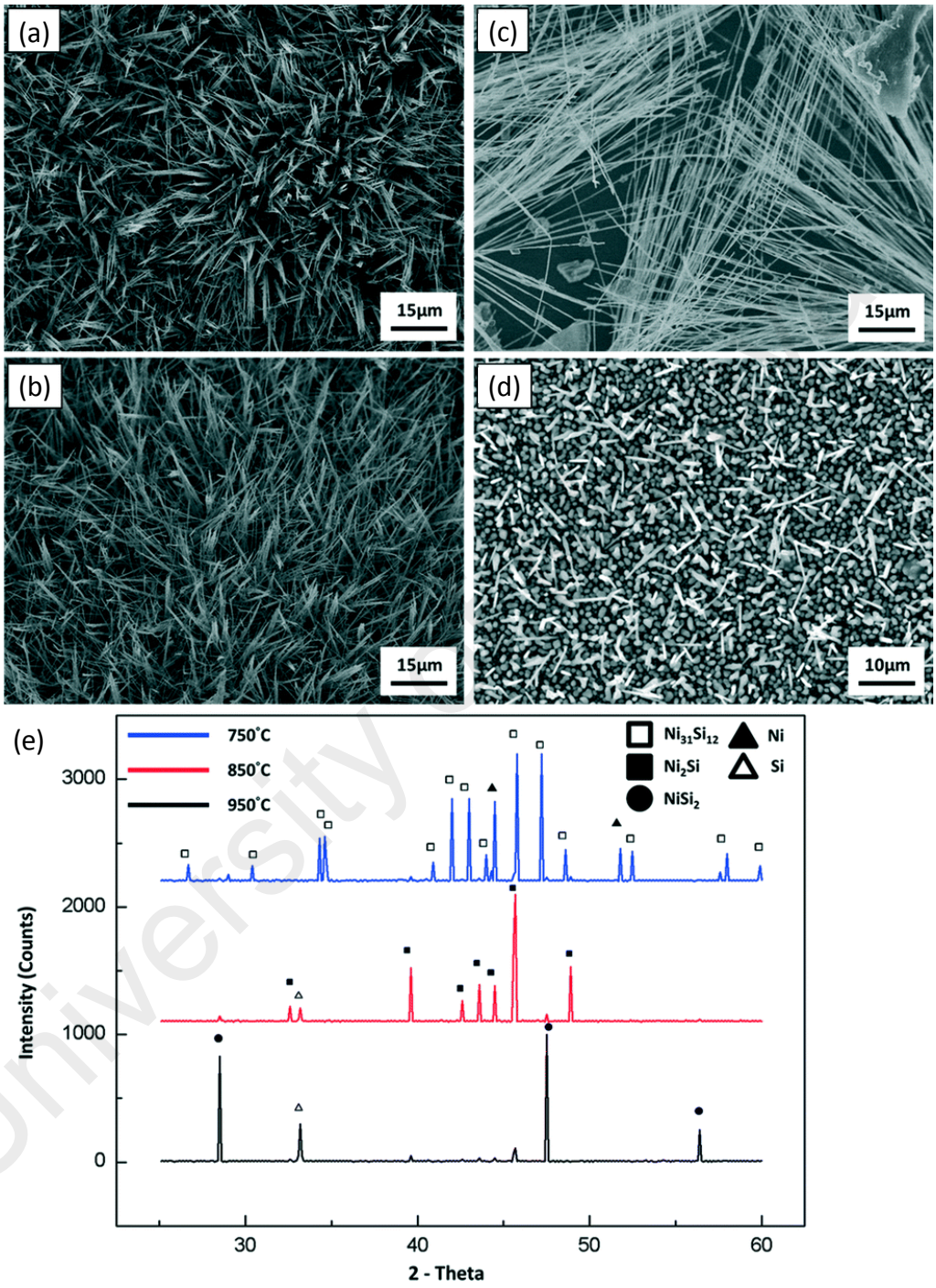

Figure 2.11: SEM images of NiSi nanowires grown on (100) Si substrates at (a) 750°C (b) 850°C and (c) 950°C (d) Ni nanowires grown on a (100) Si substrate at 400°C and 70 torr (e) XRD analyses of the nickel silicide nanowires grown on (100) Si substrates at 750°C, 850°C and 950°C. (Lin et al., 2015)

University

Chiu et al. (2013) studies physical properties of single crystalline and Ni_2Si nanowires at different pressure (6 to 15 Torr). This experiment was carried out in the three-zone furnace via a chemical vapor deposition process. Figure 2.12(a-d) shows the SEM images of NiSi nanowires grown at different pressures, indicating that the geometry on the surface of substrates varied with the ambient condition. With lower partial pressure of the precursor, as shown in Figure 2.12(a), Ni silicide nanowires were not formed due to insufficient supply of the Ni source and small nanowhiskers can be observed on the surface. As ambient pressure was raised to range of 9 to 12 Torr (Figure 2.12(b&c)), high aspect ratios were obtained with slightly increased in diameter of the nanowires from 30 to 50 nm to 40 to 70 nm. Furthermore, when the pressure was higher than 15 Torr, the concentration of the Ni source was oversaturated and the morphology of the product turned into islands instead of nanowires. Those islands may result from the condition change to decrease the surface energy of the system by transforming into bulk-like structures, as shown in Figure 2.12(d). As a conclusion, the diameter of the nanowires can be controlled under specific pressure range and the ambient pressure plays an important role in maintaining the morphology of the nanowires.

University of Malaya

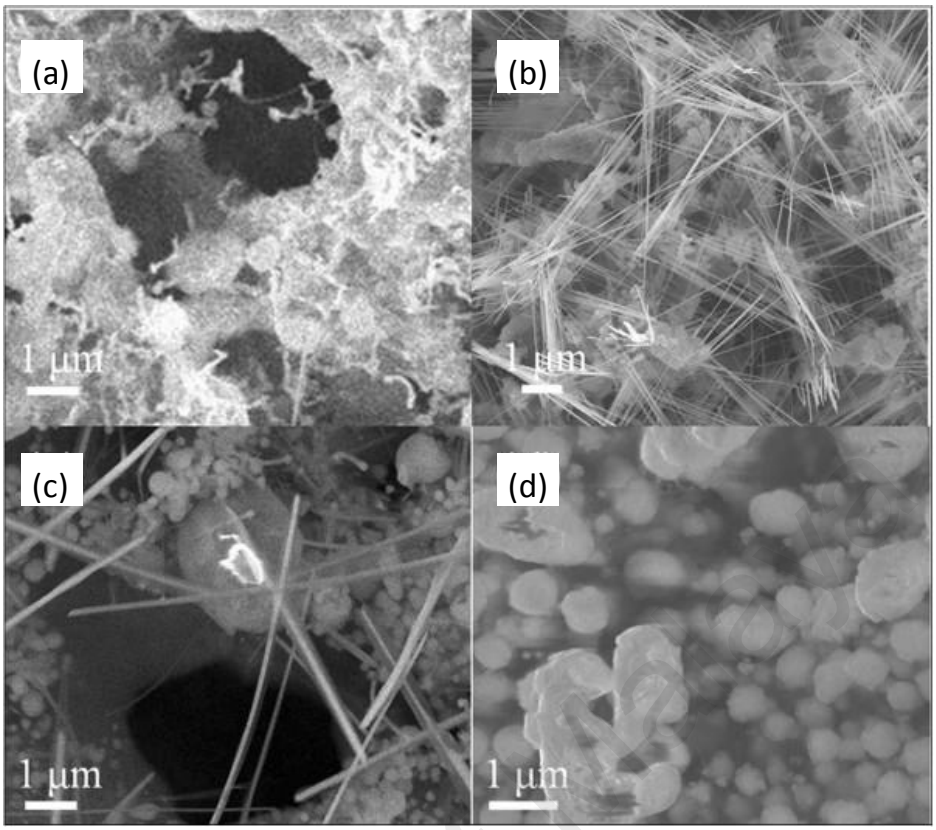

Figure 2.12: SEM images of Ni_2Si nanowires at vacuum pressures of (a) 6 (b) 9 (c) 12 and (d) 15 Torr. The temperature was fixed at 400°C reaction time was 30 min and carrier gas flow rate was held at 30 sccm. (Chiu et al., 2013)

2.5 SiC Nanowires

2.5.1 Introduction

Among of the 1D semiconductor nanostructures, SiC is widely investigated due to its unique properties such asis a wide-band-gap, excellent thermal conductivity, high breakdown electric field, high electron mobility, good thermal shock resistance and excellent chemical physical stability, which promise well for applications in microelectronics, optoelectronics, and supercapacitors (Gu et al., 2015; Hu et al., 2016; Ruff et al., 1994; Zhuang et al., 2015). Furthermore, SiC nanowires is a suitable material for the fabrication of high performance nanodevices in harsh environment applications which require high temperature resistance, high power, and high frequency (Maboudian et al., 2013; Senesky et al., 2009). Historically, the scientist Dr. Edward Goodrisch Acheson, the first man who had invented SiC in 1893. Acheson's discovery

University of Malaya

became Carborundum, the trademark for silicon carbide (Djokoto & Karimi, 2011). SiC nanowires with high aspect ratio could also become an effective reinforcement phase for ceramic-, metal-, and polymer-matrix, composites (Zhou et al., 2006). Therefore, SiC nanowires have attracted considerable interest from material science and electronic device applications, which highly focused on fundamental research and potential applications in micro and nano-devices (Duan et al., 2003).

2.5.2 Physical properties

Morphology of nanomaterials is known to have influence of their properties (Khongwong et al., 2010). A few research proved the effects of SiC nanowires morphology on their properties. For example, (Huang et al., 2014) fabricated twinned SiC nanowires by using catalyst-free thermal CVD method. The morphological of the SiC nanowires were shown in Figure 2.13. Figure 2.13(a&b) shows FESEM images of SiC nanowires at low magnification and high magnification. Figures revealed that both straight and curved nanowires grow randomly on the Si substrate. Nanowires were grown with lengths of up to several hundred microns and relatively homogeneous diameters in the range 20 nm to 100 nm. Figure 2.13(b) shows that the surface of these nanowires was rough and randomly oriented. EDS image as shown in Figure 2.13(c) shows that the nanowires mainly contained Si and C, indicating that the products were SiC nanowires. Figure 2.13(d) shows the X-ray diffraction (XRD) pattern of the products. The strong intensities and narrow widths of the peaks indicated that the nanowires were crystalline. As Figure 2.13(d) indicated, all the strong peaks could be indexed to β-SiC. A small peak, signed SF ahead of the highest intensity peak (111), was assumed to have been due to stacking faults (twins).

University of Malaya

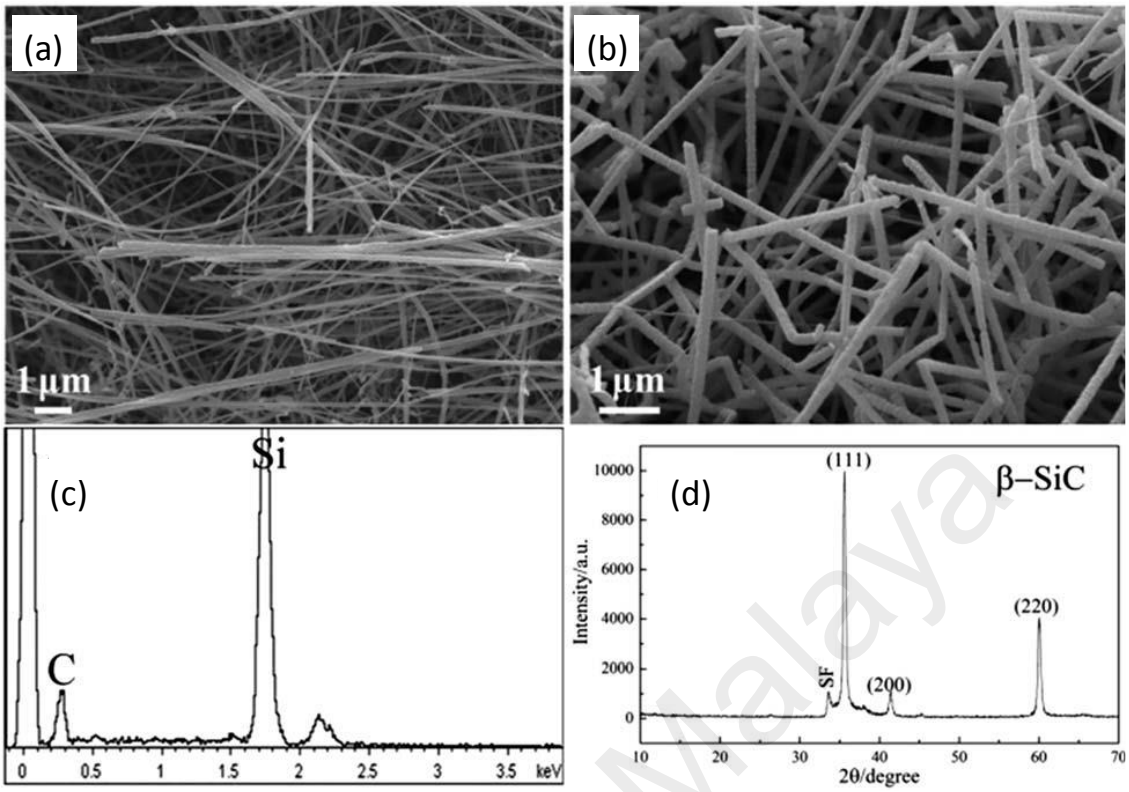

Figure 2.13: (a) Low magnification and (b) high magnification FESEM images of SiC nanowires. (c) EDS pattern of SiC nanowires. (d) X-ray diffraction pattern of SiC nanowires. (Huang Z. et al., 2014)

2.6 Heterostructure Nanowires

The single-phased intrinsic nanowires generally facing limitation such as low conductivity, weak mechanical stability and associated side reactions due to its unprotected surface. Therefore, heterostructure nanowires or core-shell nanowires have significantly demonstrated to overcome the limitation of the intrinsic nanowires in various applications such as optoelectronics and energy conversion devices due to their enhanced properties compared to both the single-phased materials alone (Liu et al., 2010; Taberna et al., 2006; Xia, 2012). The core–shell nanowire structure has an ability to can increase charge collection, suppress recombination, and show higher emission intensity and low thermal conductivity which help improve the efficiency of devices with respect to intrinsic single nanowires (Chen et al., 2007).

University of Malaya

Core-shell nanowires have been widely used in supercapacitor and optoelectronic applications due to their extremely large surface area of 1D structures Cui and co-workers, for instance, reported that crystalline core-amorphous shell Si nanowire designs show significant enhancement in their capacity/power rates and efficiency in lithium-ion batteries and solar cells, respectively (Cui et al., 2008). Lauhon et al. demonstrated an enhancement of carrier mobility in a coaxial field effect transistor that was fabricated by modulation-doped core-shell structures (Lauhon et al., 2002).

2.7 Supercapacitors

As important electrochemical energy storage devices, supercapacitors also called electrochemical capacitors (ECs) are one of the most promising energy storage devices owing to their intrinsic performances advantages (Simon & Gogotsi, 2008). They store energy in terms of charges by either ion adsorption (electrochemical double layer capacitors (EDLCs)) or surface faradic reactions (pseudocapacitors) on electrodes (Yu et al., 2015). Moreover, they also showed an excellent performance such as high power densities, long cycle's lives and a wide range of working temperatures (Korenblit et al., 2012; Lin et al., 2011). Nanowires have been reported as promising candidates for supercapacitor electrodes because of their network capabilities, resulting in the formation of electrodes with high conductivities for electron transport and open porous structure for easy electrolyte diffusion, which lead to high charge/discharge rates (Jiang et al., 2012).

According to previous reports there are two main factors that can determine the performance of supercapacitors. (1) Surface area: Since charges are stored on the surface of the supercapacitor electrodes, an electrode with a higher surface area leads to an improved specific capacitance. Enlarging the surface area of electrodes will lead to improved specific capacitance owing to the increased amount of charges stored on their surfaces. (2) The intrinsic properties of electrode materials. Materials that are

University of Malaya

electrically conductive have a capability to reduce capacitance losses, particularly at high scan rates or at high current densities. Besides that, materials that have high mechanical and chemical stability properties also have greatly influenced the cycle stability of the electrodes (Choudhary et al., 2016; Yu et al., 2015).

Unlike 1D nanomaterials such as nanowires and nanorods, core–shell structures have received considerable as one of the potential candidates for the next generation electrode designs. This is because one major advantage of using core-shell structures electrode design is the synergic improvement of intrinsic properties of each component for better electrical conductivity, faster ionic transport, greater electrochemical reversibility and cycle stability, and improved mechanical stability (Huang et al., 2013; Yu et al., 2015). Figure 2.14 shows CV curves of pure SiC nanowires and SiC nanowires/$Ni(OH)_2$. The CV curve of SiC nanowires/$Ni(OH)_2$ shows a pair of redo peaks, resulting from the faradaic oxidation and reduction reaction of $Ni(OH)_2$. Without the shell of nanowires ($Ni(OH)_2$), the current signals of the SiC nanowires was small. This result proved that the core-shell structured enhanced the supercapacitor performances of the nanowires. However, in the core-shell structure, proper control of the microstructure and the thickness of the shell are absolutely required to extract superior performance from the capacitor.

University of Malaya

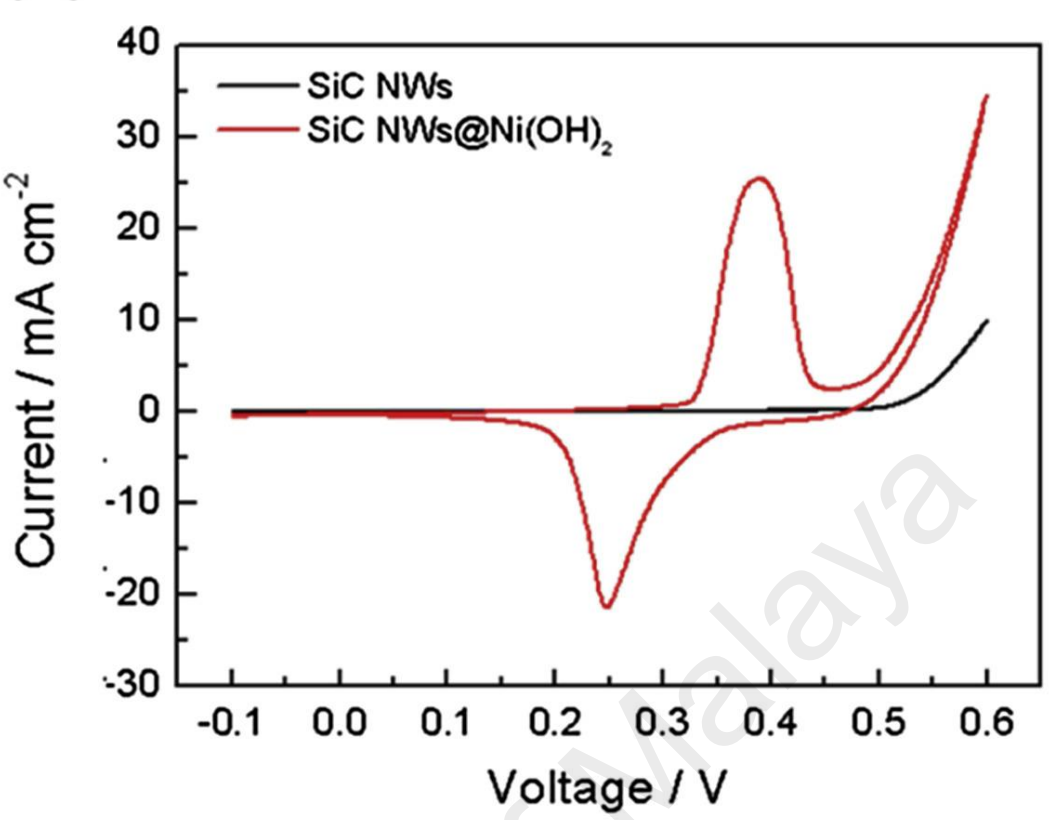

Figure 2.14: (a) CV curves of the pure SiC NWs on carbon fabric and SiC nanowires/$Ni(OH)_2$ on carbon fabric with the same scan rate of 5 mV s^{-1}. (Gu et al., 2015)

Gu et al. (2015) studies the morphological effects of SiC core and $Ni(OH)_2$ shell at different deposition times on their supercapacitor performances. Figure 2.15(a-d) show SEM images of SiC/$Ni(OH)_2$ at different deposition time of $Ni(OH)_2$ at 1, 2, 3 and 4 minutes. With the increasing of the deposition time of $Ni(OH)_2$, the $Ni(OH)_2$ nanoflakes become thicker. The diameter of $Ni(OH)_2$ flakes effect the specific capacitances of the nanowires. The specific capacitances decreased at the same charge/discharge as deposition time of $Ni(OH)_2$ increasing from 1 min to 4 min (Figure 2.15(e)).

In addition, the effect of SiC core nanowires also studies in this research. Figure 2.16(a-c) shows the morphologies of SiC nanowires on carbon fabric with the growth time of 15, 30 and 60 min. The length of SiC nanowires clearly increased with the growth time. The increased lengths of the nanowires affect the specific capacitance of the nanowires. When the growth time is 15 min, SiC nanowires were too short for

University of Malaya

deposition of enough $Ni(OH)_2$. It makes the deposited $Ni(OH)_2$ dense and thick, leading to large internal resistance and poor electrochemical property. However, when the growth time increased to 60 min, SiC nanowires were very long. Although the surface area increased, the length of transport channel for electrons increases significantly (the distance for electrons to transport from the top of the nanowire to the bottom/carbon fabric increased), resulting in large equivalent series resistance and poor electrochemical property. Figure 2.16(d) shows the specific capacitances of SiC nanowires/$Ni(OH)_2$ at the current density of 2 A g^{-1} as a function of SiC nanowires growth time (15-60 min). With the same deposition time of $Ni(OH)_2$, SiC nanowires/$Ni(OH)_2$ with the SiC nanowires growing time of 30 min has the largest specific capacitance.

University of Malaya

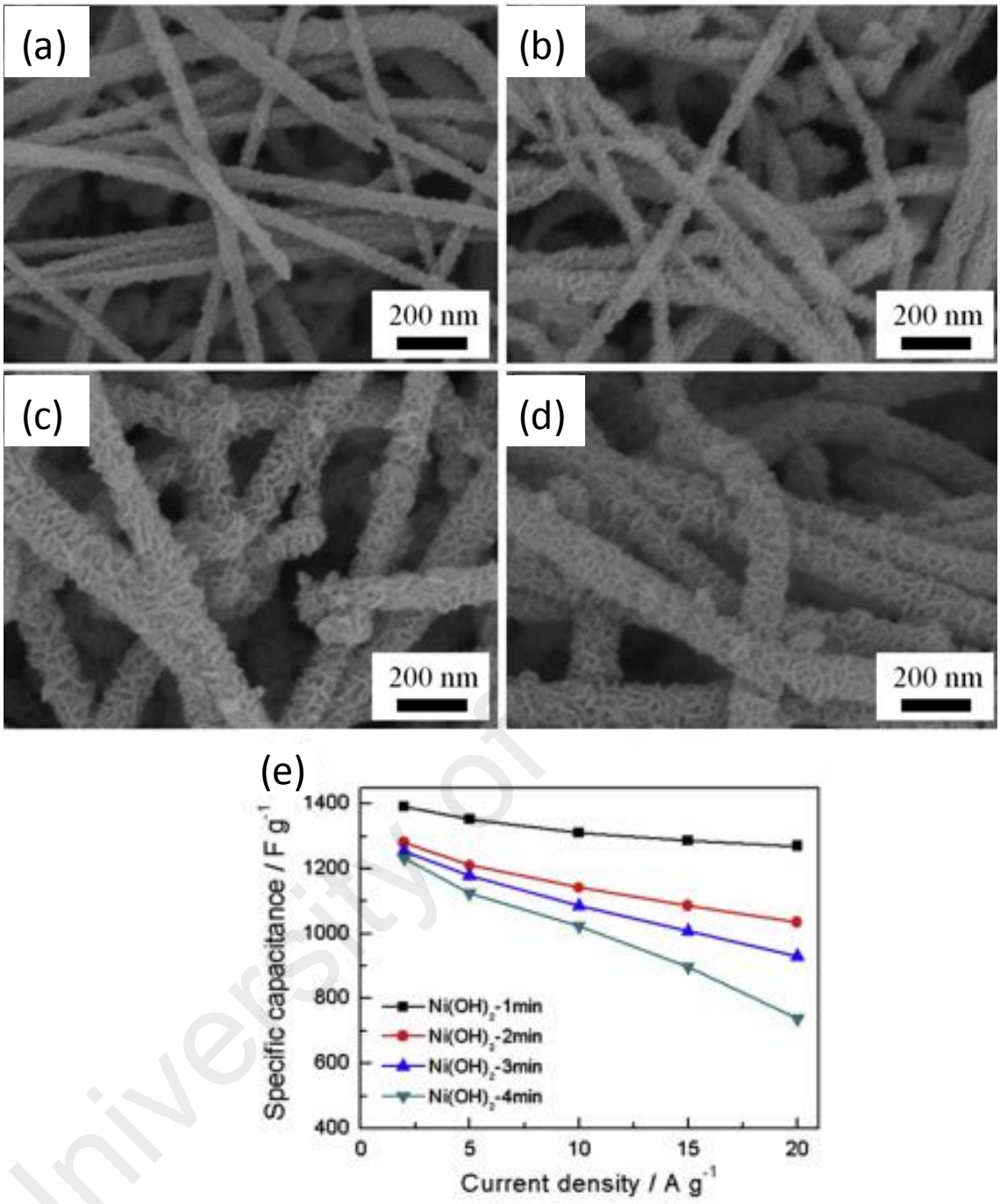

Figure 2.15: (a-d) Morphology of $Ni(OH)_2$ on SiC nanowires with different deposition time. (e) Specific capacitances of $Ni(OH)_2$ on SiC nanowires with the growth time of 15 min as a function of charge-discharge current density. (Gu et al., 2015)

University of

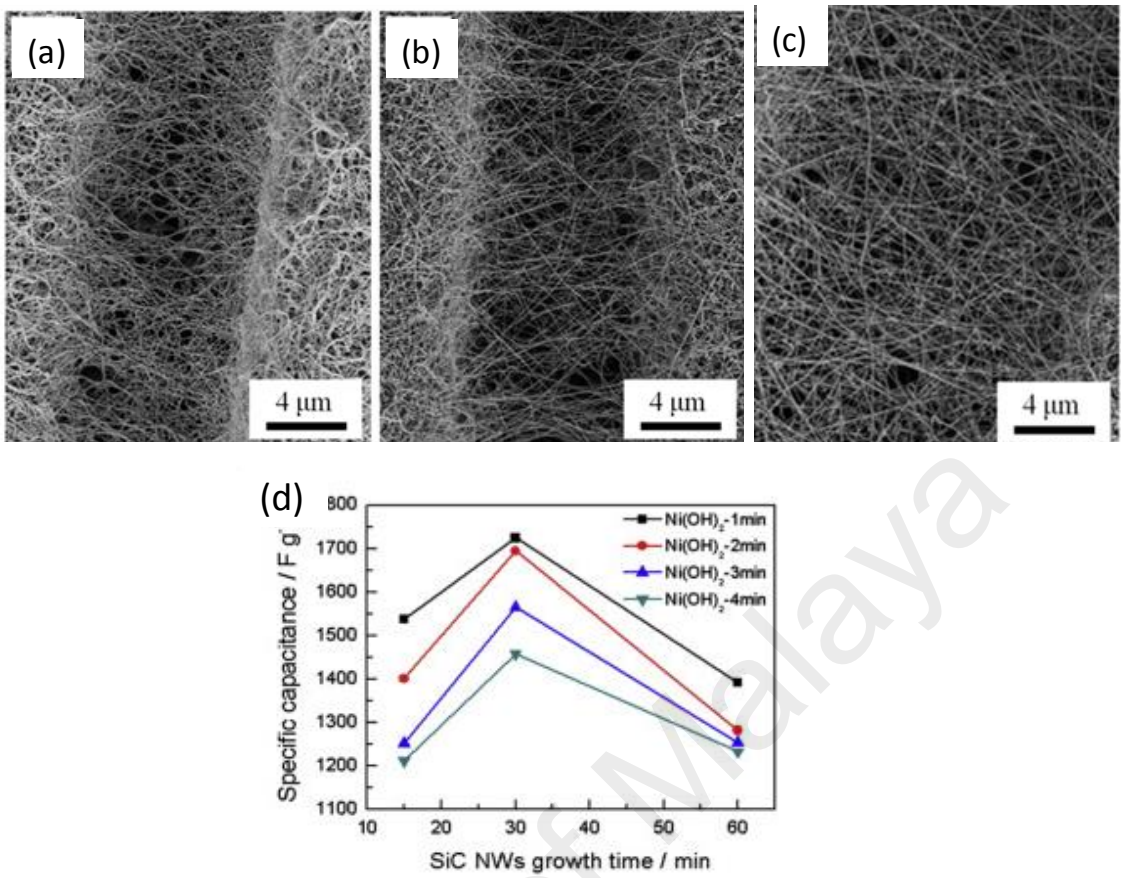

Figure 2.16: (a-c) Morphology of SiC nanowires on carbon fabric with different growth time of 15, 30 and 60 min. (d) Specific capacitances of SiC nanowires/$Ni(OH)_2$ at the current density of 2 A g^{-1}. (Gu et al., 2015)

University of Malaya

CHAPTER 3: EXPERIMENTAL AND ANALYTICAL TECHNIQUES

3.1 Introduction

This chapter described the two main parts of this experimental and analytical techniques used on the NiSi/SiC core-shell nanowires studied. The first parts of this chapter described the deposition system and the sample preparation procedures. This is followed by the description of the substrate cleaning procedures. The second part of this chapter presents the analytical instruments utilized in characterizing the nanowires.

3.2 Deposition System Setup

Most of the samples in this thesis were synthesis in the home-built HWCVD system with the schematic diagram as illustrated in Figures 3.1. The system consists of six parts, namely CVD reactor, plasma generator, hot-wire power supply, vacuum system, gas supply and heating elements. Figure 3.2 shows a photograph of our home-built hot-wire CVD system.

University of Malaya

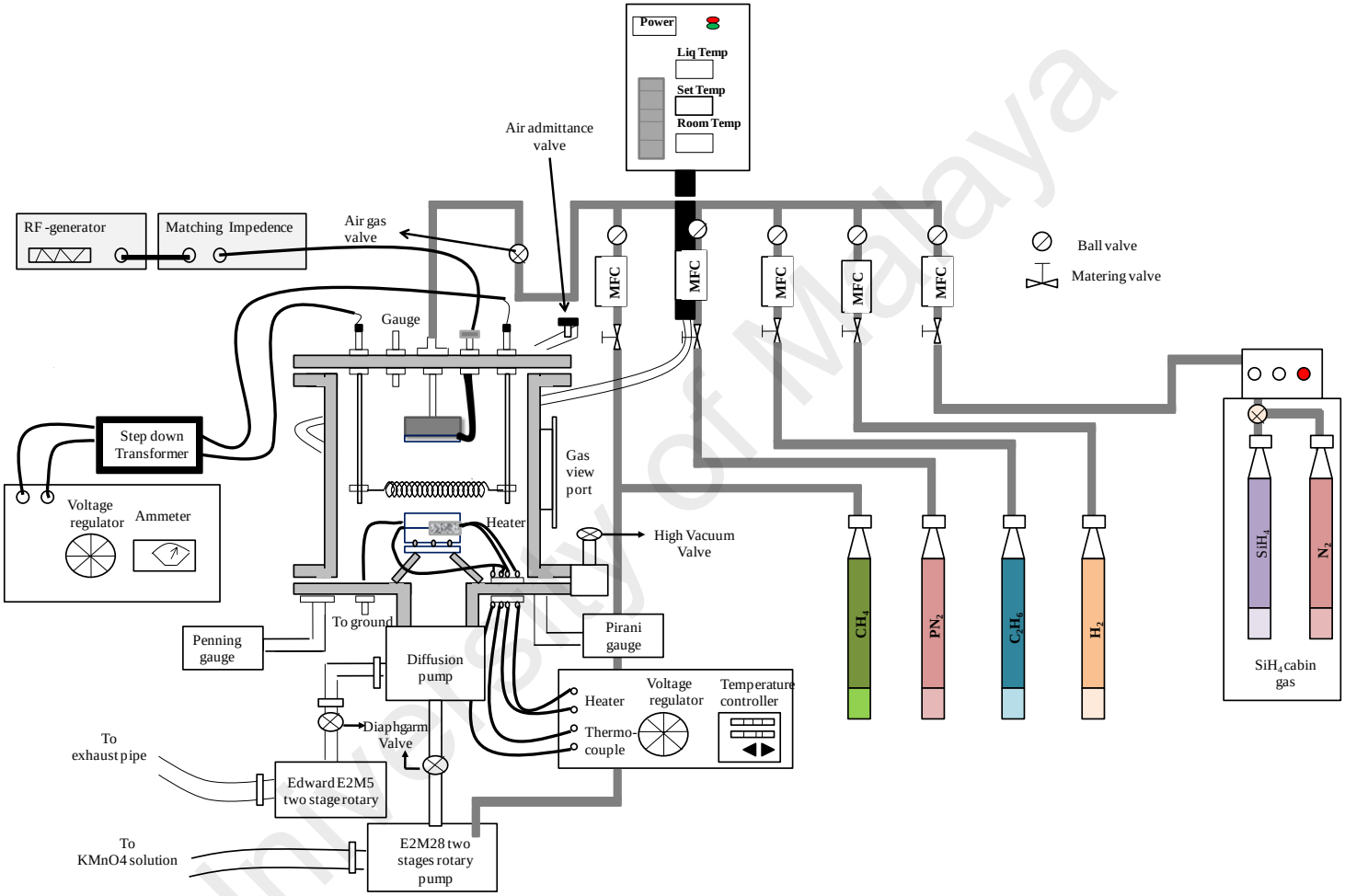

Figure 3.1: Schematic diagram of our home-built hot-wire CVD systems.

University of Malaya

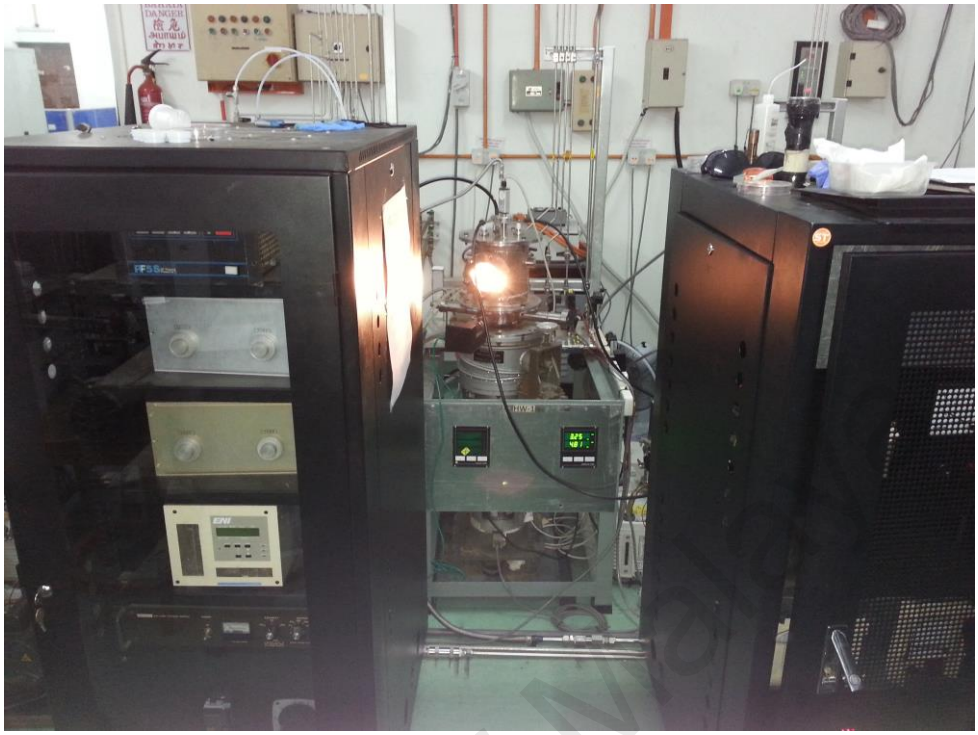

Figure 3.2: Photograph of the home-built hot-wire CVD system.

3.2.1 CVD Reactor

The CVD reactor of this deposition system consists of a cylindrical stainless steel chamber with diameter of 24 cm and height of 22 cm. The cylindrical stainless steel chamber of this CVD reactor is well-sealed with Viton o-rings and is directly connected to a vacuum pump for evacuation. The connecting tube has an air admittance valve for venting purposes. This chamber also has small tubes that connect to water – cooled chiller systems (QC Scientific Precision Cooler) used for cooling purpose. A glass viewport on the body of the reactor is used for viewing interior of the reactor. It also acts as a window for the optical pyrometer used to determine the filament temperature. A stainless steel made substrate holder is designed to hold four pieces of substrate with diameter of 2.5 cm each. The heater rod and thermocouple are attached to the substrate holder which is grounded to the earth and isolated from the body of the reactor by Teflon stands. Figure 3.3 shows a real picture of HWCVD reactor.

University of Ma

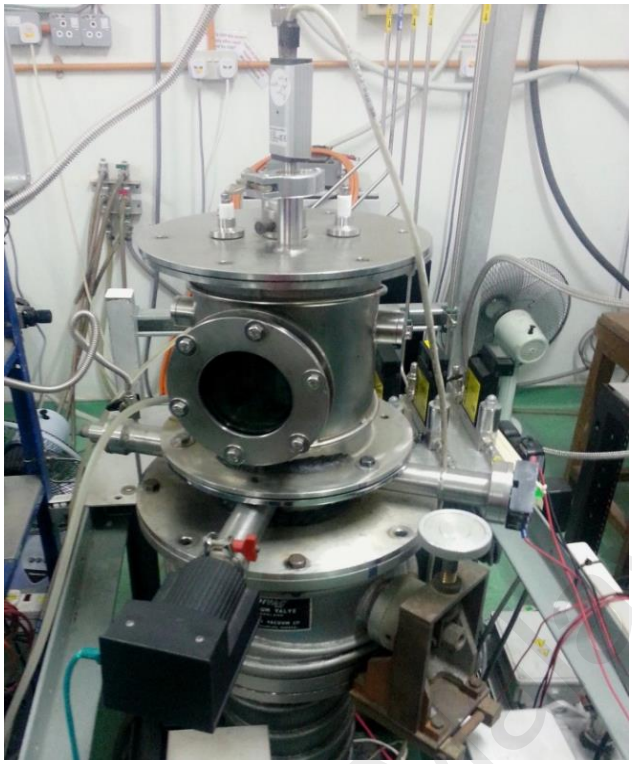

Figure 3.3: Photograph of HWCVD reactor.

3.2.2 Plasma generator

Plasma generator is electrical equipment apply high frequency (13.5MHz) power to produce plasma. A stainless steel electrode-cum-gas showerhead is installed with the gas inlet tube and is placed at a distance of 5 cm from the substrate holder. The thickness and diameter of the electrode is 1 cm and 10 cm, respectively. The electrode is decorated with cone-shaped holes. The inlet and outlet diameter of the hole is 2.2 mm and 1.0 mm, respectively, while the distance between holes is 1.0 cm. Precursor gas can be dispersed uniformly from these holes. The electrode is powered for plasma generation. It is connected to the rf generator via an impedance matching network (shown in Figure 3.4). The plasma is generated between the powered electrode and grounded substrate holder by applying rf power. An impedance matching network is employed to match the load impedance of plasma to the impedance of the DC generator, so that the reflected power from plasma to rf generator can be minimized.

University of Malaya

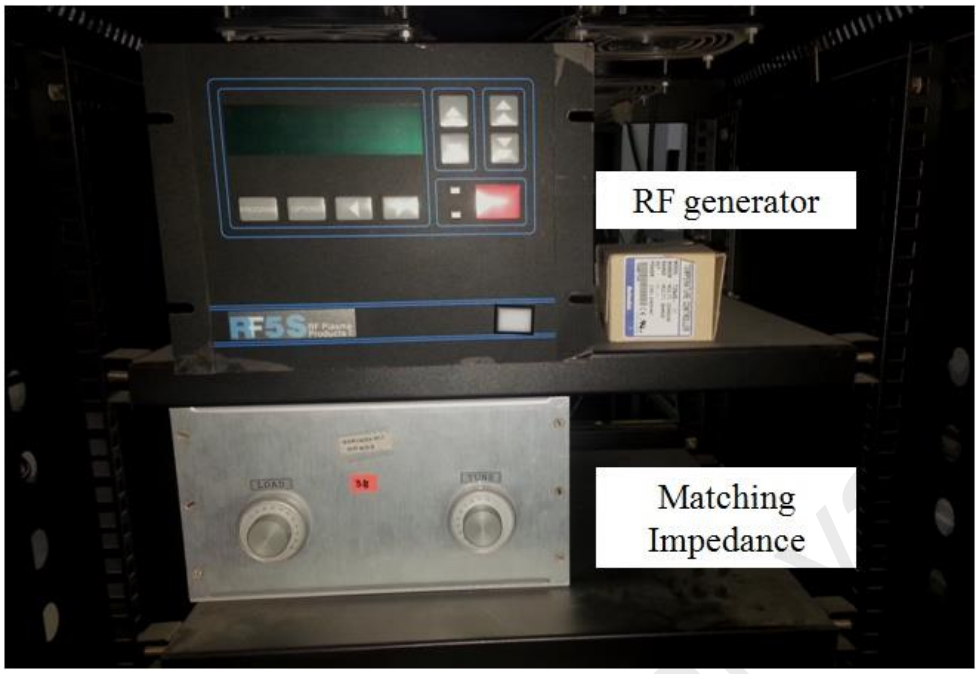

Figure 3.4: Photograph RF generator.

3.2.3 Hot-Wire Power Supply

Tungsten wire (.purity of 99.95 %) is coiled to form a solenoid shaped filament with ~30 coils of diameter 2 mm and length of ~2 cm. This filament coil serves as the thermal energy source for the evaporation of the Ni foil catalyst and decomposition of source gases. The tungsten filament is placed on a filament holder, which connected to a power supply. The power supply consists of a voltage regulator with voltage ranging from 0 – 250 V and a step down transformer. By regulating the voltage supplied to the tungsten filament, different filament temperatures, T_f can be controlled for deposition. An ammeter is connected in series with the voltage supply to measure the current flow through the tungsten filament. T_f is measured by a pyrometer (Reytek, Raynger, 3i). The detector of the pyrometer is stimulated by the incoming infrared energy and produces a signal to the circuitry, which will process the signal and compute the T_f. The tungsten filament is pre-heated to remove surface contaminations such as carbon and other metallic elements before deposition. Figure 3.5(a) shows a photograph of hot-wire

University of Malaya

power supply while Figure 3.5(b) shows a pyrometer used to measure filament temperature.

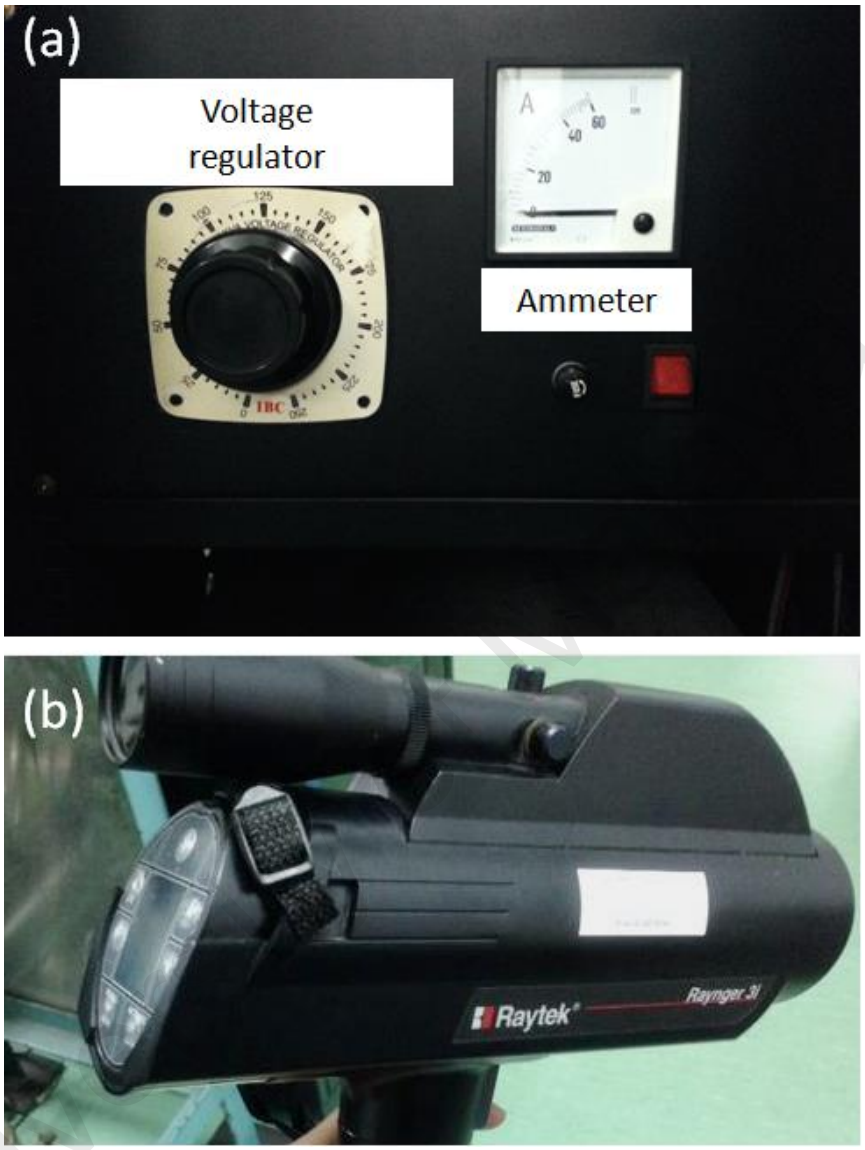

Figure 3.5: Photograph of (a) hot-wire power supply and (b) pyrometer used to measure filament temperatures.

3.2.4 The Vacuum Systems

For the purpose of materials fabrication in CVD, a high vacuum level is important to provide a clean deposition environment and minimize contaminations in the sample. In this system, there are three types of vacuum pumps which comprises of an Edwards E2M28 and Edwards E2M8 rotary mechanical vacuum pumps and an Edward P603 oil diffusion pump. In the early stage of the pumping process, the rotary pump will operate in the viscous region (fore and roughing pump) allowing the pressure to go down to 10^{-3} mbar. The diffusion pump is connected at the bottom of the whole system and is backed by an Edwards E2M8 rotary mechanical vacuum pump. The diffusion pump or high vacuum pump will take over the pumping process in the molecular flow region to further decrease the chamber pressure down to 10^{-6} mbar. This assures that the chamber achieving the lowest possible pressure in order to reduce contamination.

3.2.5 Gas Supply

In the gas distribution systems, the four gases used in this work are SiH_4 (99.9995%), CH_4 (99.9995%), and H_2 (99.999%). Highly purified SiH_4 and CH_4 are used as the precursor gases (shown in Figure 3.6). H_2 gas is used to dilute the SiH_4 and CH_4 gaseous in deposition. In addition, H_2 gas also serves as a precursor in H_2 plasma treatment and pre-heating of coiled tungsten filament process. The SiH_4 gas tank is kept in a secured gas cabinet attached to an exhaust system, which is able to remove any SiH_4 gas in case of leakage. The SiH_4 gas tank has special gas regulator, model AP1510S, which connected to a special purging system. This special purging system is connected to a N_2 gas cylinder that connected to the regulator through a safety system. This safety system is particularly used for SiH_4 gas to stop the gas from flowing into the reaction chamber instantly in the case of emergency.

University of Malaya

From the gas distribution panel, the source gases are introduced into the CVD reactor through the gas lines. Ball valves are used to open or close the gas line, while metering valves are used to roughly control the amount of gas flow. The gas flow rate is accurately controlled by using a mass flow controller (MFC) with unit reading of standard cubic centimeters per minute (sccm). The SiH_4 and CH_4 gas flow rate is controlled by an AALBORG MFC in a flow rate range of 0 – 10 sccm while H_2 gas flow rate can be varied from 0-200 sccm using an AALBORG MFC with a display meter.

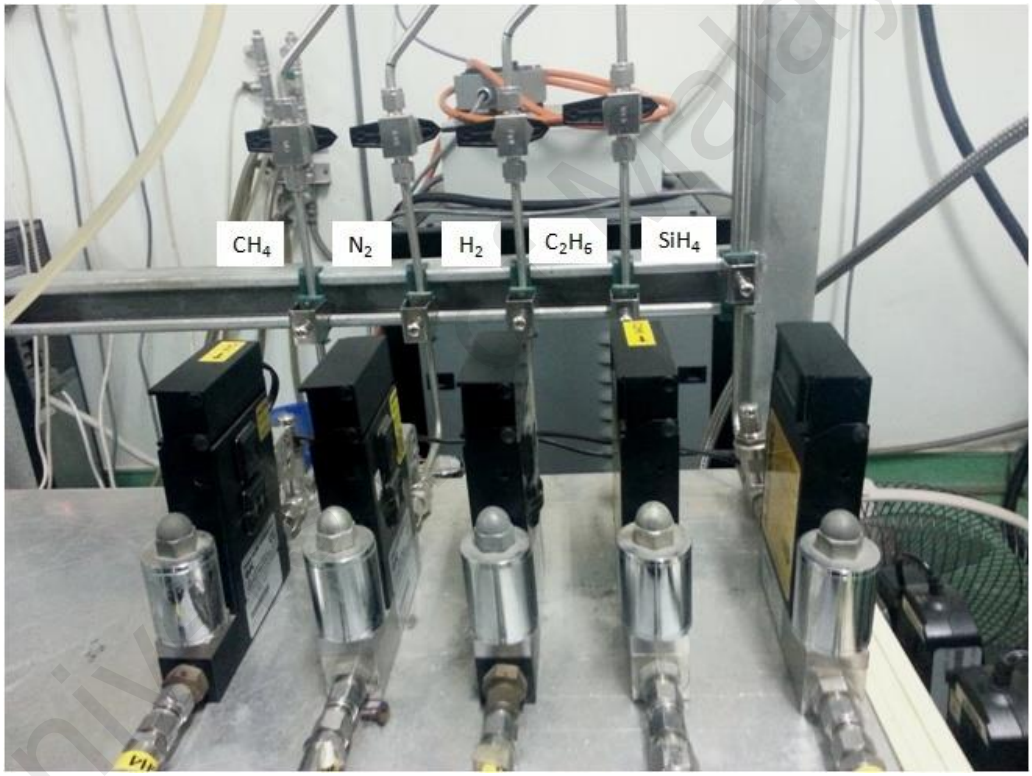

Figure 3.6: Photograph of the gas line.

Universiti Malaya

3.2.6 Heating Elements

In order to prepare the samples, relatively higher substrate temperatures than film deposition are required to melt the metal catalyst or metal-Si alloy. A Watlow Fire Rod SFMH80 A-4183 heater cartridge that used for substrate heating is clamped in between of the substrate holder, so that heat can be transferred from the stainless steel substrate holder to the substrate. The heater cartridge is connected to a voltage regulator (IBC voltage regulator IP-1kVA) and a temperature controller (Taishio TS-501 model) in a loop. The temperature controller is connected to thermocouple (Maltec-T type K thermocouple), installed at the bottom of the substrate in the CVD reactor. The thermocouple is used to directly measure the temperature of the substrate. Figure 3.7 shows a photograph of temperature controller and voltage regulator.

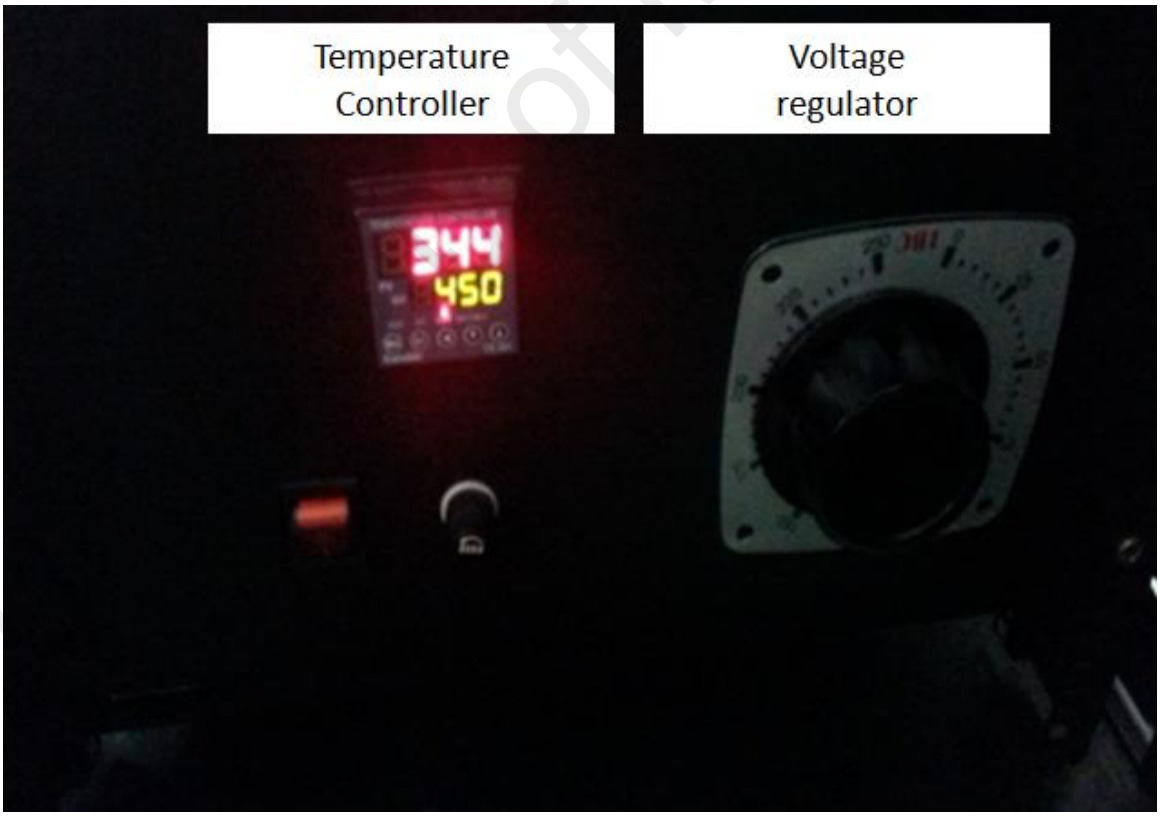

Figure 3.7: Photograph of temperature controller and voltage regulator.

University of Malaya

3.3 Experiment Methods

Experiment method can be categorized into 6 steps, namely substrate cleaning, pre-heated, evaporation process, substrate heating, plasma process and deposition process.

3.3.1 Substrate Cleaning

P-type crystal silicon c-Si (100) and Ni foil substrates were used in this work. The cleaning process is very important to ensure that the purity level is always high and also to remove contaminants on the substrate which may affect the properties of the nanowires deposited on the substrate. The Si substrates were used to study the morphological, and microstructure crystallinity and phase properties while Ni foil was used to study the supercapacitor performances of the nanowire electrodes.

The cleaning process of Si substrates is following the method of Radio Corporation of America (RCA)-I and II cleaning methods (Kern, 1970). The cleaning process for the c-Si substrates begins with rinsing the substrates in the deionized water to remove the contamination during the cutting process. The substrates were then immersed in H_2O:H_2O_2: HCl solution with ratio of 6:1:1 for 5 minutes (37% HCl, M= 36.49 g/mol, diluted in H_2O_2 and deionized (DI) water) to remove residual metal contaminations, such as Al, Mg, and Zn. The process was continued by immersing the substrates in H_2O:H_2O_2:NH_4OH (25% NH_4OH, M = 17.03 g/mol, diluted in H_2O_2 and DI water) with ratio of 5:1:1 for 5 minutes and rinsing them with DI water once again. NH_4OH used to remove organic contaminations and dissolved metal (Au, Ag, Cu, Ni, Cd, Co and Cr) contaminations. After the final rinsing process, the substrates were dried in a stream of N_2 gas.

The cleaning process of Ni foil begins with rinsing the substrates in the deionized water to remove the contamination during the cutting process. The substrates then immersed in highly flammable acetone C_3H_6O (99.5%, 58.08 g/mol) to remove any

University of Malaya

other contaminates. Finally, same like others substrates, the substrates were then dried using N_2 gun blower to prevent the formation of water spots.

3.3.2 Pre-heating filament

The tungsten filament is pre-heated to remove surface contaminations such as carbon and other metallic elements before deposition. The pre-heat treatment is carried out for 10 minutes at T_f ~1600°C in H_2 with flow rate of 100 sccm. Both for Ni evaporation and deposition process required a pre-heated tungsten filament. Figure 3.8 shows tungsten filament before and after pre-heated process.

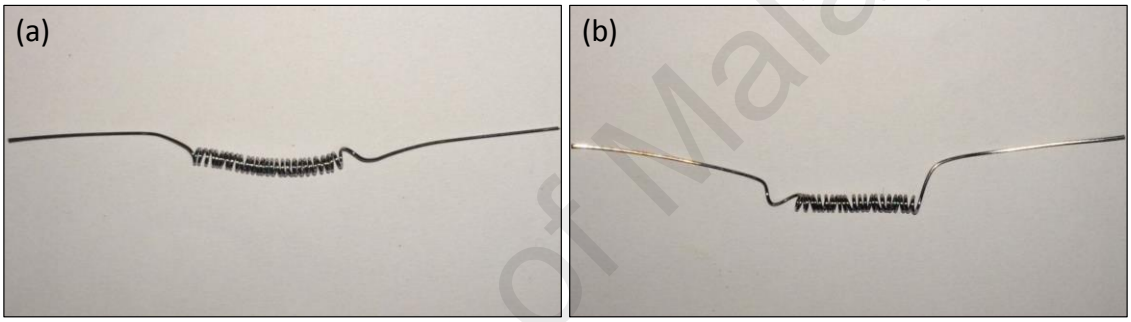

Figure 3.8: Photograph of tungsten filament (a) before and (b) after pre-heated process.

3.3.3 Evaporation Process

The cleaned substrates were put onto the substrate holder and placed into the CVD reactor. Initially, a piece of Ni foil (with a purity of 99.999%) was hung onto the coiled tungsten filament (with a purity of 99.95%) as shown in Figure 3.9(a). The reactor was then tightly sealed. This was followed by the system evacuation. The reactor was first evacuated to a pressure ~10^{-3}. This is important so that all the impurities that may contaminate the film during and after deposition may be reduced. Once the pump achieved the pressure ~10^{-3}, the high vacuum valve was closed and the rotary pumps valve was closed and the high vacuum valve was slowly opened. The system was pumped down to a base pressure of ~10^{-6}. This will assure that the chamber will achieve the lowest possible pressure in order to reduce contamination. Once the base pressure

University of Malaya

had been reached and the system had been pumped down for sufficient time, high vacuum valve was closed and the rotary pumps valve was fully opened again. The evaporation was carried out at a T_f of about 1600°C for 10 min with H_2 flow rate and substrate temperature of 100 sccm and 150°C, respectively to form Ni thin films as shown in Figure 3.9(b).

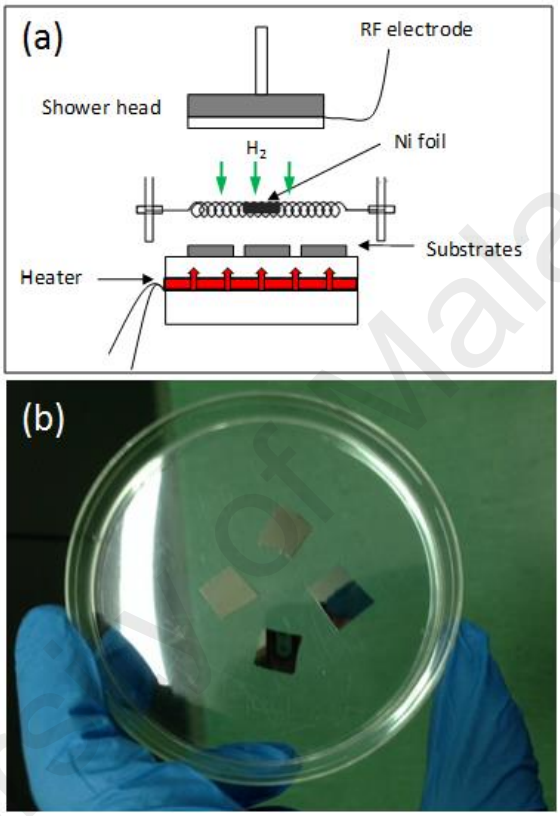

Figure 3.9: (a) Schematic diagram of Ni evaporation process. (b) Photograph of the Ni coated on glass substrates.

3.3.4 Substrates Heating

Similar with evaporation process, the pumping process was done before the substrate heating process. The substrates were heated up first to a certain temperature by using a fire rod heater cartridge, installed at the bottom of the substrate (Figure 3.10(b)). The substrate temperature was directly controlled by using a temperature controller and the heating rate was controlled by a voltage regulator power supply at 165 V (Figure 3.10(a)). The substrate temperature was measured using a Maltec- T type K

University of Malaya

thermocouple (Figure 3.5(c)). When the required temperature was reached, the substrate was annealed for 10 minutes to stabilize it.

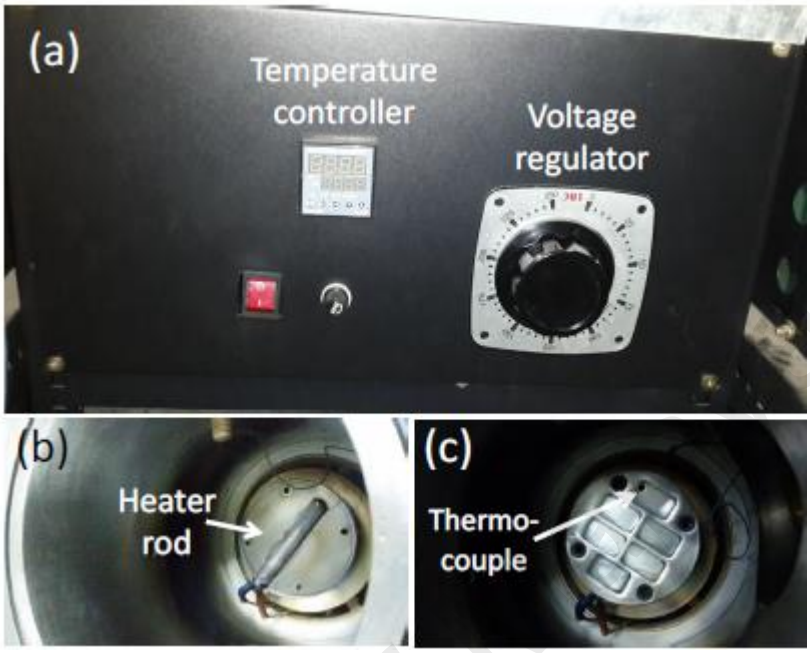

Figure 3.10: Photograph of (a) temperature controller and voltage regulator panels. (b) Heater rod. (c) Thermocouple.

3.3.5 Plasma treatment

After the required temperature was reached and stabilized, the plasma treatment was done first before deposition process. The Ni films were treated by atomic hydrogen plasma for 10 min to form Ni nanoparticles (as shown in Figure 3.11(a)). A large number of spherical shaped Ni nanoparticles were formed after being exposed to the energetic hydrogen plasma at substrate temperature of 450°C and rf power of 5 W. These spherical shaped Ni nanoparticles which were around 36 nm in size were uniformly distributed on the surface of the Ni film. Figure 3.11(b) shows photograph image of plasma treatment.

University of

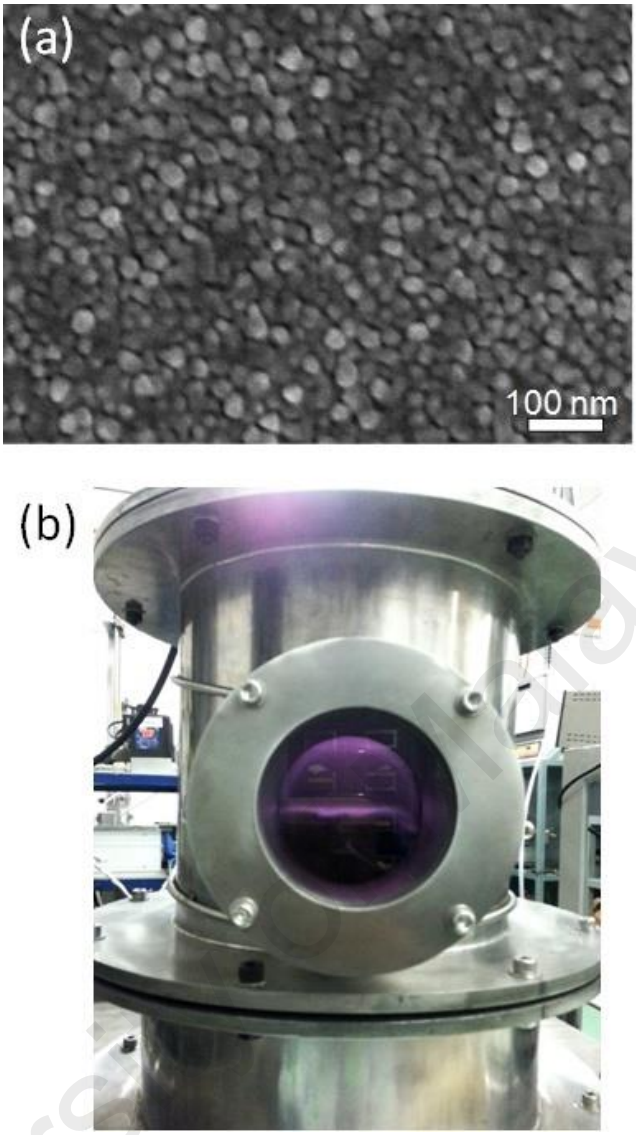

Figure 3.11: FESEM image of the Ni nanoparticles that forms by hydrogen plasma at substrate temperature and rf power of 450°C and 5 W, respectively. (b) Photograph image of plasma treatment process to form Ni nanoparticles.

3.3.6 Deposition Process

During the deposition, the filament temperature was increased to 1900°C by using voltage regulator in order to decompose SiH_4, CH_4 and H_2 gases. The filament temperatures were measured using a pyrometer model Reytek, Raynger 3i. The detector of the pyrometer is stimulated by the incoming infrared energy and produces a signal to the circuitry, which will process the signal and compute the T_f.

Universiti Malaya

The filament-to-substrate distance was kept at 2 cm. The flows of SiH_4, CH_4 and H_2 gases into the reaction chamber were controlled by mass-flow controllers while the deposition time was fixed at 5 min. Figure 3.12(a) shows schematic diagram of decomposition of precursor gases during deposition process while Figure 3.12(b) shows photograph image of deposition process. Table 3.1 shows details of the deposition parameters for each set of samples.

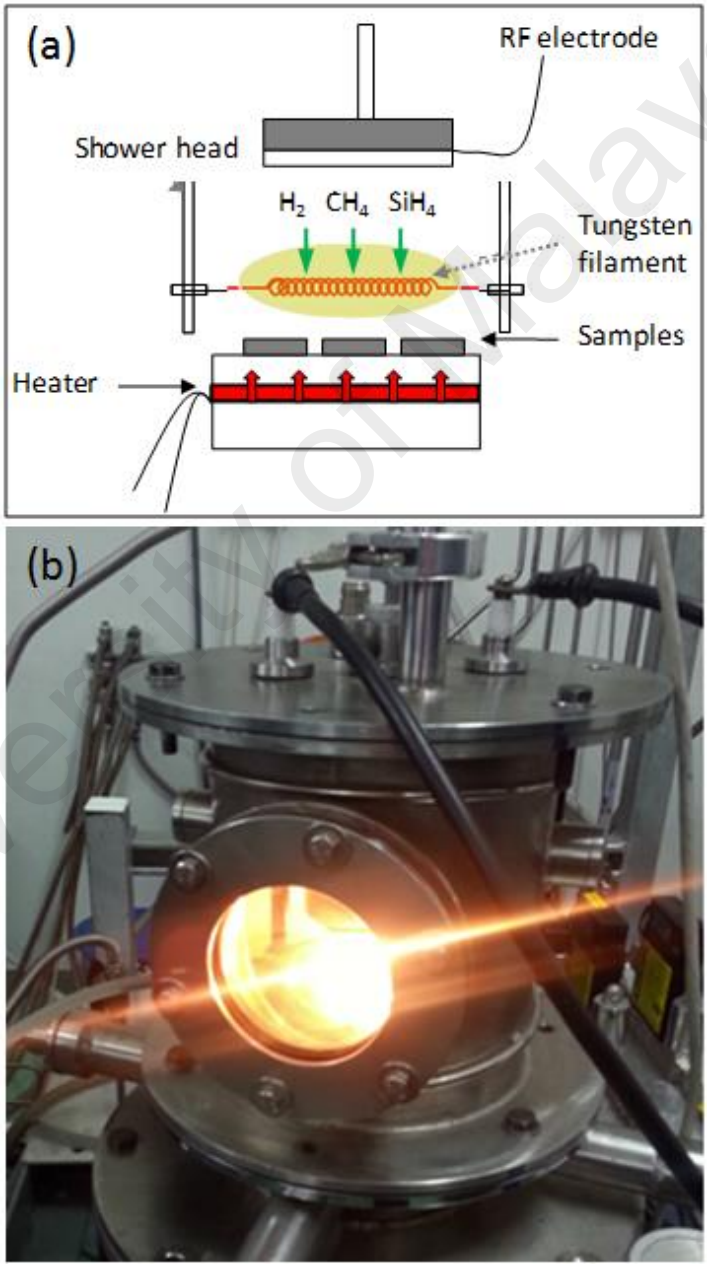

Figure 3.12: (a) Schematic diagram of decomposition of precursor gases during deposition process. (b) Photograph image of deposition process.

University of Malaya

Table 3.1: Details of the deposition parameters for each set of samples.

Set	Variable	Parameters						
		P (mbar)	**rf power (W)**	**Ts (°C)**	**H_2 (sccm)**	**CH_4 (sccm)**	**SiH_4 (sccm)**	**t_d (min)**
1	Substrate temperature	3	5	350	100	2	1	5
		3	5	400	100	2	1	5
		3	5	450	100	2	1	5
		3	5	500	100	2	1	5
		3	5	530	100	2	1	5
2	CH_4 flow rates	3	5	450	100	0.5	1	5
		3	5	450	100	1.5	1	5
		3	5	450	100	2.0	1	5
		3	5	450	100	2.5	1	5
		3	5	450	100	3.5	1	5

University of Malaya

3.4 Analytical Techniques

3.4.1 Field Emission Scanning Electron Microscopy (FESEM)

The characterization on nanostructures is highly dependent on surface morphological imaging technique. In order to view submicron to nanosize of structures, an optical microscope is no longer applicable due to the resolution limit. Electron microscope shows much better resolution and depth of focus due to the natural behavior of electron compared to photon. Thus, scanning electron microscope (SEM) technique is most often used to provide a topographic image of the sample surface. SEM was first invented by Max Knoll and Ernst Ruska in 1931 at the University of Berlin. However, the first scanning electron microscope (SEM) was built in 1938 due to the difficulties of scanning the electrons through the sample. This instrument was the first instrument used accelerated electrons as a source instead of light source (Williams & Carter, 2009).

Figure 3.13(a) shows schematic diagram of main component of a FESEM. The beam of electron is generated by thermionic emission (TE) gun or field emission (FE) gun. The field emission (FE) gun utilizes the field-emission effect that takes place when a high electric field is applied to a metal surface. A FE gun consists of a sharp tip (< 0.1 μm), usually made of tungsten serves as cathode and two anodes (extraction and acceleration anodes). By applying high voltage between the cathode and anodes, electron can tunnel through the energy barrier of tungsten tip into vacuum. Since the electron beam that emitted from emitter in the FE gun produced a small electron source with a diameter of 5 to 10 nm, thus make it suitable for high-resolution SEM as compared to thermionic emission (TE) that produce electron source with diameter of 10 to 20 μm.

The extraction anode (0-5 kV) acts to extract the electron while the acceleration anode (1-50 kV) acts to accelerate the electron by increasing the applied voltage. After the electron pass through extraction and acceleration anode, it will pass through a

University of Malaya

system of apertures and electromagnetic lenses to produce a thin beam of electron. This electromagnetic lens are consists of coils of copper wire inside iron pole pieces (solenoid). Then, the beam scans the surface of the specimen by means of scan coils. The incident electron beam with energy of a few hundred eV to 50 keV interacts with the sample atoms and generates a number of signals. The signals are detected and measured by a detector and transformed into a digital format of image. Morphology study for the FESEM images of the nanowires in this study were obtained by using a Hitachi SU 8000 SEM at low electron accelerating voltage of 2 kV. Figure 3.13(b) shows photograph of a Hitachi SU 8000 SEM. Dimension and density of NiSi nanoparticles and NiSi/SiC core-shell nanowires were measured by using Image-J software.

As shown in Figure 3.13(c), accelerated electrons in an SEM carry significant amounts of kinetic energy, and this energy is dissipated as a variety of signals produced by electron-sample interactions when the incident electrons are decelerated in the solid sample. These signals include secondary electrons (that produce SEM images), backscattered electrons (BSE), photons (characteristic X-rays that are used for elemental analysis and continuum X-rays), auger electron and visible light (cathodoluminescence–CL). Secondary electrons and backscattered electrons are commonly used for imaging samples. Secondary electron gives information about the surface morphology of the sample while backscattered electron provides information about the chemical distribution up to deeper site rather than the surface morphological study of the sample. Secondary electron imaging mode is primarily focused in the region close to the sample surface (< 10 nm) due to its low energy which excludes the electron extraction from deeper layer of sample. Thus, secondary electron is important in the surface topographical study of the materials.

University of Malaya

Different from secondary electron, backscattered electron has much higher energy (few of keV) which can be utilized to identify the distribution of different elements by determining the contrast of the imaging. The intensity of the backscattered electron signal increases with the increasing of the atomic number of the elemental composition in sample. Thus, elements with higher atomic number appear brighter than the lower atomic number on the backscattered electron imaging. Meanwhile, X-ray photons and Auger electron can be emitted when the inner shell of sample atom collides with the incident electron. During the collision, the electron in the inner shell of the sample atom can be ejected from the atom, leaving an inner shell vacancy. The vacancy can be occupied by an outer shell electron and results in photon emission. The energy difference between the two shells is equivalent to the photon energy of the electromagnetic radiation in X-ray regime. Besides the X-ray radiation, the ejected electron known as Auger electron occurs when excessive energy is transferred to another outer shell electron and this promotes the ejection of the electron from the atom shell.

Figure 3.14 shows SEM images of SiC@Si core-shell nanowires taken by a Hitachi SU 8000 (Wang et al., 2015). Figure 3.14(a) show low magnification SEM image of nanowires while Figure 3.14(b) shows the magnified SEM of the nanowires. At low magnification SEM image of nanowires, no nanowires can be seen from this image. After magnified this image, the nanowires were stacked together, closed to the surface of carbon paper substrate were clearly been shown in this image. The length and diameter also can be calculated from this image. The length of SiC nanowires was typically longer than 10 mm and the diameter were ranged from 20 nm to 50 nm.

University of Malaya

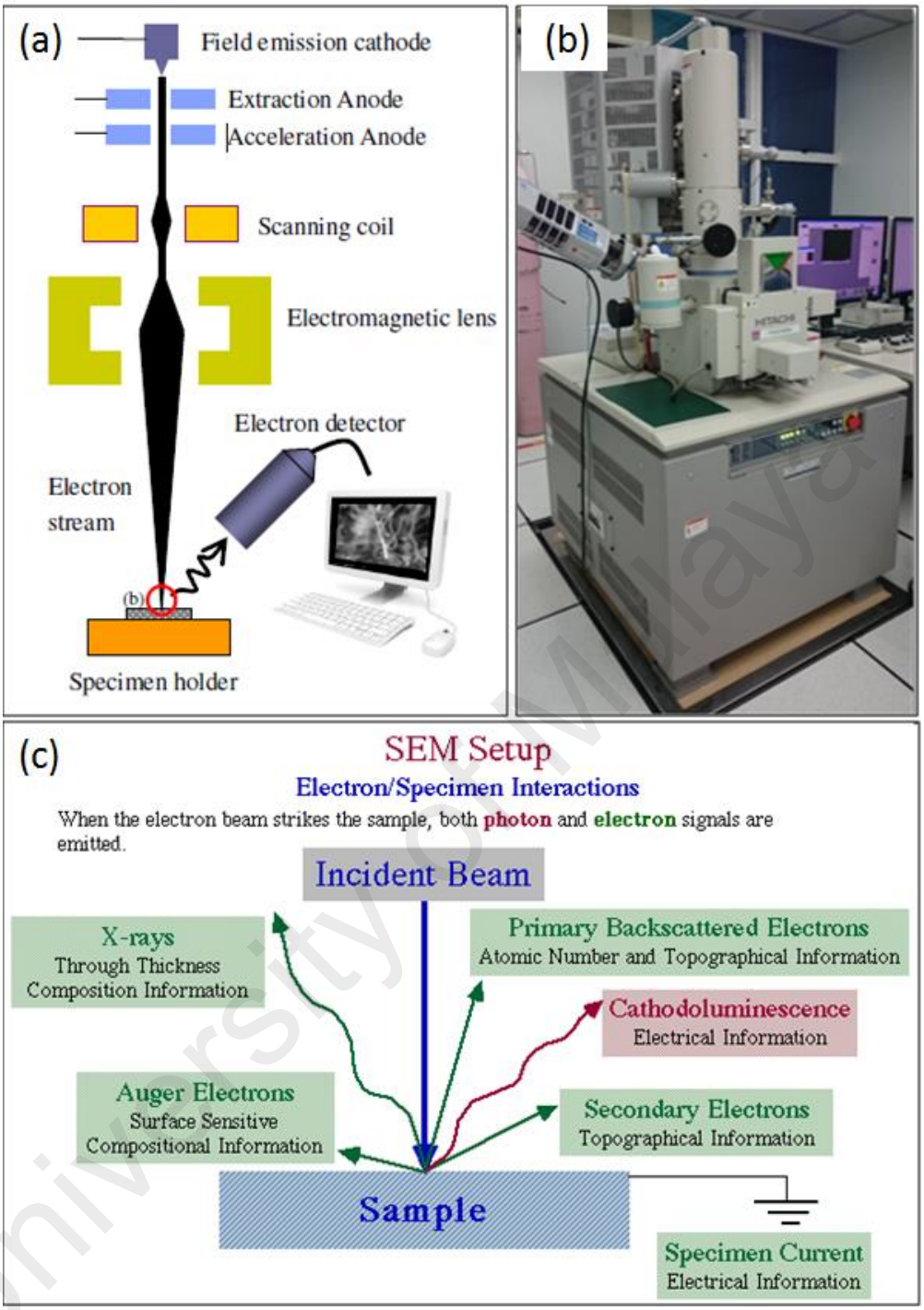

Figure 3.13: (a) Schematic diagram of the main components of a FESEM. (b) Photograph of Hitachi SU 8000 SEM. (c) Schematic of the signals generated when the electron beam strikes the specimen.(Leonard et al., 2002)

University of Malaya

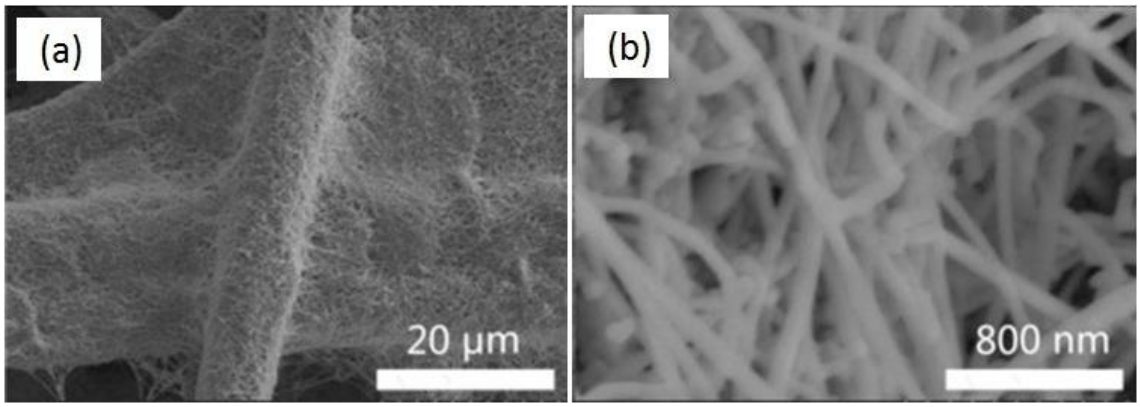

Figure 3.14: (a&b) Low and magnified image of SEM images of SiC@Si core-shell nanowires grown on carbon paper. (Wang et al., 2015)

3.4.2 Transmission electron microscopy (TEM)

Transmission electron microscopy (TEM) is a well-established technique for studying the crystallinity and microstructure of the nanowires. Atomic structure of a nanowire can be directly investigated by employing high resolution transmission electron microscopy (HRTEM). A high resolution of ~1 Å is theoretically obtained in a HRTEM due to the shortening in de Broglie wavelength of the high energetic electron beam. This is useful in determination of the crystalline or amorphous structures and structure defects such as twinning and lattice dislocation within nanowire. It can also be used to identify the atomic lattice spacing, crystalline plane, preferred orientation and growth direction of the nanowires. The high resolution TEM has been widely used to characterize the quality of both the nanowire core and the shell. Historically, the first transmission electron microscopy (TEM) were first build by Ruska and his research group in Berlin in 1931 by implement Busch's lens formula experimentally (Bogner et al., 2007).

Figure 3.15(a) show a simplified schematic diagram of a typical TEM. Electrons are extracted from a filament or a field emission tip with a large accelerating voltage ranging from 100 to 1000 kV. The electrons pass through the condenser lens system where the electron beam is condensed to a smaller size. The condenser lenses are fitted

University of Malaya

with apertures, which control the intensity of the electron beam. The condensed electron beam is incident on the sample, through which electrons are transmitted and scattered. The electrons that are elastically scattered consist of the transmitted beams, which pass through the objective lens. The objective lens forms the image display and the following apertures, the objective and selected area aperture are used to choose of the elastically scattered electrons that will form the image of the microscope. Finally, the beam goes to the magnifying system that is consisted of three lenses, the first and second intermediate lenses which control the magnification of the image and the projector lens. The formed image is shown either on a fluorescent screen or in monitor or both and is printed on a photographic film.

In order to obtain higher resolution (up to atomic level), the sample should be thin enough (< 100 nm) to enable the transmission of the electron beam. A TEM grid, usually copper grid with carbon supporting film, is used to hold the sample. Lacey 300 mesh Cu is used in this work. The samples on the substrate were immersed in isopropanol solution and sonicated for about 15 minutes to extract the nanowires from the substrate. The diluted nanowire in an isoprapanol solution was then transferred onto a copper grid through a cleaned pipette. The copper grid was dried in a dry cabinet for a few hours before proceed for TEM imaging. In this research, the TEM and high-resolution TEM images of the nanowires were collected using a TEM (JOEL JEM-2100F) with an accelerating voltage of 200 kV (Figure 3.15(b)). Figure 3.15(c) shows a schematic of the signals generated when the electron beam strikes the specimen in the HRTEM. There are three types of transmitted electrons such as unscattered, elastically scattered and inelastic scattered electrons. The electrons that transmitted through the specimen without any interaction with specimen atoms called unscattered electrons. These unscattered electrons mainly contribute to the TEM images. Elastically scattered electrons are generated when the incident electrons are scattered by the specimen atoms

University of Malaya

with no loss energy. The elastically scattered electrons follow Bragg's diffraction law, where the incident electrons are scattered by the atoms with the same atomic spacing and possess same scattering angle. The same angle of scattered electrons forms a pattern of diffraction spots. This diffraction pattern is utilized to generate selected area electron diffraction (SAED) pattern, which gives information on the structures (amorphous or crystalline), orientation and atomic arrangement of the sample (Williams & Carter, 2009).

Figure 3.16 shows a typical TEM and HRTEM of SiC core-shell nanowires. Figure 3.16(a&b) depicts the nanowires consist of a dark inner core of 100 nm in diameter and a light outer shell of 30-40 nm in thickness. The SAED pattern (inset in Figure 3.16(b)) confirms that the core was single crystalline 3C-SiC. The shell layer comprises amorphous SiO_2, which was further verified by HRTEM. The marked interplanar d-spacing in Figure 3.16(c), measuring 0.25 nm, matches well with the (111) lattice plane of 3C-SiC. The lattice fringes, along with the SAED pattern (in Figure 3.16(b)) of the core, suggest that [111] was the growth direction of the core 3C–SiC nanowire. In addition, a few typical core areas of nanowires exhibit obvious defect characteristics which also suggest that the core of nanowires was single crystalline SiC, and was further identified by the SAED pattern (Figure 3.16(d)).

University of Malaya

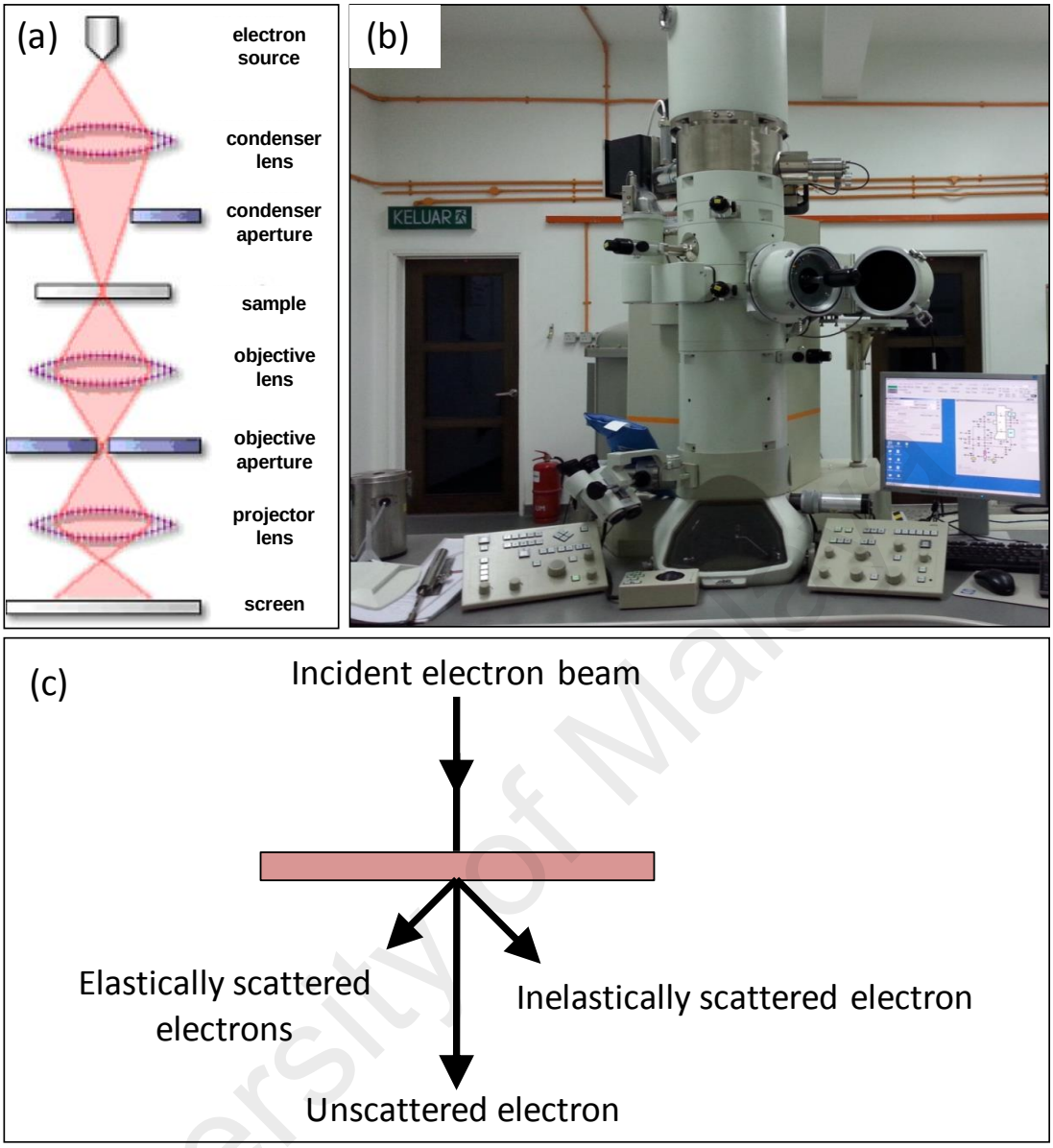

Figure 3.15: (a) Schematic diagram of TEM. (b) Photograph of TEM (JOEL JEM-2100F) with an accelerating voltage of 200 kV. (c) Schematic of the signals generated when the electron beam strikes the specimen in the HRTEM. (Williams & Carter, 2009)

University of Ma

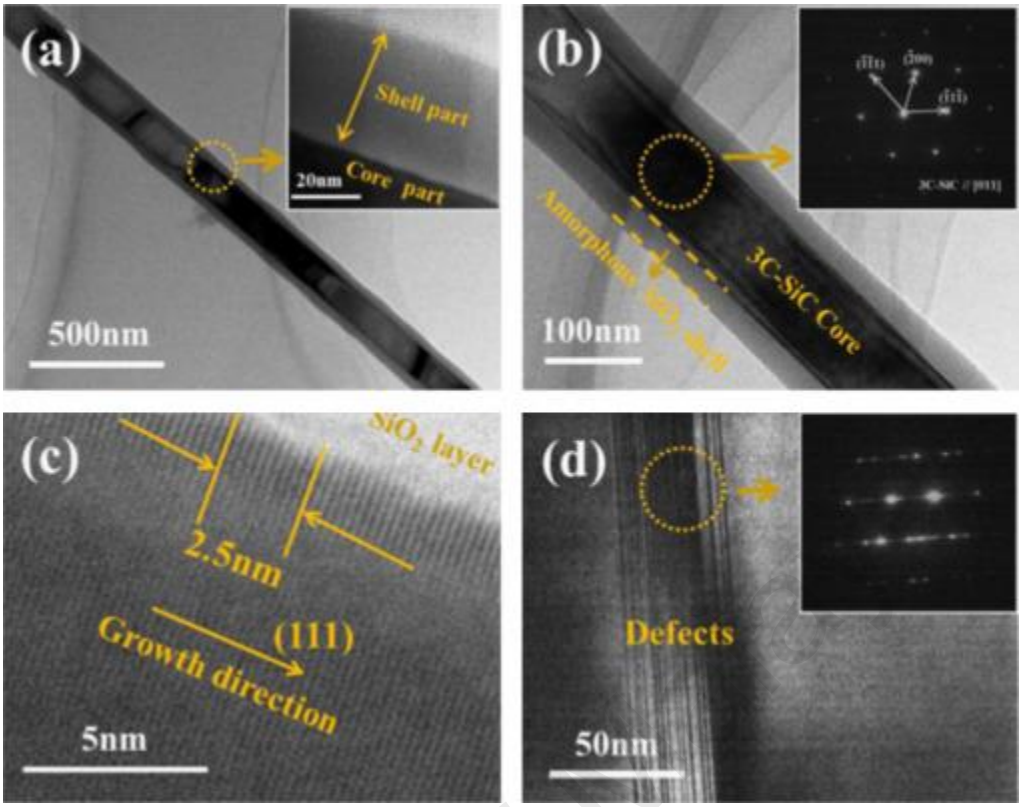

Figure 3.16: (a) Low-magnification TEM image. (b) High-magnification TEM image and the inset in the top right corner of (b) shows the corresponding SAED pattern of the core of nanowire. (c) A typical HRTEM image of the as achieved nanowires. (d) A typical area and its corresponding SAED. (Zhang et al., 2016)

3.4.3 Energy Dispersive X-ray Spectroscopy

Energy-dispersion X-ray spectroscopy (EDX) is an analytical method for qualitative as well as quantitative determination of elements in a sample, independent of their chemical form. It is built on the fact that elements that are irradiated with high-energy X-rays have certain probability of emitting characteristic X-rays. The EDX detector can be attached in a SEM or TEM to effectively collect the X-ray radiation from the sample.

After the discovery of X-rays in 1895, researchers soon realized that the X-rays emitted by excited atoms are intimately connected with their atomic structure. As the atomic structure of each element is different, it follows that, when stimulated, each element emits a specific pattern of X-rays. Then, in 1948, a prototype for the first modern commercial x-ray spectrometer was developed. In the following year, the first electron microprobe was built. The principles were the same, but the source of

University of

excitation was a beam of electrons rather than X-rays. Then, in the mid-sixties, a semiconductor radiation detector was developed at the Lawrence Berkeley Laboratory that heralded the advent of energy-dispersive x-ray spectrometry, or X-ray energy spectrometry (XES) (Goldstein et al., 2012).

Figure 3.17(a) shows an EDS system. EDS system typically consists of several key units such as semiconductor detector housed with a field-effect transistor (FET) preamplified, cooled to a sub-ambient temperature, and a main amplified that provides further amplification and a fast pulse inspection function. All of this can be fully controlled with a computer-assisted system. When the electron beam hits the sample, the X-ray will be generated. The resulting X-ray escapes the sample and hits the detector which creates a charge pulse in the detector. This short-lived current is then converted into a voltage pulse with amplitude reflecting the energy of the detected X-ray. Finally, this voltage pulse is converted to digital signals and once the measurement is completed, the accumulated counts produce a typical X-ray spectrum. The basic principle of EDS shows in Figure 3.17(b). When an electron (from the beam) strikes an atom in a sample, it ejects an electron originally positioned in an inner shell (K shell). In order to return the atom to its normal state, an electron from an outer atomic shell drops into the vacancy in the inner shell. This drop results in the loss of a specific amount of energy, namely, the difference in energy between the vacant shell and the shell contributing the electron. This energy is given up in the form of electromagnetic radiation x-rays (Ngo, 1999). In this work, the elemental analysis and mappings for the nanowire were carried out by using STEM/HAADF and Oxford EDX detectors.

Figure 3.18(a&b) shows the TEM images of V_2O_5@C core-shell nanowires clearly showed that a layer of carbon shell was uniformly covered onto the V_2O_5 nanowire surface. The SAED image as shown in Figure 3.18(b) clearly reveals that the V_2O_5@C core-shell was highly crystalline. The TEM image (Figure 3.18(c)), confirmed

University of Malaya

the core-shell structured of the nanowires. The EDS mapping shown in Figure 3.18(d&e), reveals the V and C were uniformly distributed on the nanowire. Moreover, the distribution of C was mainly located at the outer of the nanowire, confirmed the core-shell structure of V_2O_5@C nanowires. Based on the EDS spectrum shown in Figure 3.17(f), only V, O and C singles were detected, indicating the high purity of the V_2O_5@C nanowires. The atom ratio of V and O was about 14.49: 33.41, which was closed to the ratio of V_2O_5 (Guo et al., 2015).

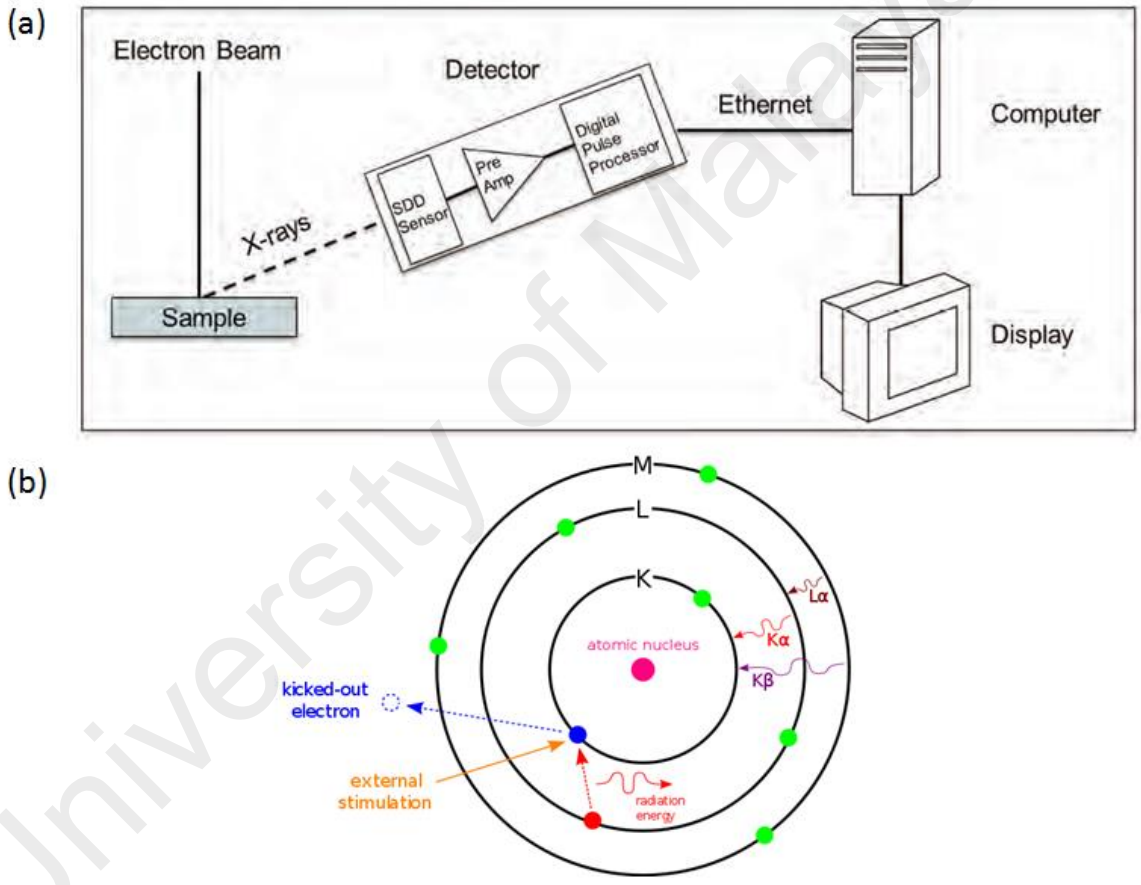

Figure 3.17: (a) The EDS system. (b) The EDS principle. (Ngo, 1999)

University of Malaya

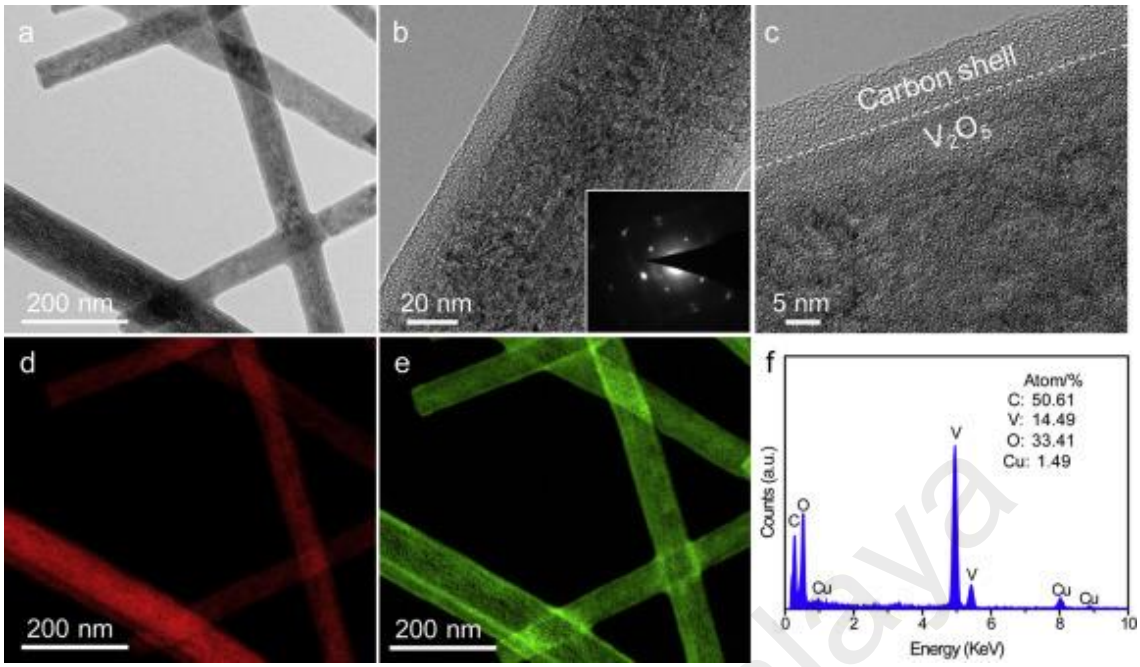

Figure 3.18: (a&b) TEM images. (c) HRTEM image, (d) V elemental mapping. (e) C elemental mapping. (f) EDS spectrum of the nanowires. (Guo et al., 2015).

3.4.4 Micro -Raman Spectroscopy

Micro- Raman spectroscopy is used for investigating the structural properties, including crystallinity, crystalline to amorphous phase transition or vice versa, and crystalline (or amorphous) phase distribution. Raman was recognized as a principle means of non-destructive chemical analysis. Raman phenomenon was detected in 1928 by the Indian physicist C.V. Raman and K.F. Krishnan. During the 1930s, this phenomenon was also reported by Grigory Landsberg and Leonid Mandelstam. After the end of 1920's, this phenomenon was forgotten for several decades because the signal was very weak. Later, when the lasers were invented in 1960, there was revived interest in the Raman spectroscopy (Castner, 2005).

Figure 3.19(a) shows the schematic diagram on how Raman spectroscopy works. When a sample is irradiated with intense monochromatic light source (usually a laser), most of the radiation is scattered by the sample at the same wavelength in all directions. This scattered known as Rayleigh scattering. However, a small proportion of the incoming light- approximately one photon out of a million is scattered at a wavelength

University of Malaya

that is shifted from the original laser wavelength. In this research the Raman spectra of the samples were recorded using an InVia Raman microscope with a charge-coupled device detector and a diffraction grating of 2400 lines/mm. An argon-ion laser with excitation wavelength and laser power of 514 nm and 10 mW respectively was used. Figure 3.19(b) shows a photograph of InVia Raman spectroscopy. Figure 3.19(c) illustrated the simplified energy level diagram of Raman scattering phenomena that consists of Rayleigh, Stokes and anti-Stokes scattering. There are two categories of light scattering occurs in Raman spectroscopy: elastic scattering where the scattered radiation is at the same frequency as the incident radiation (called as Rayleigh scattering), and inelastic scattering where the scattered radiation is at a different frequency (Stoke and anti-Stoke scattering). In Rayleigh scattering, the photon energy and molecular energy are both separately conserved while for inelastic scattering, the total photon plus molecular energy is conserved but the vibrational energy changes and frequency shifts occur in the scattered radiation. There are also present two different types of Raman scattering phenomena namely Stokes scattering and anti-Stokes scattering which are distinguish by whether the frequency of incident light is shifted up or down. Stokes scattering occurs when the incident radiation is shifted to a lower frequency (lower energy) while anti-Stokes scattering occurs when the incident radiation is shifted to a higher frequency (higher energy).

At room temperature most of the molecules are in the ground vibrational state (v=0) and which a much lower population in the first vibrational excited state (v=1). When incident light hits a molecule, an electron in ground vibrational state is promoted to a virtual state. It then relaxes and returns to the same vibrational state from which it started. This process results in Rayleigh scatter, which is scattered light of the same wavelength as the excitation laser. In Stokes scattering, the electron also begins in the ground vibrational state. It is promoted to a virtual state and then relaxes to an energy

University of Malaya

state that is higher than the electron's starting state. For anti-Stokes scattering, an electron begins in a vibrational state that is more energetic than the ground state. It is promoted to a virtual state then relaxes back down to the ground vibrational state, which lower in energy than when it started.

Figure 3.20 shows a typical Raman spectra of $SiC@SiO_2$ core-shell nanowires obtained by Renishaw InVia Raman spectroscopy (Attolini et al., 2010). The Raman peaks corresponded to the transverse optic (TO) and longitudinal optic (LO) modes at 797.3 cm^{-1} and 976.2 cm^{-1} indicated the formation of β-SiC core. There also presented the formation of vibrational modes from 500 to 750 cm^{-1} due to presence of the SiO_2 shell.

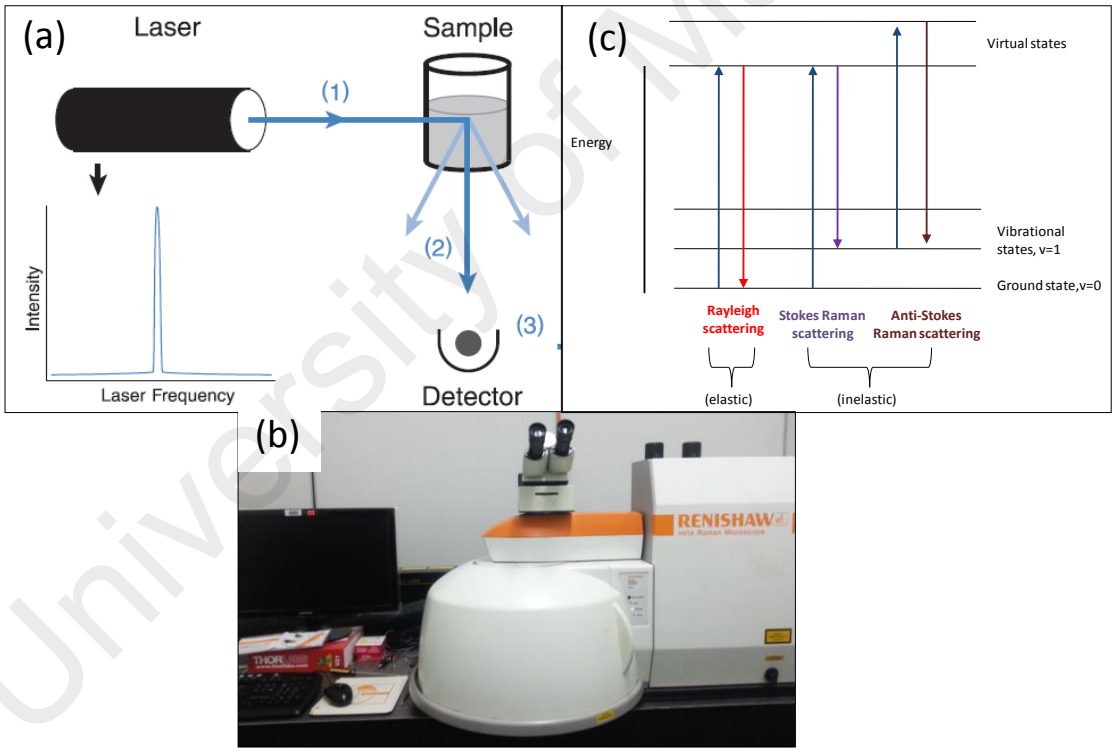

Figure 3.19: (a) Schematic diagram on Raman excitation principle. (b) Photograph of InVia Raman spectroscopy. (c) Energy level diagram of Raman scattering phenomena. (Laserna, 2006)

University of Malaya

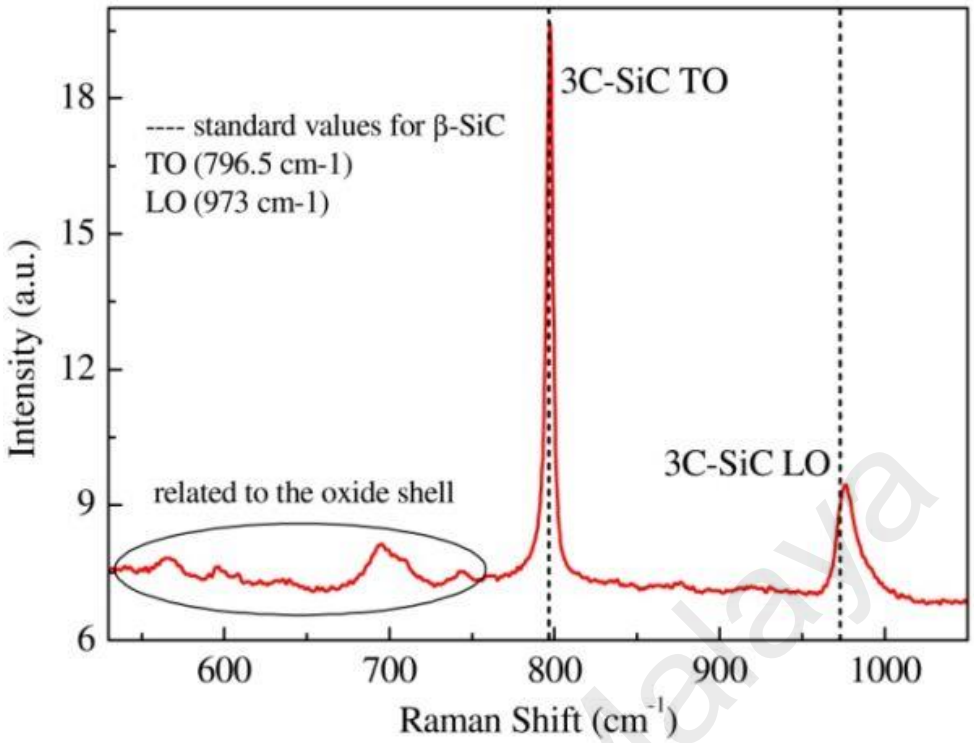

Figure 3.20: Raman spectrum of SiC@SiO_x core-shell nanowires (Attolini et al., 2010).

3.4.5 X-ray Diffraction (XRD)

X-ray diffraction (XRD) is a powerful method for the study of nanomaterials (materials with structural features of at least one dimension in the range of 1-100 nm). Crystal of an element can be identified by determining the peak position in XRD pattern, while the orientation plane corresponding to the peak can be assigned. XRD provides a qualitative determination of the crystallinity of a material by analyzing the intensity of the diffraction peak. Crystallite size of the material can be quantitatively calculated from the width of the diffraction peak using several methods (Langford et al.1986; Patterson, 1939).

X-ray diffraction were first discovered by Wilhelm Conrad Röntgen discovered 1895. The properties of these X-rays were investigated and by 1912 the principles of diffraction physics and reciprocal space were developed by Rontgen, von Laue, Ewald, Sommerfeld and Brentano in Munich, Germany. In 1914, W. H. Bragg (father) and W.

University of Malaya

Lawrence Bragg (son) had exploited the phenomenon to solve the first crystal structure and determined the rule governing the diffraction pattern as:

$$2d\sin\theta = n\lambda \quad (3.1)$$

where d is the spacing between diffracting planes, θ is the incident angle, n is any integer, and λ is the wavelength of the beam (right) (Jenkins, 2006). A schematic diagram of X-ray diffractometer is illustrated in Figure 3.21(a). X-ray diffractometers consist of a monochromatic X-ray radiator and a detector which is placed on the circumference of a circle centered on the sample. X-rays are generated in a cathode ray tube by accelerating electron towards a Cu anode plate. CuKa is commonly used as X-ray source. The produced X-ray beam is then filtered by monochromator to a wavelength of 0.7 to 2 A and collimated towards sample. The X-ray beam diverges from the source and diffracted by the sample to form a convergent diffracted beam. The convergent diffracted beam is filtered by a monochromator and focused at a slit, then enters the detector. Intensity of the diffracted X-ray beam is measured as the number of current pulses per unit time by an electronic X-ray detector. During the measurement, the X-ray detector is mechanically rotated in an angle of 2θ accompanied by a rotation of sample holder in an angle of θ, while the angle of incident beam to sample holder always keeps at θ. Thus, the angle of incident beam is always equal to the angle of diffracted beam. The detector measures data of each angular increment in a minimum order of 0.01°, while the length of time per count and step size of the angular increment are controlled by the computerized programmed (Fultz & Howe, 2013).

In this research, the X-ray diffraction (XRD) patterns of the samples were recorded over the 2θ range of 20–70° at a fixed grazing incidence angle of 1.5° using a PANalytical Empyrean X-ray diffractometer with X-ray wavelength of 1.5406 Å. The step time and step size of the scanning were fixed at 2 s and 0.026°, respectively. The raw data from XRD measurement is then transferred to PANanalytical X'pert Highscore

University of Malaya

software to analyze the atomic structure. Figure 3.21(b) shows photograph of PANalytical Empyrean XRD diffrometer. Figure 3.21(c) show schematic diagram of Bragg's law. Based on Bragg's law, when the X-ray scattered by all the atoms in all of the planes are completely in phase, the constructive interference are formed and the X-rays are diffracted at maximum intensity. This results in the diffraction peak in XRD pattern. The intensity of the diffraction peak is proportional to the degree of crystallinity of the sample. In the rest of angles, the scattered rays cancel out each other (destructive interference) (Sharma et al., 2012).

Figure 3.22 shows an XRD spectra of typical SiC nanowires and SiC@SiO_2 core-shell nanowires measured performed on a PANalytical EMPYREAN instrument in range of 20-80° (Hu et al., 2016). The distinct diffraction peaks at 35.6°, 41.5°, 60.0°, 71.8° and 74.5° are attributed to the (111), (200), (220), (311) and (222) of 3C-SiC (cubic β-SiC), respectively. A minor shoulder peak at around 34° was ascribed to stacking faults (marked with SF) of SiC nanowire. Apparently, besides those mentioned above, a broad hump at about 25° could be observed for SiC@SiO_2 core-shell nanowires, which confirms the existence of low-crystallized SiO_2.

University of Malaya

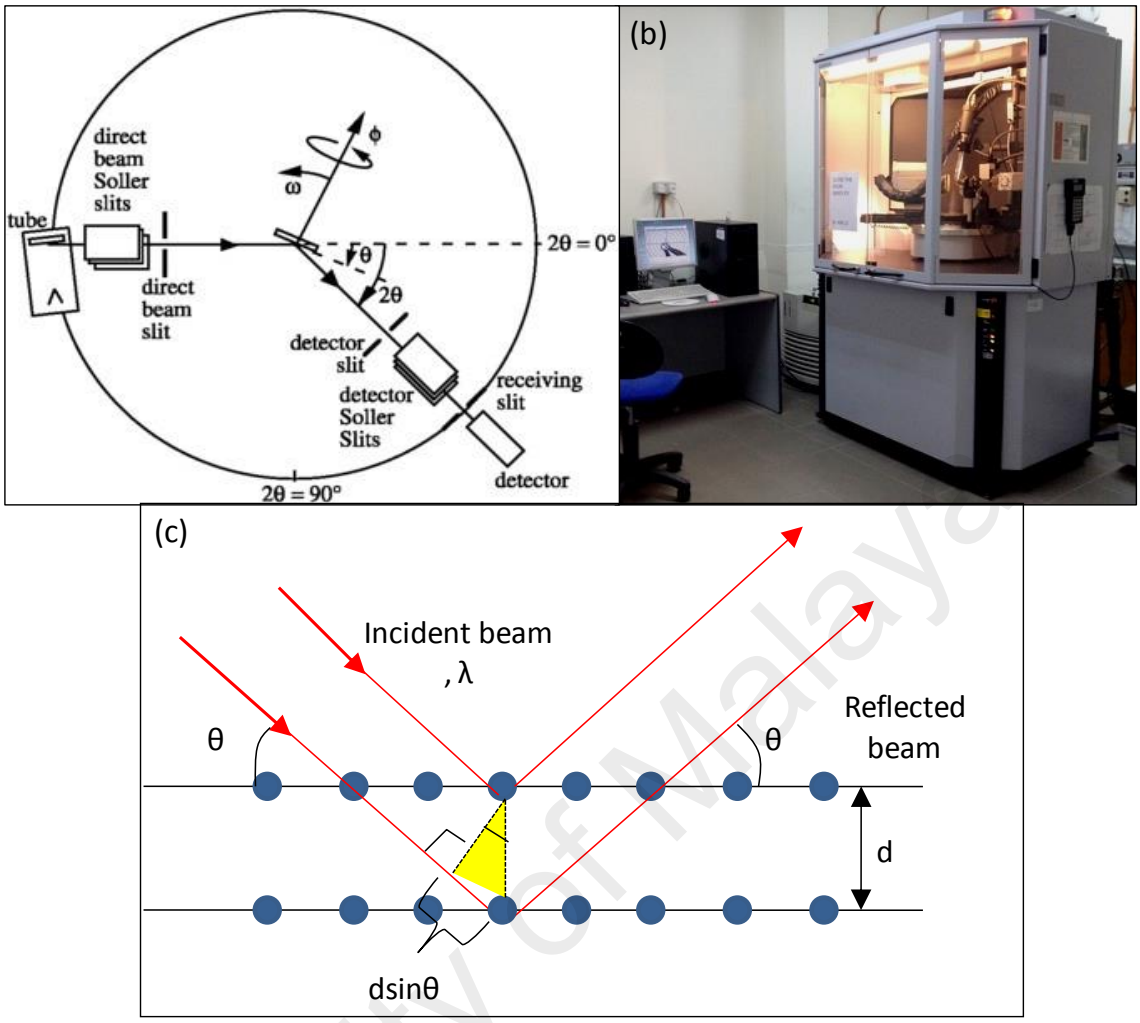

Figure 3.21: (a) Schematic diagram of the X-ray diffractometer. (b) Schematic diagram of Bragg's law. (c) Photograph of PANalytical Empyrean XRD diffrometer. (Fultz & Howe, 2013; Sharma et al., 2012)

University of Malaya

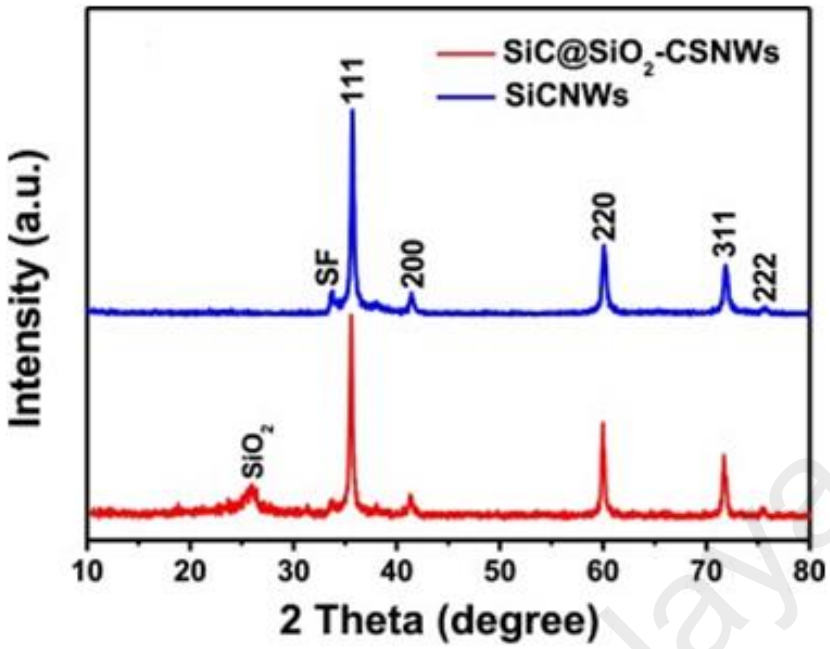

Figure 3.22: XRD spectra of Si nanowires and SiC@SiO_2 core-shell nanowires. (Hu et al., 2016)

3.4.6 X-ray Photoelectron Spectroscopy (XPS)

X-ray Photoelectron Spectroscopy (XPS) also known as Electron Spectroscopy for Chemical Analysis (ESCA) widely used to investigate the chemical composition of surfaces. Both composition and the chemical state of surface constituents can be determined by XPS. This technique is based on the photoelectric effect and was initially developed by Professor Kai Siegbahn at the University of Uppsala in 1970. Before that, in 1887, Heinrich Hertz discovered that electrodes illuminated with ultraviolet light create electric sparks more easily. In 1905 Albert Einstein published a paper that explained experimental data from the photoelectric effects as being result of light energy being carried in discrete quantized packets (Briggs, 1981).

In this research XPS analysis were done at Synchrotron Light Research Institute in Thailand. Figure 3.23(a) shows a schematic diagram of BL3.2a (PES) of the Synchrotron Light Research Institute in Thailand. The PES system is equipped with a Thermo VG Scientific CLAM2 electron spectrometer and operated in the conditions of maximum photon energy 600 eV with an energy step of 0.1 eV. The obtained binding

University of Malaya

energies (BE) were calibrated using the C 1s energy of 284.6 eV attributed to adventitious carbon that normally unavoidably presence in all air-exposed materials. Figure 3.23(b) shows photograph of X-ray photoemission spectroscopy (XPS) at the photoemission spectroscopy (PES) beamline, BL3.2a.

XPS uses the same photoelectron principle to study materials. The basic principle of XPS is schematically shown in Figure 3.23(c). When an X-ray beam directs to the sample surface the interaction between an X-ray photon and the core level electron of an atom causes a complete transfer of the photon energy to the electron. If the photon energy, hν is large enough, the core electron will then escape from the atom and emit out of the surface. The emitted electron with the kinetic energy of E_k is referred to as the photoelectron.

Figure 3.24(a) shows the XPS wide scan of SiC:H films. The scan shows the silicon (Si 2p and Si 2s), carbon (C 1s), and oxygen (O 1s) peaks. The oxygen peak originates due to surface oxidation of films. Figure 3.24(b-d) shows typical narrow scan deconvoluted XPS spectra of the Si (2p), C (1s), and oxygen O (1s) electron state, respectively. The spectrum has been decomposed into several peaks based on the assumption that each peak consists of the Gaussian sum function. The Si (2p) peak (96 eV–106 eV) was deconvoluted into the Si–Si, Si–C, and Si–O peaks. The C (1s) peak (280 eV–292 eV) was deconvoluted into the C–Si, C–C, C–OH, and C=O peaks. The O (1s) peak (530 eV–537 eV) was deconvoluted into O–Si, O–CH, O=C, and O–O peaks.

University of Malaya

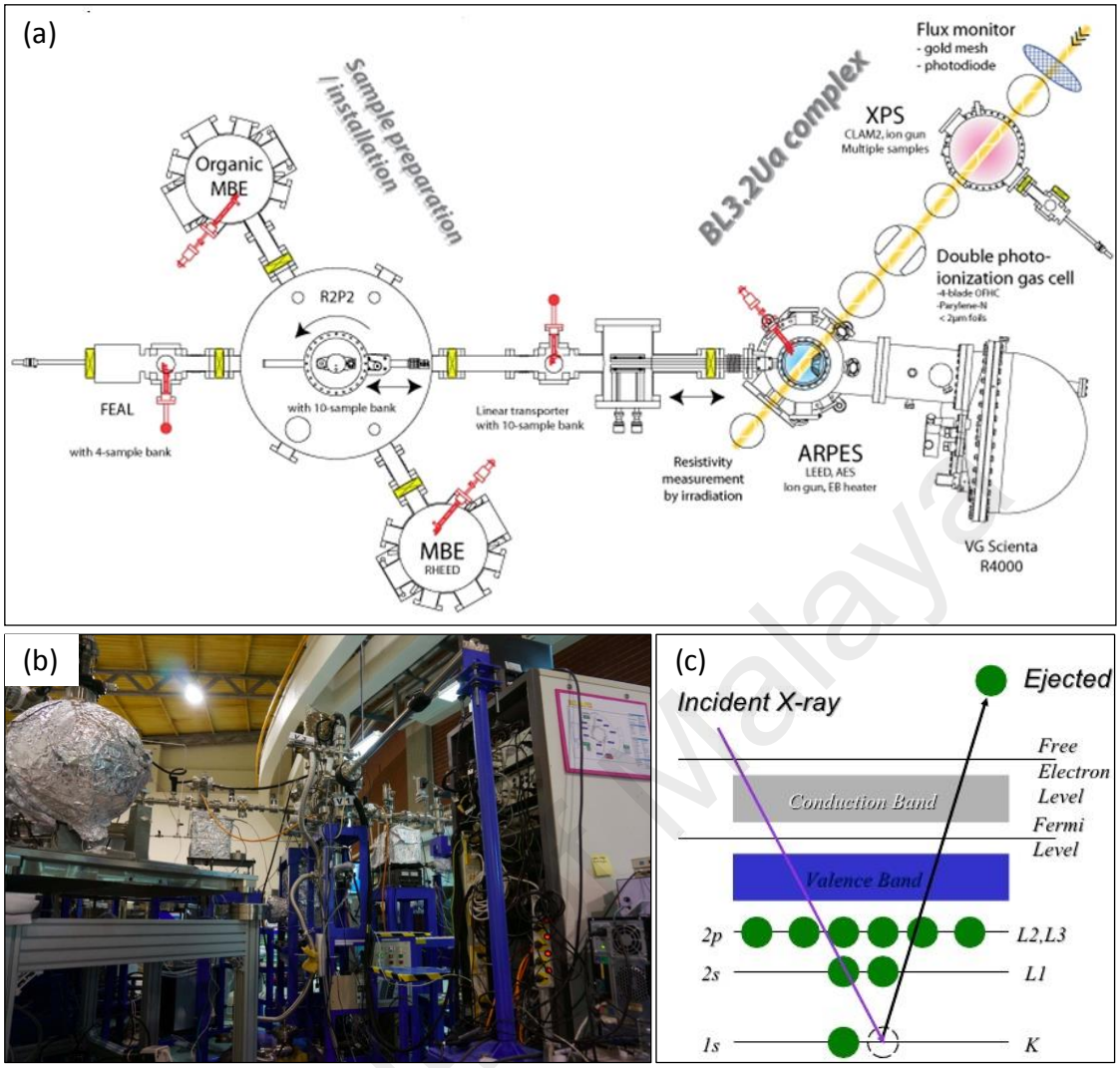

Figure 3.23: (a) A schematic diagram of photoemission spectroscopy. (b) Photograph of X-ray photoemission spectroscopy (XPS) at the photoemission spectroscopy (PES) beamline, BL3.2a, of the Synchrotron Light Research Institute in Thailand. (c) A schematic diagram of BL3.2Ua (PES). (Source: Synchrotron Light Research Institute in Thailand)

University of Malaya

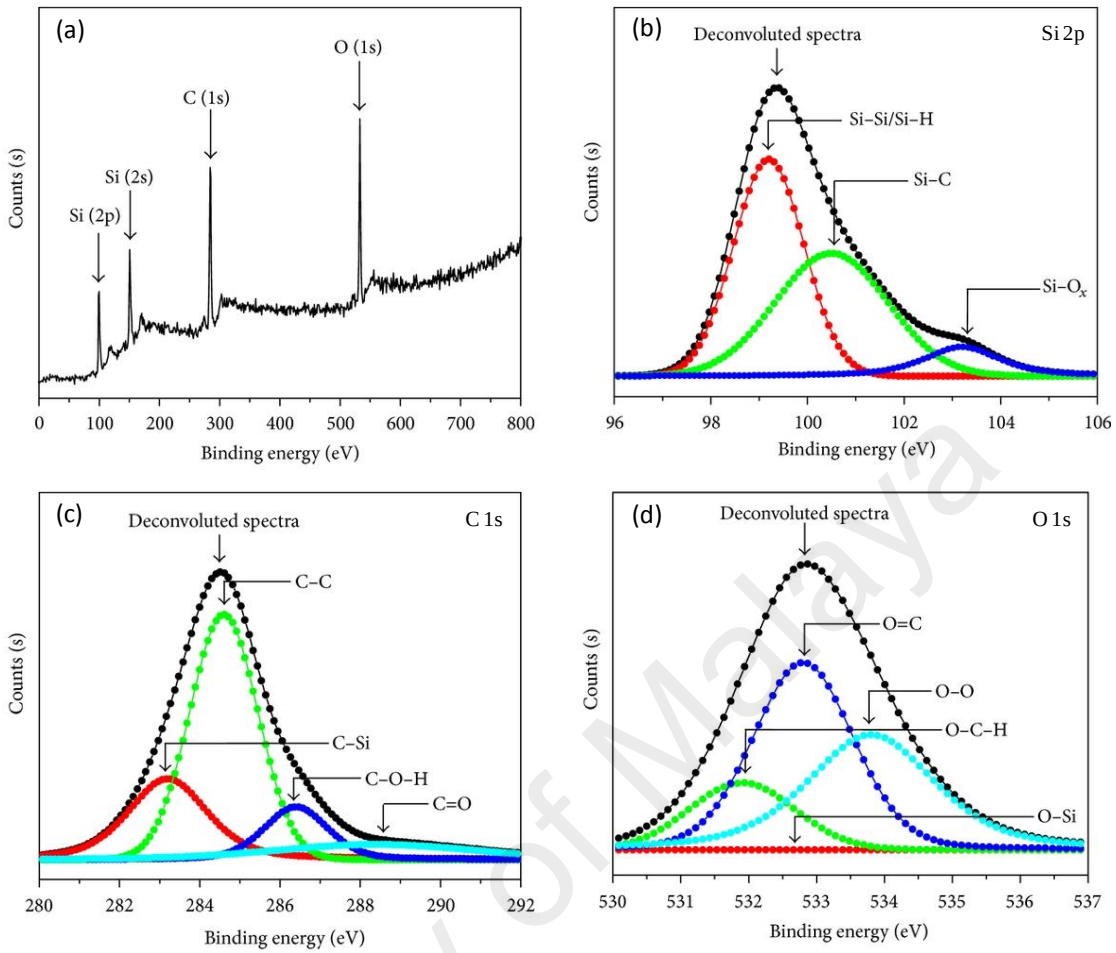

Figure 3.24: Typical XPS spectra for SiC:H film deposited at 350 mTorr by HWCVD method: (a) Wide scan. (b) Deconvoluted XPS spectra of Si (2p) in the range 96 eV–106 eV. (c) Deconvoluted XPS spectra of C (1s) in the range 280 eV–292 eV. (d) Deconvoluted XPS spectra of O (1s) in the range 530 eV–537 eV. (Kamble et al., 2014)

3.4.7 Cyclic Voltammetry

Cyclic voltammetry (CV) is a type of potentiodynamic electrochemical measurement that usually used to deal with any electrochemically active species. It measures the current that arises at the working electrode surface by adjusting the potential in the electrochemical reaction. Czech chemist called Jaroslav-Heyrovsky was first introduced voltammetry in 1922, for which he received the 1959 Nobel Prize in chemistry. The instrument, which monitors current-voltage curves (polarograph), was invented by Heyrovsky and Shikata. The resulting current-voltage plot is called voltamogram where current is displayed in vertical axis and potential in horizontal axis. In 1960's and 1970's, significant advances were made in all areas of voltammetry which include the

University of Malaya

theoretical, methodology and instrumentation. The enhancement of this method facilitated the rapid commercial development of relatively inexpensive instrumentation of this cyclic voltammetry (Farghaly et al., 2014).

Voltammetry is based on voltage-current-time relationship arising in a cell of three electrodes: working electrode (WE), reference electrode (RE), and counter (auxiliary) electrode (CE). They immersed in a solution containing of solution that acts as electrolytes. In this research, CV measurement was performed using computer-controlled VersaSTAT 3 Electrochemical Workstation (Princeton Applied Research, USA). A platinum wire was used as counter electrode and Hg/HgO is used as reference electrode. The platinum wire electrode functions as current carrying electrode while Hg/HgO electrode was used for controlling and measuring potential between the working electrode and electrolyte. All measurements are performed in an electrolyte solution made of 1.0 M KOH. Figure 3.25 show schematic diagram of CV measurement. Figure 3.26(a&b) show photographs of three electrodes and CV measurement set-up.

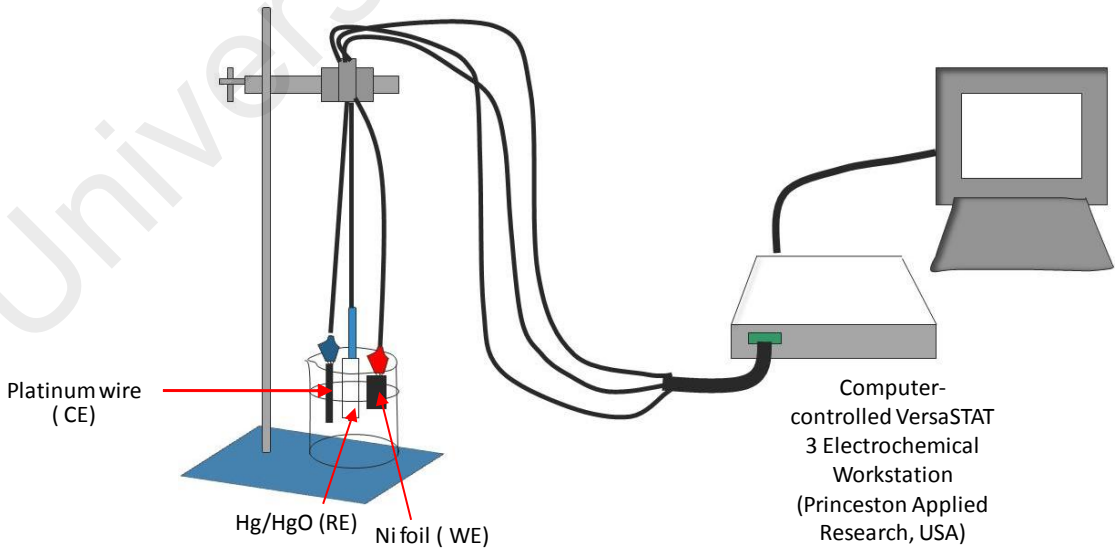

Figure 3.25: Schematic diagram of CV measurement.

University of Malaya

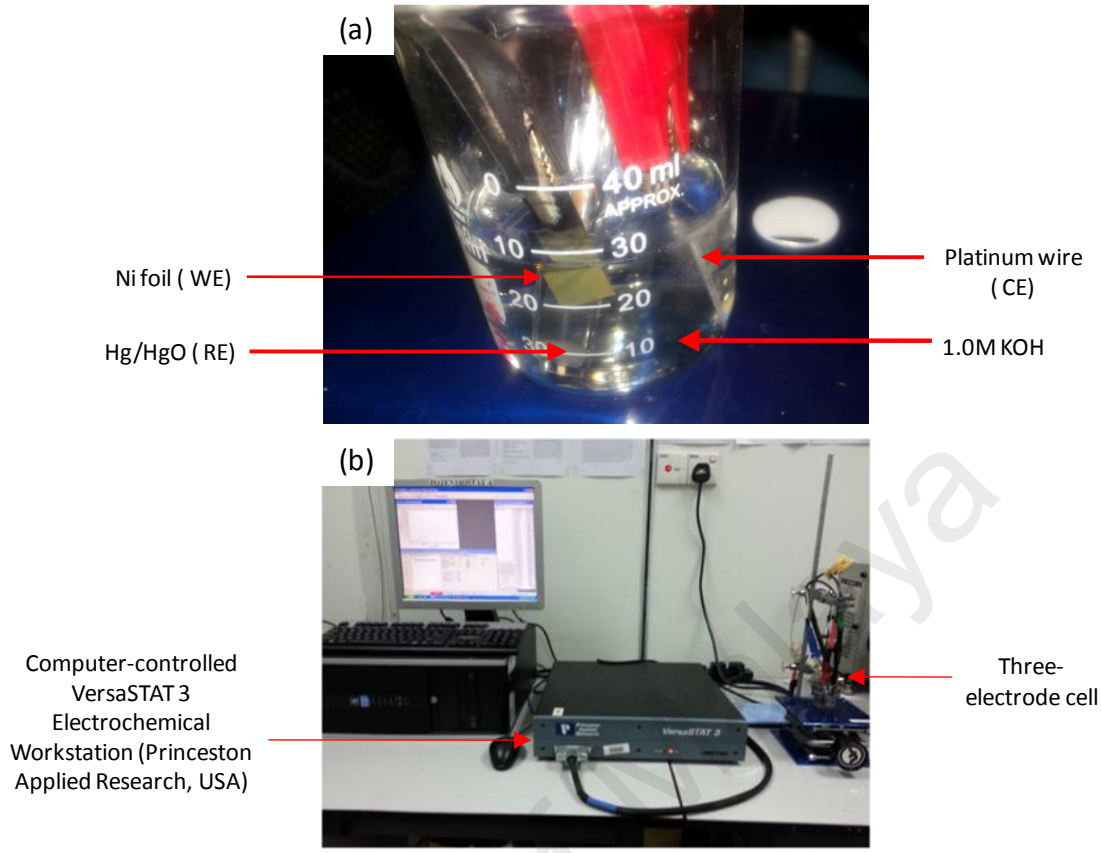

Figure 3.26: (a) Photograph of three electrodes and 1.0 M KOH. (b) Photograph CV measurement set-up.

University of Malaya

CHAPTER 4: RESULTS AND DISCUSSIONS

4.1 Introduction

This chapter discusses the result obtained from the characterization of NiSi/SiC core-shell nanowires prepared by using HWCVD. Two different sets of parameters prepared in this research: (1) Different substrate temperatures (350 to 530°C), and (2) Different CH_4 flow rates (0.5 to 3.5 sccm). For both sets, the pressure, SiH_4 flow rate and rf power were fixed at 3 mbar, 1.0 sccm and 5 W, respectively. The morphology and structural of the nanowires were obtained by using five different characterization instruments such as FESEM, TEM, EDX, Raman, XRD and XPS. The structural properties of the nanowires were determined from Raman and XRD spectra while FESEM and TEM were used to study the morphological and microstructure of the nanowires. For the elemental analysis, EDX characterization was used to identify the elemental composition of nanowire. On the other hand, the compositions of nanowires were further revealed by XPS results.

The growth mechanisms of nanowires also were investigated for both parameters in order to understand the morphological and structural properties changes of these nanostructures. Finally, the CV measurement was carried out to study the supercapacitor performance of the nanowires.

4.2 Effect of substrate temperatures on the growth, structural and electrochemical properties of the NiSi/SiC core-shell nanowires

4.2.1 The morphological and structural properties of the NiSi/SiC core-shell nanowires

Figure 4.1(a-e) shows the FESEM images of the samples prepared by HWCVD at different substrates temperature. The sample prepared at 350°C (Figure 4.1(a)) clearly illustrated that no formation of nanowires and have only appearance of spherical grains that were uniformly distributed on the substrate surface. Some grains started to grow as

University of Malaya

short pillars since the temperature were not sufficient to active the reaction of Ni and Si thus limited the formation of NiSi nanoparticles via diffusion - controlled process (Yu et al., 2013). The estimated average size of these nanoparticles was about 68 nm. According to Lavoie et al. (2013), the formation of NiSi started at temperature above 350°C via a nickel film and Si substrate reaction process. The high density of nanowires started to grow and be randomly distributed on the substrate surface as temperature increased to 400°C. Some of the NiSi grains also be observed on the substrate surface as shown in Figure 4.1(b). The formation of these nanowires could be due to the moderate diffusion rate of Si into Ni nanoparticles thus forming sufficient amounts of NiSi solid particles.

An increased in substrate temperature results in a higher surface diffusion rate, leading to enhancement of the nanowire's growth rate (LaLonde et al., 2011). As shown in Figure 4.1(c), at substrate temperature of 450°C, a high diffusion rate of the Si into Ni nanoparticles enhances the development of smaller solid NiSi particles contributes to the formation of a high density of vertically aligned nanowires. Furthermore, the surface of the nanowires shows a relatively smoother than nanowires at substrate temperature of 400°C. The surface roughness of the nanowires grown at 400°C and 450°C can be clearly observed in the insets. However, as substrate temperature increased up to 530°C (Figure 4.1(e)), the density of nanowires showed significantly decreases. High substrate temperatures led to an increasing surface mobility of the growth species. These species therefore sufficiently reach growth sites for forming larger NiSi solid particles or layers instead of precipitation as nanowires (Kim, 2012).

The variation of average diameters and lengths of the nanowires at different substrate temperatures were clearly be shown in Figure 4.2. The estimated average diameters of the nanowires grown at 400°C and 450°C were about 0.12 μm and 0.09 μm

University of Malaya

respectively, while the estimated average lengths were about 1.36 μm and 2.12 μm, respectively. The change in diameters could be due to an increase in the nucleation sites for precipitating the smaller NiSi solid nanoparticles thus allowing for the growth of smaller and longer nanowires. As reported by Kim (2012), higher growth temperature will reduced the volume of free energy resulting in an enhancement of the total free energy. This induced the growth of smaller nucleation sites which subsequently increased the growth rate of the nanowires. The diameter of the nanowires was noticeably enlarged with the increase in the substrate temperature while the lengths of nanowires decreased. The estimated average diameters of nanowires grown at 500°C and 530°C were about 0.14 μm and 0.19 μm, respectively, while the estimated average lengths were about 2.65 μm and 2.48 μm. The change of the diameter of the nanowires was also related to the increase in the surface mobility of the growth species which was similar to several reported works previously (Chen et al., 2002; Yang et al., 2007).

University of Malaya

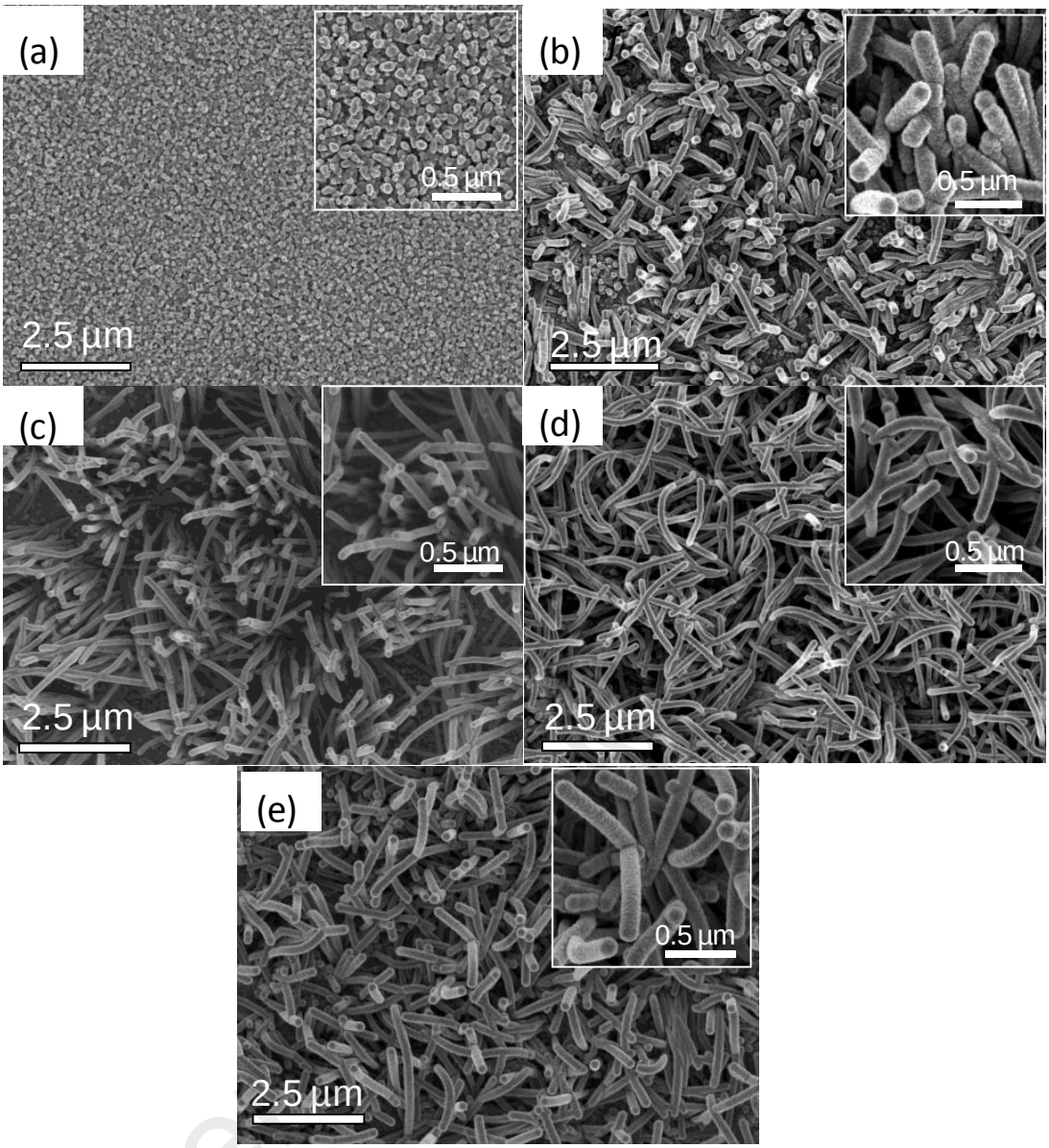

Figure 4.1: FESEM images of NiSi/SiC core-shell nanowires at different substrates temperatures (a) 350°C (b) 400°C (c) 450°C (d) 500°C (e) 530°C.

Unive

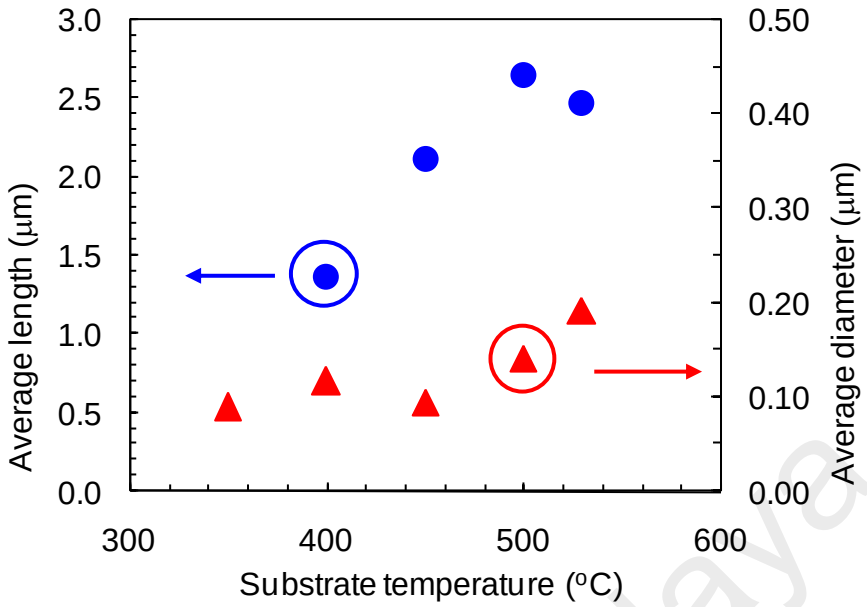

Figure 4.2: Variation of average lengths and diameters of nanowires.

Figure 4.3(a) shows the deposition rate of the nanowires at different substrate temperature. As temperature increased, the deposition rate of the nanowires increased from 0 to 88. 43Å/s at 500°C and decreased to 82.57 Å/s as temperature increased to 530°C. The deposition rate constant R is known to be a function of substrate temperature T, and can be expressed by the Arrhenius equation:

$$R = R_0 e^{-\frac{E_a}{k_B T}} \qquad (4.1)$$

where E_a is the activation energy, and R_o and k are the rate constant and the Boltzmann constant, respectively (Cheng & Chen, 2012). The activation energy for the growth of NiSi/SiC core-shell nanowires on Si substrates can therefore be determined by an Arrhenius plot of the ln (rate constant), lnR, versus the reciprocal of substrate temperature (1/T), as shown in Figure 4.3(b). The activation energy derived from the slope of the line is about 227.76 ±5 meV which is much lower than activation of 3C-SiC nanowires and SiC nanowires coated with carbon fiber at 290 and 1762 meV (Cheng et al., 2017; Prakash et al., 2014). Such lower in E_a could be due to presence of Ni as catalyst during deposition process.

University of Malaya

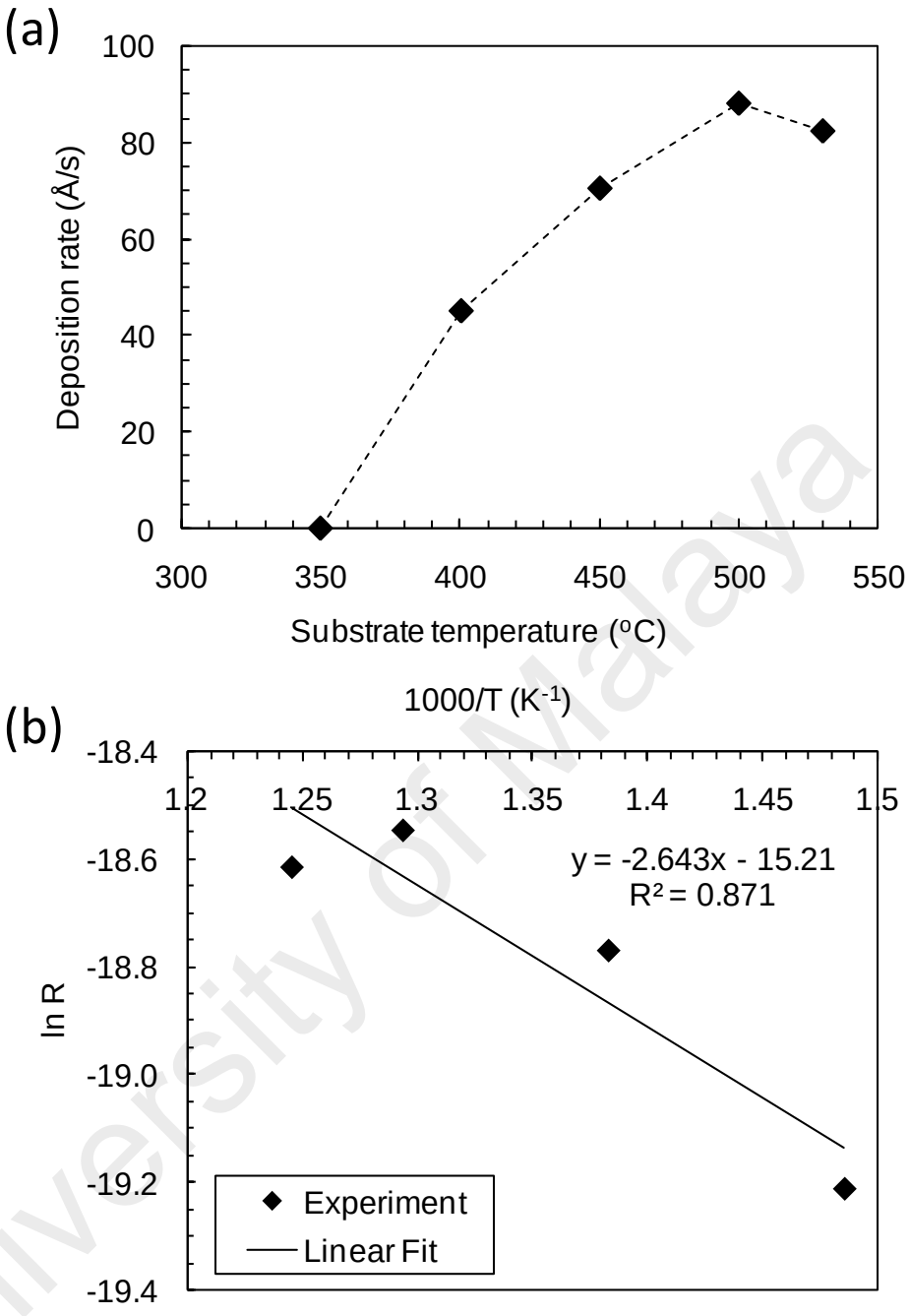

Figure 4.3: Deposition rates at different substrate temperatures (b) Arrhenius plot of lnR versus the inverse substrate temperature (1/T).

University of Malaya

The FESEM images of the samples prepared at substrate temperature of 400°C with respective EDX spectra are presented in Figure 4.4 while the elemental compositions of the samples are tabulated in Table 4.1. The labels of S1 and S2 represent the point scan on the tip and stem of nanowires, respectively. The EDX spectra for the scans at S1 and S2 are presented in Figures 4.4(b&c), respectively. These spectra clearly illustrate that the tip of the nanowire consist of Si (35.31 at. %), O (34.61 at. %), Ni (24.86 at. %), and O (5.21 at. %) while stem of the nanowire contains of Si (39.72 at. %), C (24.31 at. %), Ni (30.27 at. %), and O (4.97 at. %). As shown in Table 4.1, amount of atomic concentration of Ni and Si at stem of nanowire are higher than at tip of nanowire. This result proved that formation of nanowire grows up from NiSi solid catalyst alloys. On the other hand, a relatively low amount of O in the stem of nanowire as compared to the tip of the nanowire indicates that the formation of SiO_x could be due to oxidation after the nanowires were exposed to the atmospheric ambient.

Based on the Table 4.1, the Ni to Si ratio at the tip and the stem of the nanowire can be calculated. The amounts of Ni to Si ratio are estimated about 0.70 and 0.76, respectively. These values are comparatively close to the NiSi phase with a Ni-to-Si ratio of about 1. Hence, this composition ratio suggests that growth of the nanowires was followed by a diffusion control growth (Kim et al., 2005; Kim et al., 2006).

University of Malaya

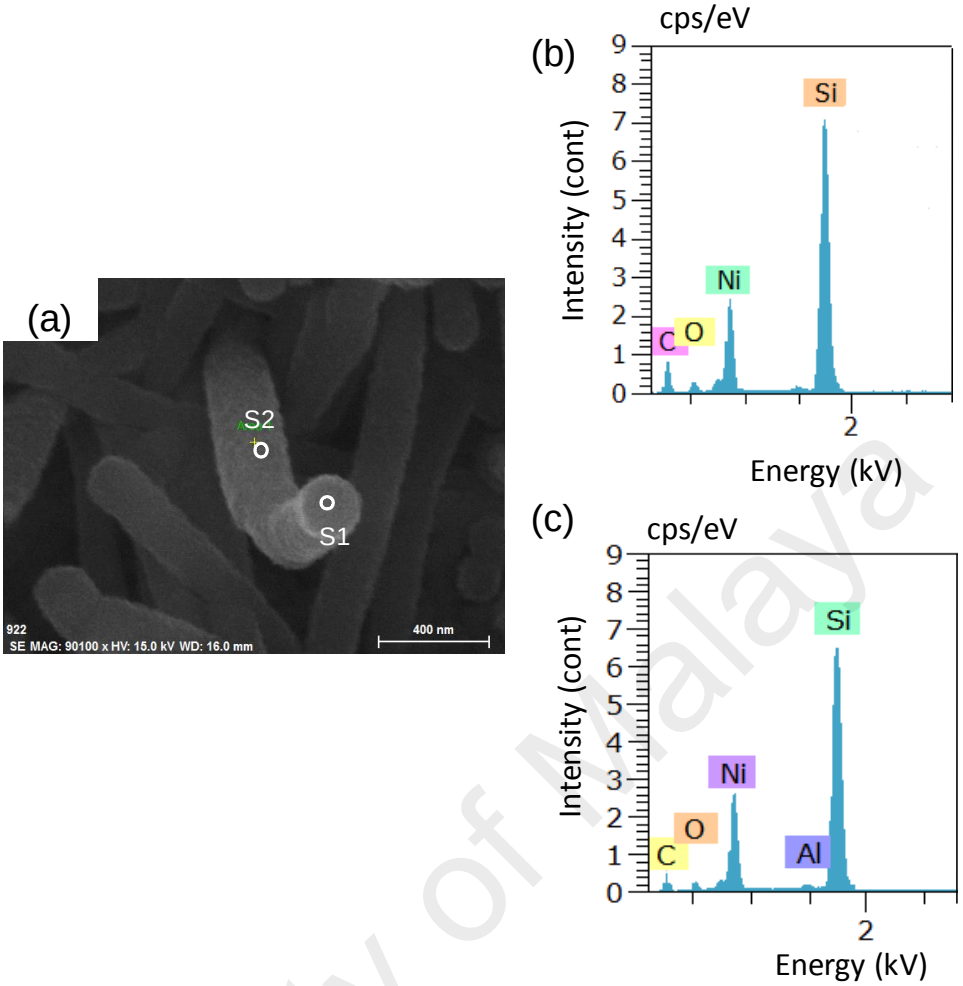

Figure 4.4: (a) FESEM images of single nanowire prepared at substrate temperature of 400°C. (b&c) EDX spectrum collected at the tip and stem of nanowire which are labeled by S1 and S2 respectively, as shown in (a).

Table 4.1: Element content at 400°C at tip and stem of the NiSi/SiC core-shell nanowire.

		Percentage of composition (at. %)			
Temperature (°C)	**Position**	**Si**	**C**	**Ni**	**O**
400	Tip	35.31	34.61	24.86	5.21
	Stem	39.72	24.31	30.27	4.97

University of Malaya

The composition of the nanowire was further investigated by using STEM/EDX elemental mappings using HAADF detector in the TEM, as illustrated in Figure 4.5. Figure 4.5(a) shows a typical dark-field STEM image of a single nanowire on a carbon film supported by a TEM copper-grid clearly reveals that the nanowire consisted of a core-shell structure with the dotted box indicating the scan area for EDX elemental mappings. The EDX elemental maps of the nanowire for Ni, Si, C, and O are demonstrated in Figure 4.5(b-e) respectively. This EDX elemental mapping supported EDX spectrum shown in Figure 4.4.

The presence of Ni with a company of Si content along the center axis of the nanowire which shown in Figure 4.5(d) support a NiSi core of the nanowire. High densities of Si and C as presented in Figure 4.5(b&c) reveal uniform distributions of Si and C in the shell of the nanowire. Furthermore, the uniform distribution of O as illustrated in the O map (Figure 4.5(e)) supports the formation of a SiO_x thin layer on the surface of the nanowires. The formation of SiO_x could be due to oxidation after the nanowires were exposed to the atmospheric ambient.

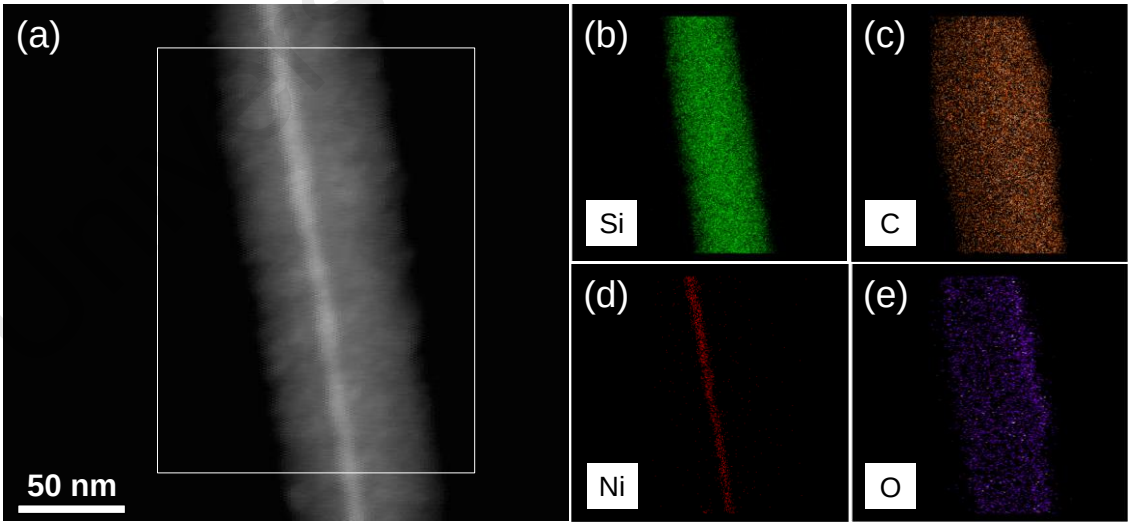

Figure 4.5: (a) Dark-field STEM image of NiSi/SiC core-shell nanowire prepared by HWCVD at substrate temperature of 450°C. (b-e) EDS element maps of the core-shell nanowire.

University of Malaya

The microstructure of NiSi/SiC core-shell nanowires was investigated by TEM and HRTEM images as shown in Figure 4.6. These nanowires were prepared on top of a carbon film supported by a TEM copper-grid as demonstrated in the TEM image. The TEM image of many nanowires gathered together shown in Figure 4.6(a). Some of the nanowires shows formation of bumps along their lengths indicated the formation of out-diffusion NiSi core. Figure 4.6(b) clearly illustrated the core and shell structure of the nanowire with their diameter being approximately about 13 nm and 98 nm, respectively. These diameters were consistent along the length of the nanowire indicating that they have been grown without tapered morphology attributed to the radial growth which generally occurred in the CVD deposition (Joyce et al., 2007). The HRTEM image near the edge of the core reveals a single-crystalline structure surrounded mainly by amorphous shell as clearly depicted in Figure 4.6(c). The estimated lattice spacing of the crystalline core was approximately 0.20 nm, corresponding to a crystallographic plane of NiSi (111) orientation [JCPDS card No. 65-1507].

This single crystalline NiSi structure was further revealed by a Fast Fourier Transform (FFT) image, as shown in the inset. Figure 4.6(d) shows a HRTEM image obtained at the sidewall of the shell clearly revealing polycrystalline structure of nanocolumns. The estimated lattice spacing of about 0.25 nm corresponds to 3C-SiC (111) orientation [JCPDS card No. 29-1129]. The crystalline plane of 3C-SiC (111) was further revealed by the FFT image as shown in the inset. These nanocolumns were formed by the 3C-SiC nano-crystallites embedded within an amorphous matrix and the columnar structure acts as a shell of the nanowires.

University of Malaya

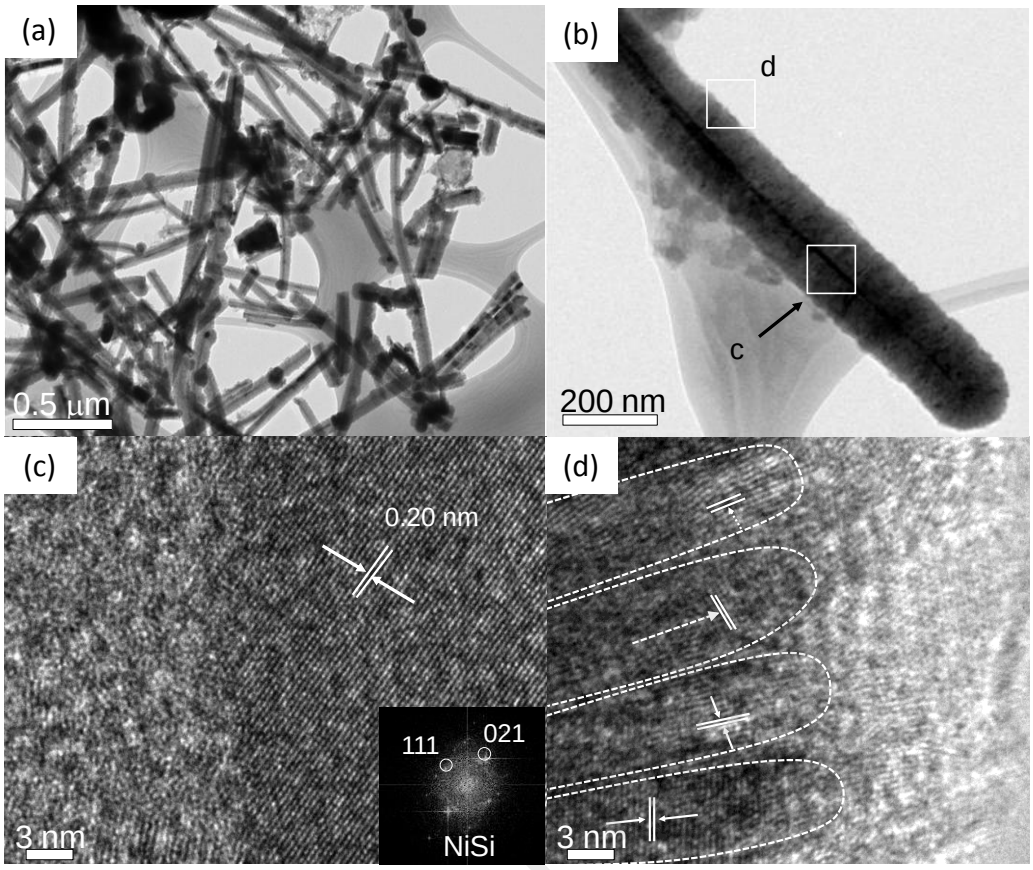

Figure 4.6: (a) TEM image of the typical NiSi/SiC core-shell nanowires grown by HWCVD. (b) Magnified image of single NiSi/SiC core-shell nanowire. (c&d) HRTEM images of core and shell nanowire. Inset represent FFT image of the core and shell nanowire.

The Raman scattering spectra of the nanowires prepared at different substrate temperatures of 350°C until 530°C are shown in Figure 4.7. In the spectra, the appearance of sharp crystalline NiSi excitation bands at 193 cm^{-1} and 210 cm^{-1} were clearly observed for the sample at substrate temperature of 350°C till 527°C indicating the formation of the NiSi core in the nanowires (Wang et al., 2007; Zhao et al., 2004). Moreover, the spectra also presented two broad Raman excitation bands at ~770-780 cm^{-1} and ~893-902 cm^{-1} corresponding to transverse optical (TO) and longitudinal optical (LO) of SiC, respectively. This implies the formation of SiC shell of the nanowires.

University of

According to Bechelany et al. (2007), the transverse optical (TO) and longitudinal optical (LO) mode of bulk β-SiC located at 796 cm^{-1} and 976 cm^{-1}. However, as shown in Table 4.2, this Raman peak is red-shifted as substrate temperature increased from 350°C to 530°C. The shifted of these Raman excitation bands relative to the bulk 3C-SiC crystal could be due to presence of SiC nano-crystallites embedded within an amorphous matrix. In addition, the asymmetric broadening of the Raman peaks of crystalline SiC for TO and LO modes is observed as temperature increased from 450°C to 530°C for LO modes and 350°C to 500°C.

The full width at half maximum (FWHM) of the TO and LO modes of crystalline SiC increased from 64.43 cm^{-1} to 94.26 cm^{-1} for TO mode and 82.26 cm^{-1} to 90.15 cm^{-1} for LO mode. The increased FWHM for both modes indicates a formation of SiC nano-crystallites embedded within an amorphous matrix in the shell as reported previously (Panda et al., 2010). In addition, as reported by other researchers, the shifted of Raman peak can be due to the lattice thermal expansion. Heating of the lattice will caused the volumetric expansion of the lattice. This will result the restoring force of lattice vibration to decrease. The change in interatomic force modifies the phonon vibrational frequency that eventually caused the phonon peak shifting toward lower frequency (Calizo et al., 2007; Xiao-Yong et al., 2012).

University of Malaya

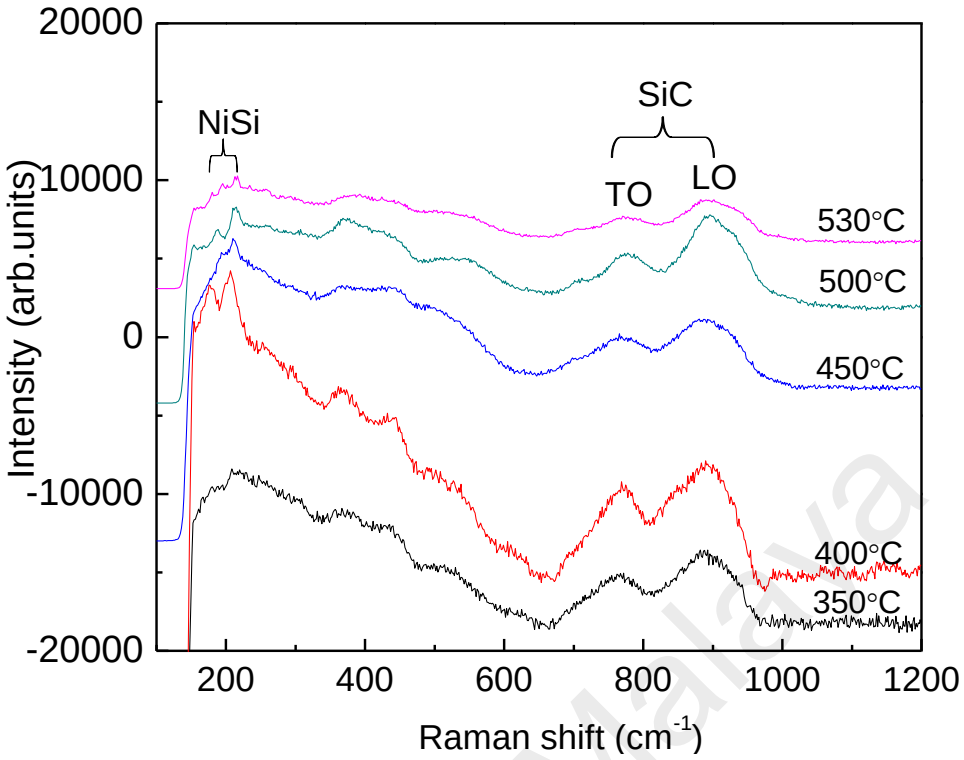

Figure 4.7: Raman spectrum for NiSi/SiC core-shell nanowires prepared at different substrate temperatures.

Table 4.2: Raman shift and FWHM of NiSi/SiC core-shell nanowires.

Substrate temperatures (°C)	TO		LO	
	Raman shift (cm^{-1})	FWHM	Raman shift (cm^{-1})	FWHM
350	766.94	96.24	893.30	82.26
400	768.92	98.84	894.26	88.06
450	778.37	64.43	898.54	90.15
500	770.53	78.75	895.08	97.99
530	769.48	94.26	901.77	90.97

Figure 4.8 shows the XRD pattern of the core-shell nanowires prepared at different substrate temperatures. At substrate temperature of 350°C, only Ni_2Si phase presented. The appearance of Ni_2Si phase located at 46.04°, 47.84° and 68.4° belong to (102), (110), and (202) crystalline planes according to JCPDS card No.03-1069. As substrate temperature increased up to 400°C, the NiSi phase started to appear. The $NiSi_2$ phase located at 44.3°, 45.6° and 56.2° belong to (210), (112) and (013) according to JCPDS

University of Malaya

card No. 65-1475. Furthermore, there was an appearance of a small diffraction peak at 28.4^0 which could be attributed to crystalline Si plane of (111) orientation [JCPDS card No. 27-1402]. The appearance of crystalline Si peak was also been observed at temperature of 450°C and 500°C. The crystalline Si peak could be from the deposited layer at the bottom of the nanowires due to the high penetration depth of the X-ray source.

At substrate temperature of 450°C, it clearly observed the presence of dominant peak at 47.3° indicates a presence crystalline NiSi plane with orientation of (121) [JCPDS card No. 65-1475]. However, the crystalline plane (121) does not match with crystalline plane of NiSi core in the HRTEM image (shown in Figure 4.6(c)). This is because as observed crystalline planes of NiSi core in the HRTEM image does not reflected the overall crystalline planes of the NiSi owing to the high resolution imaging on a selected nanowire. The NiSi crystalline peak was accompanied by a small peak at 51.8° which is corresponds to crystalline NiSi plane of (310) orientation. At substrate temperature of 500°C, only NiSi phase located at 47.3° observed in the pattern. As substrate temperature increased to 530°C, only the Ni_3Si_2, phases located at 28.04°, 44.42°, and 46.16° belong to (112), (600) and (242) according to JCCPDS card No.17-1881 observed in the pattern implying the formation of stabilized Ni_3Si_2 films at the base of the nanowires.

Furthermore, as shown in the inset figure, a SiC peak started to appear at 35.7° belonging to the (111) crystalline plane of 3C-SiC according to the JCPDS card No.29-1129. The SiC peak increased in intensity for the nanowires prepared at higher substrate temperatures of 400°C, 450°C and 530°C. By using Scherrer's equation, the crystallites size of the SiC nanocolumns can be estimated from the relation of $D = k\lambda/\beta \cos \theta$, where k, λ, β, and θ are the Scherrer's constant, the wavelength of X-ray (1.5402 Å), the full-width at half-maximum (FWHM), and the Bragg angle of the diffraction peak

University of Malaya

respectively (Goh et al., 2012). The estimated crystalline sizes for samples prepared at substrate temperatures of 400°C, 450°C, 500°C and 530°C are approximately ± 4.12 nm, 4.11 nm, 4.19 nm and 7.50 nm, respectively. An increase in substrate temperatures enhances surface mobility thus leading to an increase in the diffusion of C into the NiSi solid particles and forming a bigger SiC layer at higher temperature. This results in an increase in the formation of bigger SiC nanocolumns as estimated from the diffraction peak width by Scherrer's relation.

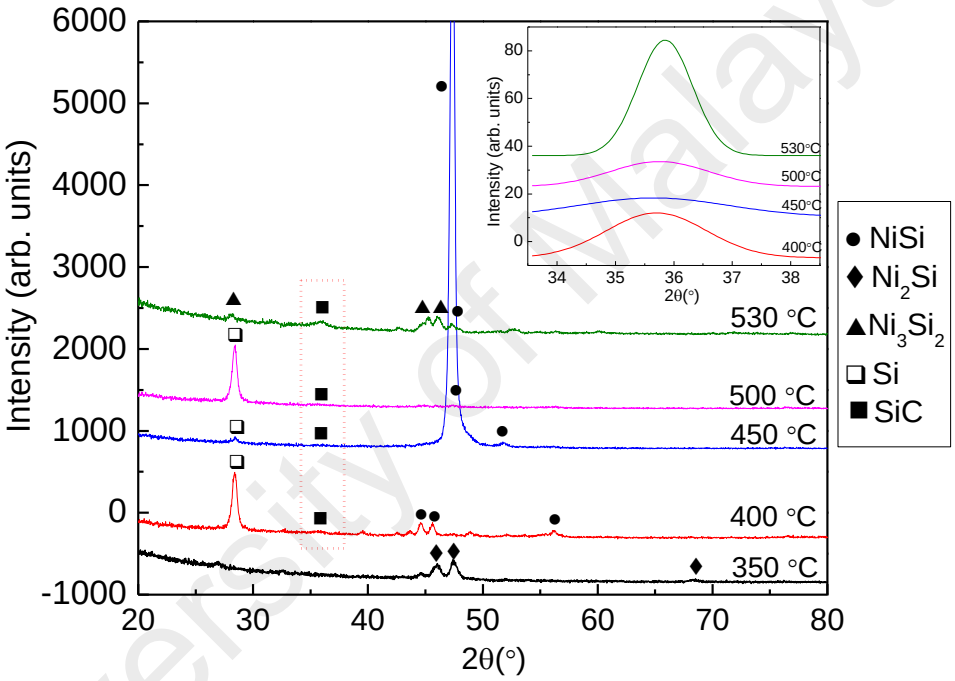

Figure 4.8: XRD pattern of the NiSi/SiC core-shell nanowires grown by HWCVD at different substrate temperatures.

The chemical bonding states of NiSi/SiC core-shell nanowires were investigated by using x-ray photoelectron spectroscopy (XPS) analysis. Figure 4.9(a) shows the XPS wide scan of NiSi/SiC core-shell nanowires at substrate temperature of 450°C. The scan shows the main compositions are silicon (Si 2p and Si 2s), carbon (C 1s) and oxygen (O 1s). Figures 4.9(b-d) show typical narrow scan deconvoluted XPS spectra of the Si 2p, C 1s, and O 1s electron state, respectively. The deconvolution of Si 2p band as shown in Figure 4.9(b) revealed that the band consists of four major components at 98.5 eV,

University of Malaya

99.5 eV, 100.7 eV and 102.7 eV correspond to Si-Si (17.97%), Si-Ni (28.53%), Si-C (44.67%) and Si-O_x (8.83%) chemical states respectively.

The larger percentages of Si-C (44.67%) and Si-Ni (28.53%) chemical states in the spectrum imply the formation of SiC shell and NiSi core in the nanowires. Figure 4.9(c) shows the deconvolution of the C 1s band into four chemical states of C-Si (17.32%), C=C (36.45%), C-C (46.05%) and O-C=O (0.17%) at 283.2 eV, 284.4 eV, 285.9 eV and 288.8 eV, respectively. The presence of C-Si chemical state supports the chemical composition of the SiC shell. In addition, the appearance of C=C and C-C chemical states could indicates a diffusion of C onto the NiSi catalyst alloys during the nucleation for forming SiC clusters. Figure 4.9(d) shows the deconvolution of the O 1s band. The spectrum can be decomposed to three Gaussian components located at 531.2 eV, 532.6 eV and 533.8 eV. These three O states are attributed to O=C (6.54%), O=Si (48.55%) and O-O (44.91%) (Tseng et al., 2013). The O=Si and oxide related bands are attributed to the formation of SiO_x layer on the surface of the nanowires due to the oxidation after the nanowires were exposed to the atmospheric ambient.

University of Malaya

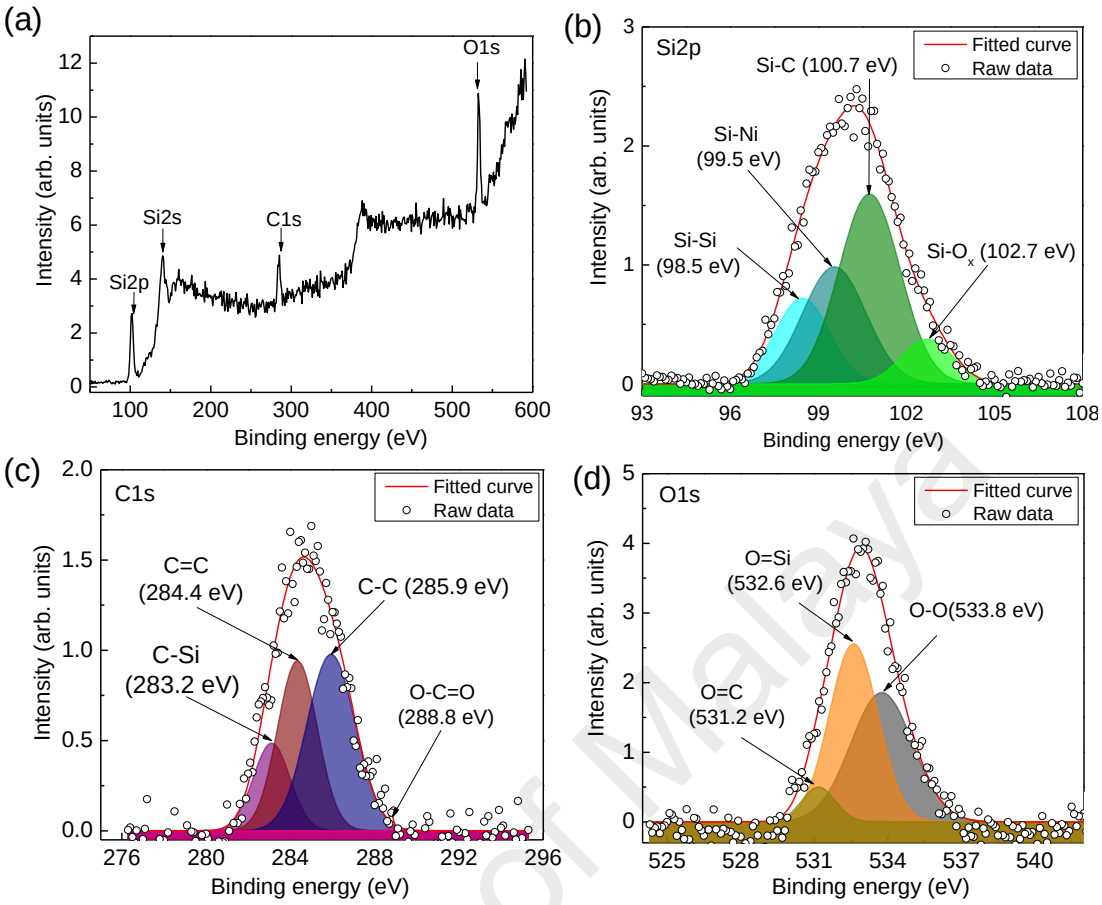

Figure 4.9: (a) Wide scan XPS spectra of NiSi/SiC core-shell nanowires at substrate temperature of 450°C. (b) Deconvoluted XPS spectra of Si 2p. (c) Deconvoluted XPS spectra of C 1s. (d) Devonvoluted XPS spectra of O 1s.

4.2.2 The growth mechanism of the NiSi/SiC core-shell nanowires

In order to investigate the growth mechanism of these NiSi/SiC core-shell nanowires, an elemental analysis of EDX points scan on the nanowire and deposited layer is performed as shown in Figure 4.10. The labels S1 to S4 in Figure 4.10(a) represent the points scan on the stem of the nanowire, the deposited layer below the nanowires, the deposited layer with no nanowires on top, and the Si substrate, respectively. The deposited layer below the nanowires and no nanowires on top refer to the smooth particle-like and the grainy structures respectively. The EDX spectra of the stem of the nanowire and the deposited layer below the nanowires are demonstrated in Figure 4.10(b) and (c), respectively.

University of Malaya

The elemental compositions of the points scan for S1 to S4 are tabulated in Table 4.3. The results of the EDX spectra and the quantitative analysis reveal that the nanowire consists of C, O, Ni, and Si, while the deposited layer below the nanowires mainly contain Ni and Si with small amounts of C and O. This implies that the smooth particle-like structure was formed by NiSi solid catalyst particles during the nucleation at the initial growth of the nanowire. The presence of lower amount of C and O contents in the initial growth of the nanowires were from the environment and oxide contamination respectively. The Ni to Si ratio (1.07) is near to 1 indicating the formation of a NiSi solid catalyst for sustaining the epitaxial growth of the NiSi nanowires instead of forming a stable $NiSi_2$ phase in the growth temperature as reported (Zhao et al., 2004). The presence of 7.3% C indicates a diffusion of C into the NiSi solid catalyst particles during the impinging of C-rich species on the NiSi particle surface and form a SiC layer radially on the particle.

The deposited layer with no nanowires on top presents a slightly higher Ni to Si ratio of 1.2, however, it showed about 2% and 4% of C and O respectively, comparatively higher than the deposited layer below the nanowires. This could be attributed to the formation of agglomerated SiC grains which usually have a higher percentage of O content. The EDX spot on the c-Si substrate below the NiSi solid particle is used as a control analysis and is mainly Si (93.5%) with a small amount of Ni (6.5%) indicating a slight diffusion of Ni into the substrate. Hydrogen plasma treatment at the high substrate temperature of 450°C could remove oxide contamination on the Ni layer on c-Si substrate. This could therefore form Ni nanoparticles with less oxide contaminations, and subsequently leads to the base and its surrounded area with higher oxides contaminations. Removing of oxide contaminations by an energetic atomic H during hydrogen plasma treatment has been reported widely (Bai et al., 2005; Cavallotti et al., 2004).

University of Malaya

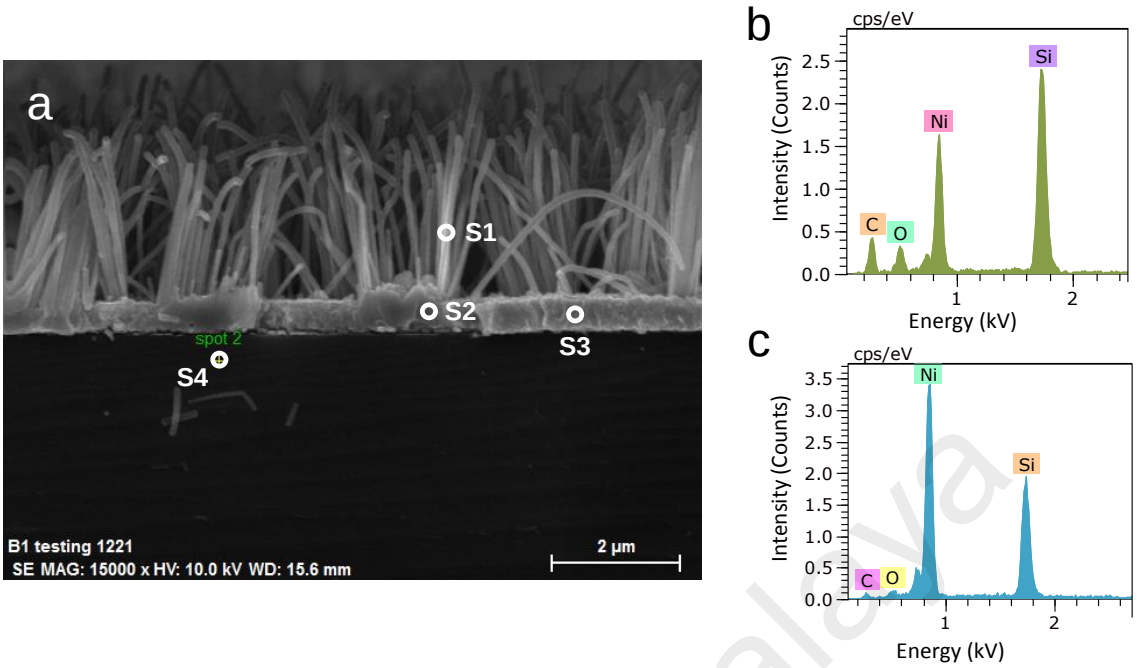

Figure 4.10: (a) FESEM image of the nanowires prepared by HWCVD for EDX elemental analysis. (b&c) EDX spectra obtained on the stem of nanowire (S1) and the deposited layer with nanowires (S2), respectively.

Table 4.3: EDX element contents at different spots for the nanowire sample as shown in Figure 4.10.

EDX scan area	Percentage of composition (at. %)			
	C	Si	Ni	O
Spot on the stem of the nanowire (S1)	43.52	31.21	13.54	11.73
Spot on the deposited layer below nanowires (S2)	7.28	43.89	47.29	1.54
Spot on the deposited layer with no nanowires on top (S3)	8.71	39.67	46.11	5.51
Si Substrate (S4)	0	93.52	6.48	0

University of Malaya

Figure 4.11 shows the AES elemental depth profiles of the nanowires prepared by HWCVD. These elemental profiles are divided into three regions as illustrated in the figure. The elements of the nanowires are mainly consisted of C, O, Ni, and Si. The presence of these elements also supported by EDX elemental analysis as shown in Figure 4.10. In the region A which is on the tip of the nanowires, the C and Si contents are highs with a low O content. This observation agrees well with the formation of SiC shell of the nanowires. On the other hand, the variations of the Si and C contents with etching time in region A support the growth of the SiC as a shell that was grown radially with the NiSi core nanowires simultaneously. The atomic concentration of O is found low and decreases gradually with increase in etching time again reveals that the formation of SiO_x layer on the surface of the nanowires is attributed to the oxidation after being exposed to the ambient condition.

In the region B, the Ni content showed dominant in this region and it reached to a maximum at approximately 1000 s. The C and Si contents decrease with increase in etching time in the same region. The elemental profiles in region B are similar with the areas of S2 and S3 as illustrated in Figure 4.10 that is supported by the elemental compositions of S2 and S3 in Table 4.3. These observations could be used to deduce that the region B is actually indicates the elemental profiles of the root of the nanowires and the NiSi deposited layer. Furthermore, decreasing of C in the region B clearly indicated the diffusion of C into the NiSi region. This strongly supports the nucleation of SiC and this SiC mediates as a shell of the nanowires followed the NiSi core nanowires. The compositions in the region C are same as the area S4 in Figure 4.10. This indicates that the region C is actually in the Si substrate showing a large Si content with a very little Ni content and the Ni content diminish after 2000 s of etching time. Presence of Ni in the Si substrate indicates a Ni diffusion into the substrate since Ni is a fast diffuser in Si.

University of Malaya

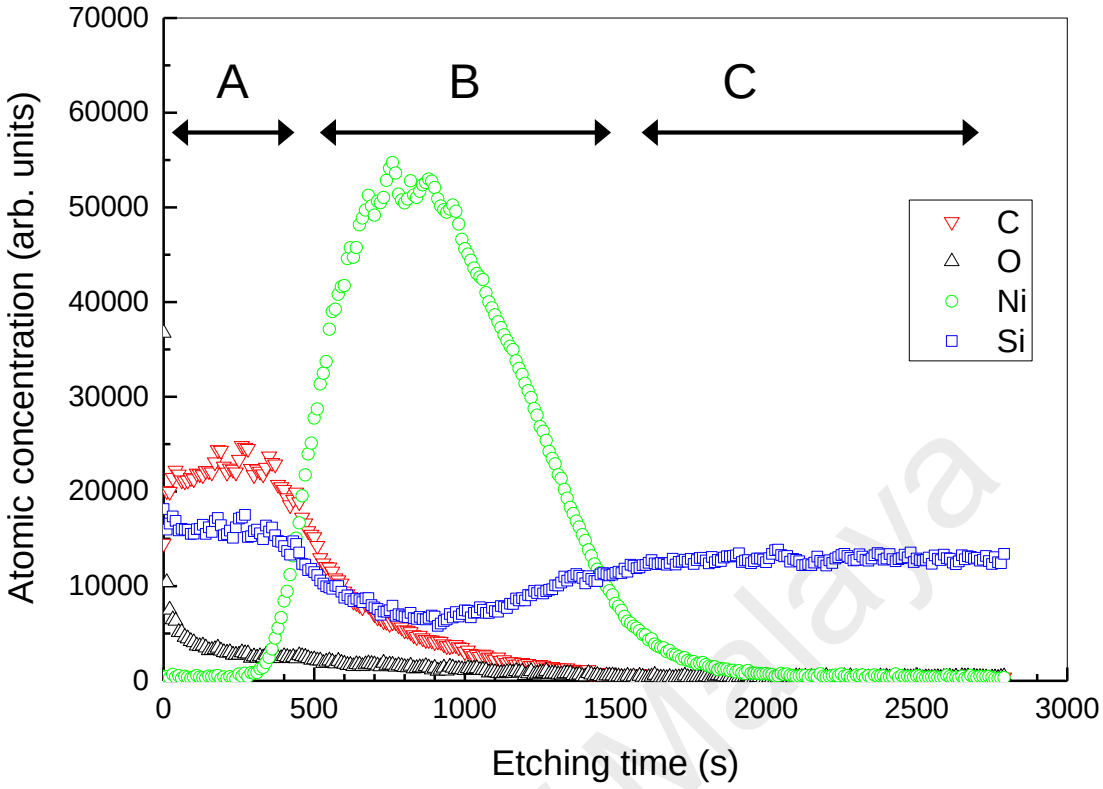

Figure 4.11: Auger elemental depth profiles of the nanowires.

With the results of the surface morphologies, EDX elemental analysis and Auger elemental depth profiles, the growth mechanism of these NiSi/SiC core-shell nanowires is proposed by the schematic diagrams as shown in Figure 4.12. The synthesis process involves a series of chemical reactions involving catalyst activation, alloying, nucleation and precipitation of nanowires. In addition, the formation of Ni nanoparticles acts as templates by the energetic atomic hydrogen contributed significantly to the growth of these well-aligned nanowires. Since the related deposition temperature was extremely lower than the eutectic temperature of Ni-Si (993°C) (Nash & Nash, 1987) and the precipitation of the nanowires is not lifted by solid catalyst particles (Kang et al., 2008; Kim et al., 2007; Lensch-Falk et al., 2009). Therefore, the growth of these NiSi/SiC core-shell nanowires could probably followed a growth mechanism which is different from catalyst growth mechanism.

University of Malaya

In the first reaction (a), the Ni film was subjected to energetic atomic hydrogen during the hydrogen plasma treatment at a substrate temperature of 450°C resulting in the Ni coalescing and forming Ni particles. A similar type of metallic nanoparticle formation were reported by Alet et al. (2008); Meshram et al. (2011), and Colli et al. (2007). The formation of the Ni nanoparticles by the hydrogen bombardment plasma treatment was also presented in our work (Goh & Abdul Rahman, 2014). Besides, the energetic atomic hydrogen bombardment also plays an important role by removing the oxide layer on the Ni film and subsequently activating the catalyst particles. In the second reaction (b), impinging of SiH_4 molecules on the surface of the Ni particles due to the gases flow direction, were catalytically decomposed by the Ni particles at temperature of 450°C. The decomposition of Si forms an accumulated Si layer on the particles.

Due to the diffusivity of Si and Ni, the latter diffused into the accumulated layer to initiate the formation of the first NiSi solid catalyst particle. The formation of NiSi at temperatures above 350°C is followed by a solid-diffusion control process described previously (Lavoie et. al, 2003). The continuous supply of Si until a Ni to Si ratio of about 1 is achieved results in nucleation. These NiSi solid catalyst particles act as nano-templates for the growth of the nanowires vertically. At reaction (c), the high thermal decomposition rate of SiH_4, CH_4 and H_2 by hot filament at temperatures above 1900°C supplied large amounts of H, Si- and C-rich species on the surface of the NiSi catalyst particles leading to a thicker layer of the accumulated Si. The sufficient diffusion of Ni into Si reach to a supersaturation stage or critical drop radius would precipitate the NiSi nanowires according to thermodynamic relation as described by Kim (2012).

In the thermodynamic relation, the NiSi particle size increases spontaneously with the diffusion of Ni into the Si layer, tend to reduce the surface free energy. However, the precipitation of NiSi nanowires only occur after reaching the critical drop radius in

University of Malaya

the maximum free energy region. During the growth, the hot-filament provides an extremely high surface temperature to the NiSi particle due to hydrogen-assisted heat transfer from the hot-filament (Tankala & DebRoy, 1992). The measured substrate surface temperature is approximately 785°C. This increases the surface mobility for Ni thus enhances the diffusion of Ni into Si layer. The hydrogen-assisted heat transfer sustains the diffusion of Ni and facilitates the growth of NiSi nanowires. The EDX results show a presence of C content in the deposited layer for the samples prepared with hot-filament and without hot-filament. However, the introduction of hot-filament increases the diffusion of C into the nanowires attributed to the decomposition of CH_4 in the gas-phase reactions by hot-filament.

According to the ternary Ni-Si-C phase diagram (Gülpen, 1995), there is no diffusion of SiC in the Ni or NiSi at temperatures below 850°C (The diffusivities of Si and SiC in NiSi are $5.7\text{-}5.9\times10^{-14}$ and 0.04×10^{-14} m^2/s, respectively at 850°C). As such, this reaction temperature is not sufficient to achieve a nucleation stage for precipitation of SiC, instead of NiSi, nanowires. Thus, the dissolved C atoms could absorb the excess Si, mainly through Si dangling bonds on the surface of the accumulated Si layer forming SiC clusters and promoting the formation of stable SiC nuclei. These stable SiC nuclei formed a shell radially surrounding the NiSi particles and its subsequent migrates on the NiSi nanowires as a shell nanowires during the precipitation of the nanowires, as shown in reaction (d). The solid-diffusion of NiSi followed the nucleation limited silicide reaction, and the surface-migration of SiC forms these single crystalline NiSi and amorphous SiC core-shell nanowires respectively. Finally, the growth of these core-shell nanowires deceases with the reduction of the reaction temperature or with insufficient supply of Si-rich species due to the termination of the hot-filament process.

University of Malaya

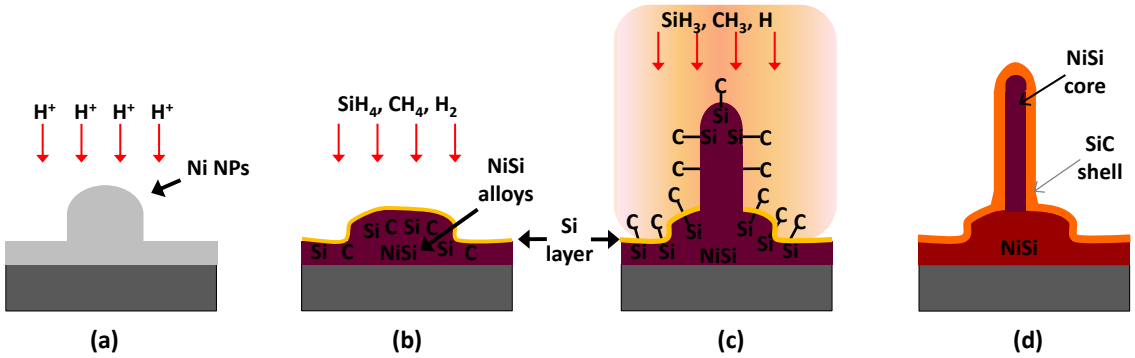

Figure 4.12: Growth mechanism of NiSi/SiC core-shell nanowires prepared by HWCVD.

4.2.3 Supercapacitor performances

Figures 4.13 (a&c) show photographs of the NiSi nanowires and NiSi/SiC core-shell nanowires grown on Ni foil substrates at substrate temperature of 450°C. These samples show dark-grey and dark-chocolate in color for NiSi nanowires and NiSi/SiC core-shell nanowires respectively. The morphologies of these nanowires are illustrated by FESEM images as shown in Figures 4.13(b&d). It can be observed that the former figure show a high density of NiSi nanowires growth uniformly on the Ni foil substrate with diameter and lengths about 60 nm and 2.83 μm, respectively. The latter figure presents a high density of vertically well aligned NiSi/SiC core-shell nanowires that uniformly distributed on the Ni foil substrate with diameter and lengths of nanowires about 133.40 nm and 1.34 μm, respectively. This morphology was similar to the nanowires grown on Si substrate as shown in Figure 4.1(c).

The XRD patterns of the NiSi nanowires and NiSi/SiC core-shell nanowires grown on Ni foil substrates are shown in Figure 4.14. Different phases of crystalline NiSi such as Ni_2Si, Ni_3Si_2, and NiSi were observed on both nanowires. The presence of Ni_2Si diffraction peaks located at 39.5°, 42.4°, 43.6°, 45.5°, 48.8°, and 76.3° are correspond to the crystalline planes of (211), (310), (021), (002), (301), and (040) [JCPDS card No. 01-073-2092]. The Ni_3Si_2 diffraction peak only observed at 44.4° corresponds to the crystalline planes of (600) [JCPDS card No. 17-0222]. In addition, it was clearly

University of Malaya

observed the presence of NiSi plane with orientation of (121) and (310) located at 47.3° and 51.8° [JCPDS card No: 65-1475]. This reveals an existence of NiSi core. Moreover, there was a small diffraction peak at 28.4° which could be attributed to crystalline Si plane of (111) orientation [JCPDS card No. 27-1402]. Furthermore, for NiSi/SiC core-shell nanowires, a broad SiC hump appear at 35.7° belonging to the (111) crystalline plane of 3C-SiC [JCPDS card No. 29-1129]. This similar diffraction pattern was observed for the both nanowires grown on Ni foil substrates as compared to the nanowires grown on Si substrate (Figure 4.8) which mainly consists of NiSi and Si. The appearances of other phases (Ni_3Si_2 & $NiSi_2$) for the nanowires grown on Ni foil substrates are from the deposited layer instead of nanowires.

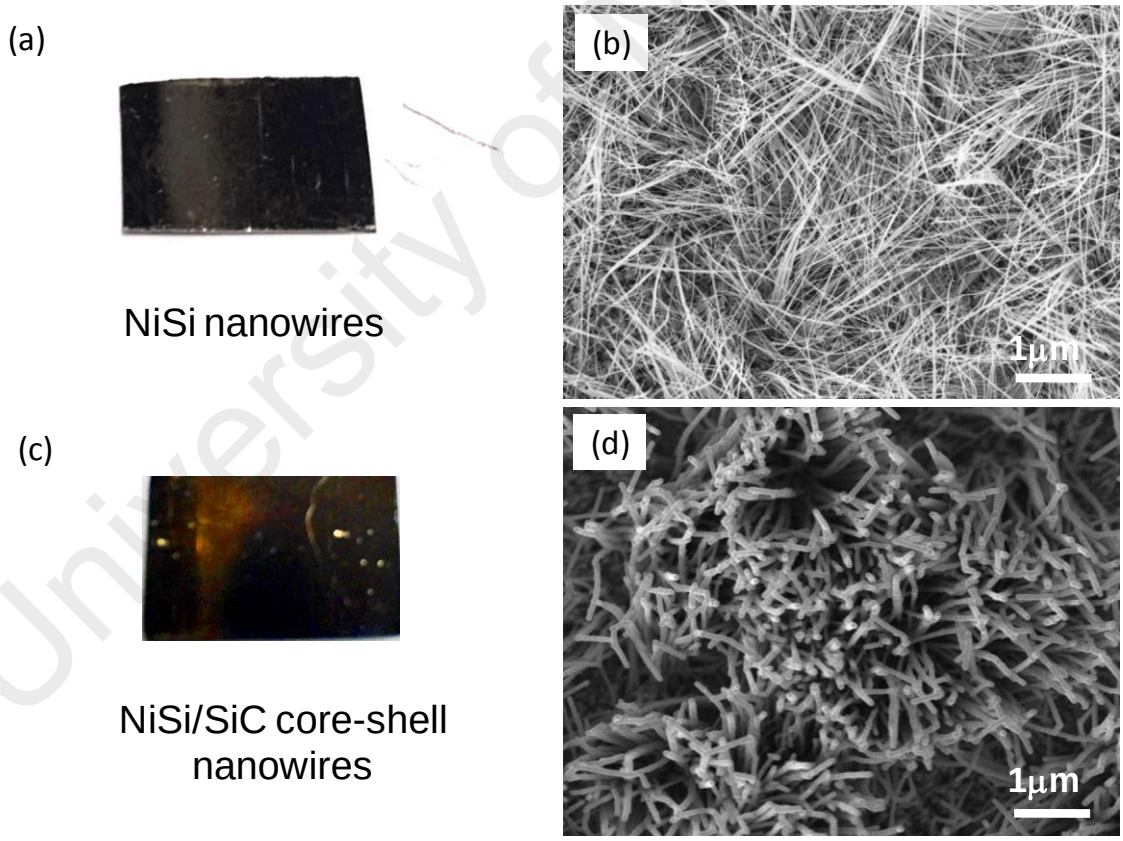

Figure 4.13: (a&c) Photograph of as-prepared NiSi and NiSi/SiC core-shell nanowires grown on Ni foil at substrate temperature of 450°C. (b&d) The FESEM images of the NiSi and NiSi/SiC core-shell nanowires.

University of Malaya

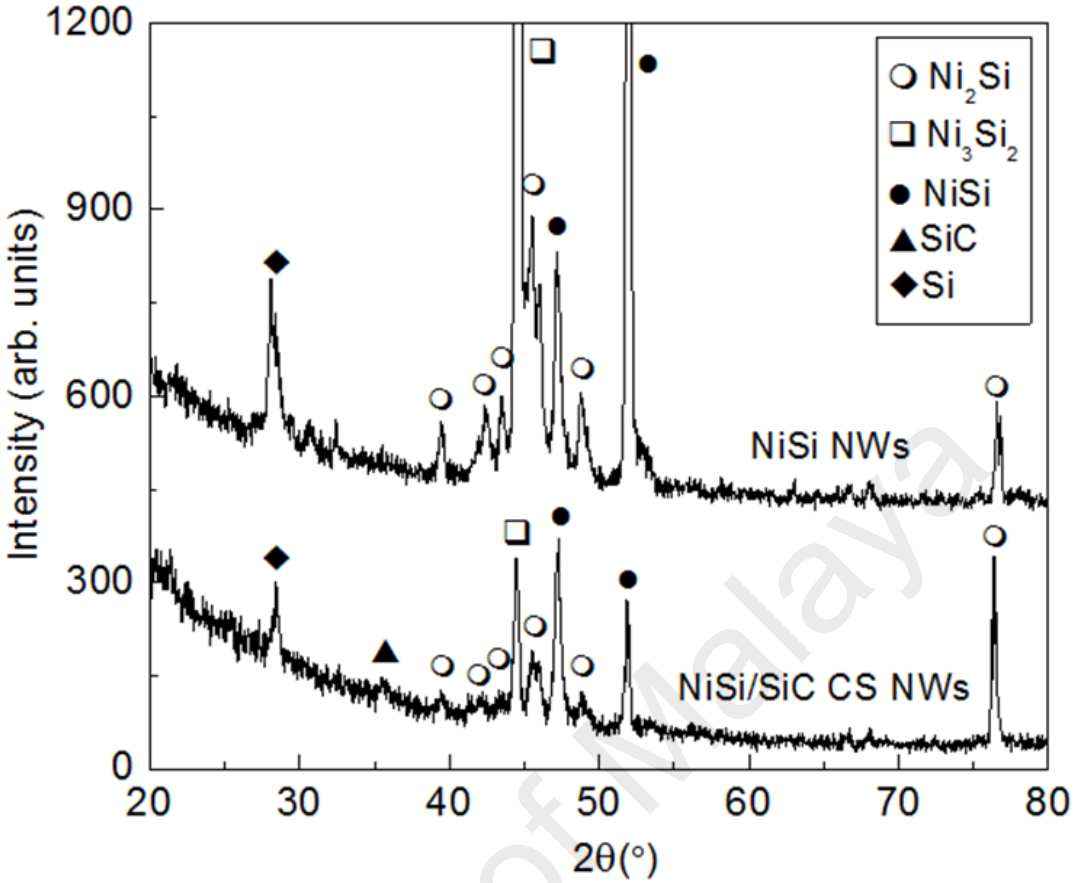

Figure 4.14: X-ray diffraction patterns (XRD) patterns of NiSi nanowires and NiSi/SiC core-shell nanowires grown on Ni foil substrates.

The electrochemical properties of the NiSi/SiC core-shell nanowires grown on Ni foil by HWCVD were comparatively studied, with control experiments on bare Ni foil and NiSi nanowires in a standard three-electrode configuration using 1.0 M KOH electrolytes over a potential window between 0 and 0.7 V. Control experiments are carried out in order to show an enhancement of electrochemical properties of NiSi/SiC core-shell nanowire electrode. Figure 4.15(a-c) shows the cyclic voltammetry (CV) curves of bare Ni foil, NiSi nanowires and NiSi/SiC core-shell nanowires at different scan rates of 10, 25, 50, and 100 mV/s. The CVs curves show two strong peaks corresponding to the typical pseudocapacitive behavior due to the occurrence of the faradic oxidation and reduction reactions between the nanowires and OH^- ions in the alkaline electrolytes (Guo et al., 2015; Yu et al., 2013). In addition, according to Dorp et al. (2007), faradic reaction of SiC can be described by the following equation:

University of Malaya

$$SiC + 6OH^- + 6h^+ \rightarrow SiO_2 + CO + 3H_2O \quad (4.2)$$

Therefore, the capacitance of the NiSi/SiC core-shell nanowire electrode is derived from a pseudocapacitive capacitance based on the obvious redox peaks. For all reactions, the anodic peak (oxidation) shifts to a higher potential while the cathodic peak (reduction) shifts to a lower potential as the scan rate increased from 10 to 100 mV/s. It may be resulted from the polarization effect in the electrode material (Zhang et al., 2015). As these figures clearly show, the overall NiSi/SiC core-shell nanowires exhibit much higher capacitive current density compared to the bare Ni foil and NiSi nanowires. By comparison, the shapes of NiSi/SiC core-shell nanowires CV curves did not change obviously with scan rate, suggesting that the electrode enabled excellent electrochemical reversibility and high rate capability (Zou et al., 2015). In addition, the integrated area of CV curve for NiSi/SiC core-shell nanowires is much larger than bare Ni foil and NiSi nanowire electrode, which indicates that the NiSi/SiC core-shell nanowire electrode has the highest capacity (Lee et al., 2012). As shown in Figure 4.15(a), current density is rather small compared with that of NiSi and NiSi/SiC core-shell nanowires. Therefore, the contribution of the substrate to the capacitance is ignored.

Figure 4.15(d) displays the calculated specific capacitance of bare Ni foil, NiSi nanowire electrode and NiSi/SiC core-shell nanowire electrodes. The specific capacitance was calculated from the CV curves using the following equations:

$$q = \frac{\int J(V)dV}{V_{scan}}, \quad (4.3)$$

$$C = \frac{q}{V_f - V_{io}}, \quad (4.4)$$

University of Malaya

where C is capacitance (F), q is quantity of electric charge (C), V_f is final potential, V_{io} is starting potential, $\int J(V)\,dV$ is the area under current density-potential curve, and V_{scan} is the potential scan rate for CV test (Chopra et al., 2015). The specific capacitance of NiSi/SiC core-shell nanowires is as high as 130 mF/cm^2, 102 mF/cm^2, 89 mF/cm^2, and 75 mF/cm^2, which is much higher than the NiSi nanowires (130 mFcm^{-2}, 63 mFcm^{-2}, 36 mFcm^{-2}, and 21 mFcm^{-2}) and the bare Ni foil (20 mFcm^{-2}, 19 mFcm^{-2}, 18 mFcm^{-2}, and 17 mF/cm^2) at scan rates of 10 , 25, 50, and 100 mV/s, respectively.

The excellent supercapacitor performance of NiSi/SiC core-shell nanowire electrode is due to the increased accessible surface area of the nanowires that exist in 1D. The nanowire electrode with SiC shell layers demonstrated a substantial the stability of the capacitance performance at higher scan rates. In addition, the higher electrical conductivity of the NiSi/SiC core-shell nanowires as compared to the intrinsic NiSi nanowires was proved by Nyquist plot shown in Figure 4.15(e). As compared to current reports, these NiSi/SiC core-shell nanowires exhibit a remarkable higher specific capacitance than the single SiC nanowires (0.4 mF/cm^2) and SiC-coated silicon nanowires (17 mF/cm^2) (Alper et al., 2013; Alper et al., 2012).

The electrochemical kinetics of NiSi and NiSi/SiC core-shell nanowires was further exemplified by electrochemical impedance spectra (EIS). Figure 4.15(e) illustrates the Nyquist plots of the NiSi and NiSi/SiC core-shell nanowire electrodes determined by EIS spectra in the frequency range from 10 kHz to 0.01 Hz. From the Nyquist plot, solution resistance (R_s) can be obtained from the Z' axis intercept at the high frequency end. Normally the spectrum shows a semicircle which is represented by a parallel combination of interfacial capacitance and resistance (Hastak et al., 2012; Hong et al., 2015). Based on figure, it clearly showed that the absence of semicircle in the high frequency region for NiSi and NiSi/SiC core-shell nanowire electrodes indicating that the contact between the electrode materials (NiSi and NiSi/SiC core-shell nanowires)

University of Malaya

and the current collector (Ni foil) are good. This result is similar with the previous work reported by Gu et al. (2015) and Gu et al. (2013). The NiSi nanowires electrode has the largest slope as compared to the NiSi/SiC core-shell nanowires electrode, indicating its best capacitive performance with a lower diffusion resistance (Kong et al., 2015). However, the inset clearly showed that the NiSi/SiC core-shell nanowires electrode has a lower equivalent series resistance (R_s) of 1.43 Ω compared to that of the NiSi nanowires electrode (R_s of 1.93 Ω). The relatively small R_s, demonstrates that the core-shell nanowires electrode possesses a higher electrical conductivity attributed to formation of the SiC nanocolumns.

University of Malaya

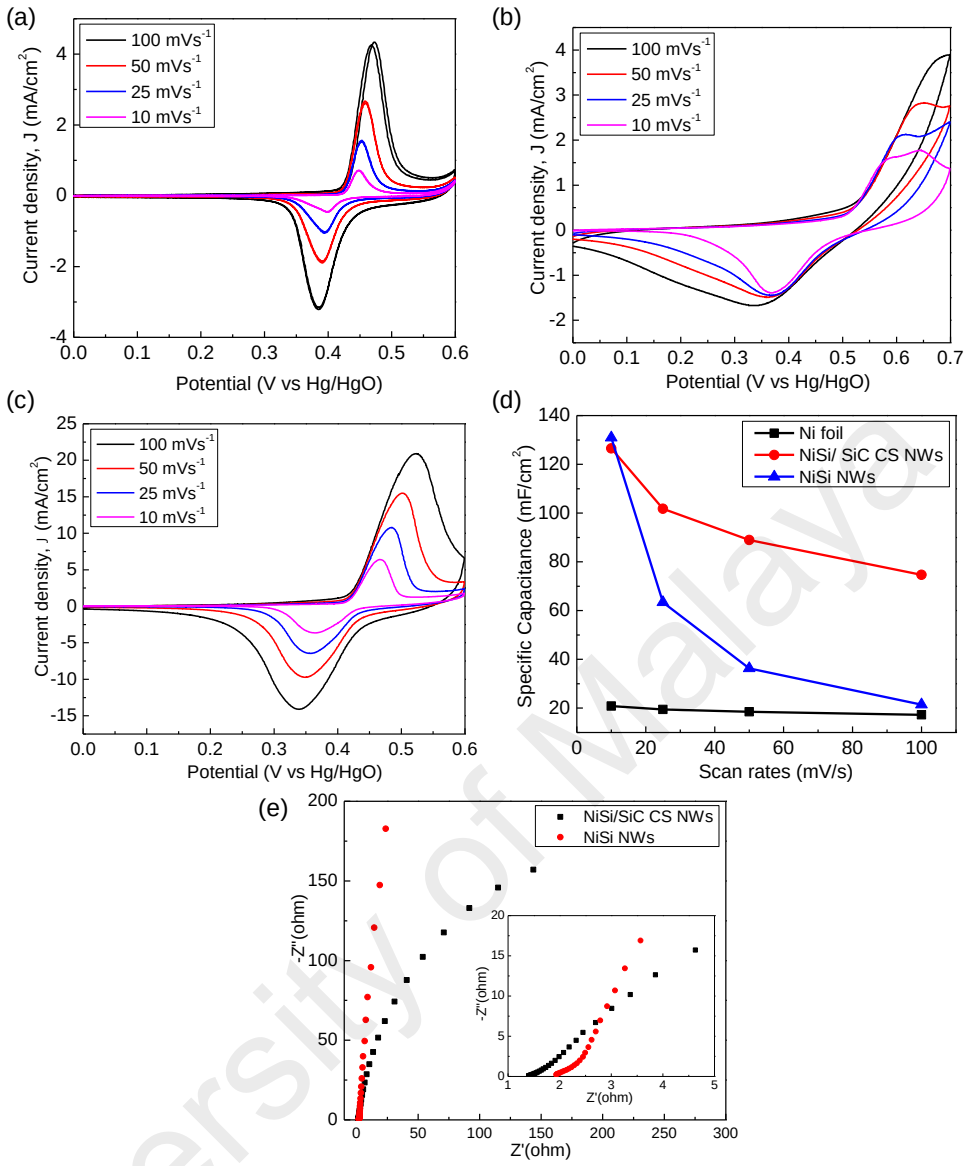

Figure 4.15: CV curves for (a) Ni foil (b) NiSi nanowires and (c) NiSi/SiC core-shell nanowires at different scan rates. (d) Specific capacitance of blank Ni foil, NiSi/SiC core-shell nanowires and NiSi nanowires. (e) Nyquist plot of NiSi nanowires (in black) and NiSi/SiC core-shell nanowires (in red).

The excellent supercapacitor performance of the NiSi/SiC core-shell nanowires can be attributed to the large specific surface area of the nanowires, the unique core–shell nanostructure together with the synergistic effects of the NiSi core and the SiC shell, and the selection of Ni foil as a conductive substrate. The high density of nanowires was widely reported to have extremely large specific surface area that increase the electrochemically contact areas between the electrodes and electrolyte ions thus

University of Malaya

enhanced the energy storage and good rate capability (Wang & Yan, 2014; Zhang et al., 2014).

The enhancement of the supercapacitance performance by the heterostructure NiSi/SiC core-shell nanowires can be attributed to several factors. The high density and vertically well aligned of the NiSi/SiC core-shell nanowires gives a large specific surface area for the charge accumulation during the electrochemical reactions. The synergistic effects of the heterostructure core-shell nanowires in improving the capacitance performance were reported extensively in literatures (Jiang et al., 2012; Wang et al., 2016). The highly metallic characteristic of NiSi core can act as a efficient current collector to form an effective conductive pathway for electron transport between the SiC shell and the Ni foil substrate leading to improve the capacitive activity. Moreover, the NiSi core also served as good scaffold to support SiC shell. The SiC nanocolumn shell coated on the NiSi core nanowires may relieve the stress exerted on inner nanowires caused by severe volume change, thus suppress the degradation of NiSi core (Huang et al., 2016).

Secondly, the formation of polycrystalline SiC nanocolumn shell provides the electrochemically available surface area for the charge accumulation and moreover, the SiC nano-crystallites increase the electroactive sites to further facilitate the transport of electrolyte ions thus remarkably improving the electrochemical performance even at high scan rates as demonstrated in Figure 4.15(c). Besides, the high specific surface area of SiC nanocolumns are favorable toward forming larger amount of double layers and promoting electrolyte ions intercalation/deintercalation, which enhances energy storage and improves the rate capability. In summary, the combination of NiSi and SiC as core-shell nanowires would give rise to a strong synergetic effect and good mechanical integrity for improving the electrochemical performances.

University of Malaya

4.3 Effect of CH_4 flow rates on the growth, structural and electrochemical properties of the NiSi/SiC core-shell nanowires

4.3.1 The morphological and structural properties of the NiSi/SiC core-shell nanowires

Figure 4.16(a-e) shows the surface morphologies of the NiSi/SiC core-shell nanowires grown by HWCVD at different CH_4 flow rates. The sample prepared at 0.5 sccm (Figure 4.16(a)) clearly illustrated that no formation of nanowires and only appearance of spherical grains of NiSi nanoparticle uniformly distributed on the substrate surface. The estimated average size of these nanoparticles was about 550 nm. As CH_4 flow rate increased to 1.5 sccm (Figure 4.16(b)), short nanowires become randomly distributed and were clearly observed on the surface of the substrate. There was also formation of NiSi nanoparticles on the substrate surface clearly shown in the inset figure.

An increase of CH_4 flow rate up to 2.0 sccm as shown in the Figure 4.16(c) enhances the growth of the nanowires. The high density of the nanowires was distributed uniformly on the substrate of the sample. Further, the nanowires also shows the formation of bumps along their lengths which increased along with CH_4 flow rate, as shown in the inset. However as CH_4 flow rate increased to 2.5 sccm, the density of nanowires started to decreased. In addition, as shown in the inset, the surfaces of nanowires were relatively smoother and less grainy compared to other samples. These nanowires demonstrate relatively better uniformity and alignments compared to other samples. The density of nanowires significantly decreased as CH_4 flow rates increased to 3.5 sccm as shown in Figure 4.16(e).

University of Malaya

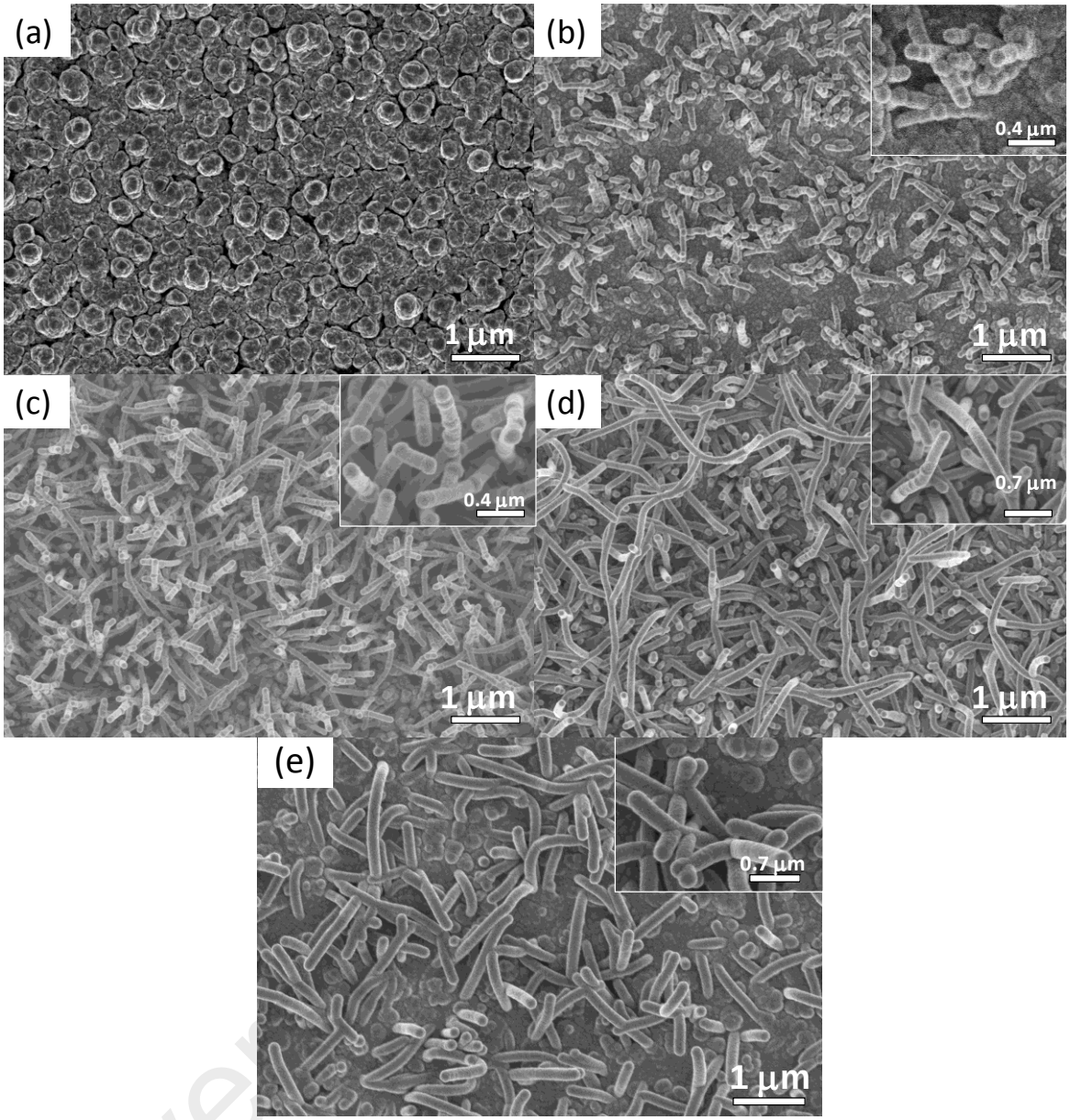

Figure 4.16: FESEM images of NiSi/SiC core-shell nanowires prepared by HWCVD at different CH_4 flow rates (a) 0.5 (b) 1.5 (c) 2.0 (d) 2.5, and (e) 3.5 sccm.

The variations in the average lengths, diameters and density of the nanowires against CH_4 flow rates were plotted in Figure 4.17. As shown in Figure 4.17, the diameters and lengths of the nanowires remain small for the CH_4 flow rate increased from 1.5 sccm to 2.0 sccm. The measured average diameters and lengths are 162 nm and 145 nm, and 0.76 μm and 0.93 μm, respectively. However, the average diameter and length increased to 250 nm and 2.27 μm, respectively with further increase in CH_4 flow rate from 2.0 sccm to 3.5 sccm. At the low CH_4 flow rates, low secondary gas phase

reactions of SiH_n and CH_n radials causes the low deposition of NiSi nanoparticles and SiC shells. Increase in the secondary gas phase reactions at the high CH_4 flow rates mainly enhances the deposition of SiC thus increasing the growth rate of the nanowires in both axial and radial directions.

Approximately 0 to 60 nanowires in 4.40 μm ×.6.32 μm of area were measured from each sample. Hence, the density of the nanowires can be calculated. The density of nanowires increased from 0 μm^{-2} to 1.51 μm^{-2} at 0.5 sccm to 2.0 sccm and decreased to 0.97 μm^{-2} at 3.5 sccm for nanowires grown at 0.5 sccm to 3.5 sccm, respectively. According to Tehrani (2015), an appropriate gas flow rate of SiH_4 and CH_4 into the reaction chamber is an important parameter to control the composition and structure of the SiC nanowires as it influences the density of radicals that generated and the probability of gas phase reactions. At low CH_4 flow rate (0.5 and 1.5 sccm), the concentration of CH_4 is too low as compared to SiH_4, thus allowed the generation of Si and H radicals from decomposition of SiH_4 on the heated filament and enhanced the density of H atoms reaching growth sites. As a result, more Si radicals diffuse into Ni nanoparticles thus forming NiSi solid particles.

As CH_4 flow rate is increased up to 2.0 sccm, the growth rate of the nanowires is enhanced. At this flow rate, the comparable of amount of secondary gas phase reactions of SiH_n and CH_n radicals on the substrate results an increase in the number of energetic H atoms reaching growth sites which results an increased number of nucleation sites and there for increased in precipitation of the nanowires. In addition, the comparable amount of SiH_n and CH_n radicals also influences the formation of SiC nano-crystallites as reported previously (Cheng et al., 2007; Lee et al., 2002). Further increase CH_4 flow rates to 3.5 sccm, significantly reduced the partial pressure of SiH_4 gas and consequently limited the number of Si and H radicals generated during SiH_4 decomposition by the hot filament and thus reduced the density of CH_n radicals

University of Malaya

reaching growth sites. In addition, the limited formation of H radicals reaching the growth sites also caused the reduction of H etching effects as a results decreased in nucleation sites. Hence, the formation of the nanowires decreased.

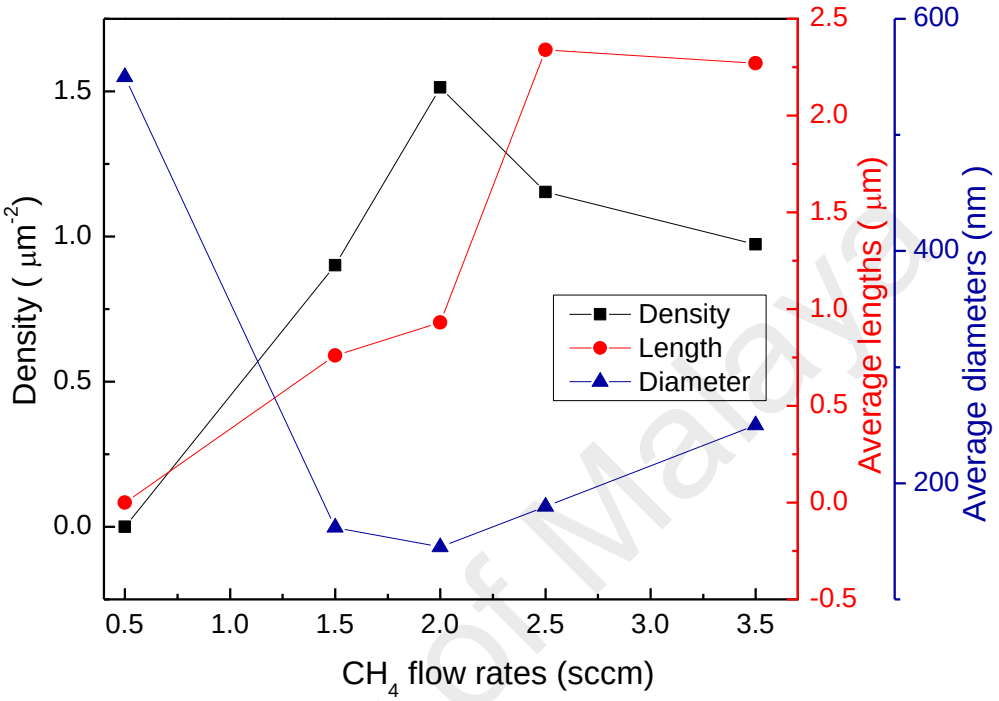

Figure 4.17: Variations in the density, average length and diameter of the nanowires at different CH_4 flow rates.

The variations in the deposition rates of the NiSi/SiC core-shell nanowires against CH_4 flow rates are plotted in Figure 4.18. The growth rate of nanowires shows increases gradually as CH_4 flow rates increase from 0.5 to 3.5 sccm. The deposition rates achieved its highest values at 7.57 nm/sec at 3.5 sccm. As reported in the previous report by Lien et al. (2011) and Shariatmadar Tehrani et al. (2013), the increase in CH_4 flow rates, increases secondary gas phase reactions of SiH_n and CH_n radicals with CH_4 molecules, which results in an increase in the number of energetic H atoms reaching the growth surface. This increases the H etching effect resulting in an increase in the number of nucleation sites and also the number of growth radicals reaching the growth surface. Therefore, the combined increase in the growth sites and growth radicals had

University of Malaya

contributes to the increase in the deposition rates. Moreover, an increase in SiH_n and CH_n radicals during deposition process also causes a higher Si-C bond formation (Figure 4.23(f)) and therefore enhances the deposition rates.

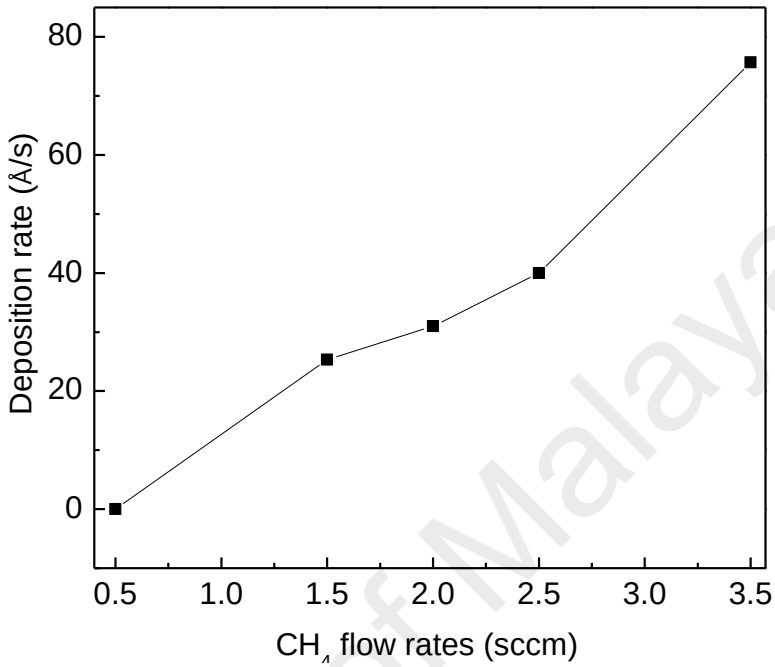

Figure 4.18: Variations in the deposition rate of the NiSi/SiC core-shell nanowires at different CH_4 flow rates.

The compositions of the nanowires were further investigated by STEM/EDS elemental mappings using a HAADF detector in the TEM, as shown in Figures 4.19. Figure 4.19(a) depicts a bright-field STEM image of typical single nanowire at CH_4 flow rate of 1.5 sccm on a carbon film supported by a TEM copper-grid. The image clearly reveals that the nanowire consists of a core-shell structure. The compositions of the nanowire were demonstrated by the EDS maps as shown in Figure 4.19(b-e) correspond to the Si, Ni, C and O maps respectively. Clearly, the presence of Ni along the center axis of the nanowire confirms its NiSi core (Figure 4.19(d)). Some NiSi bumps appearing near the center axis were also observed, indicating that the formation of the NiSi particles is due to the out-diffusion of NiSi core. A high density of Si and C as presented in Figure 4.19(b&c) reveal uniform distributions of Si and C in the shell of

University of Malaya

the nanowire. Furthermore, the uniform distribution of O along the length of the nanowire as illustrated in the O map (Figure 4.19(e)) indicates the formation of a SiO_X layer on the surface of the nanowires probably due to oxidation after the nanowires were were exposed to the atmospheric ambient.

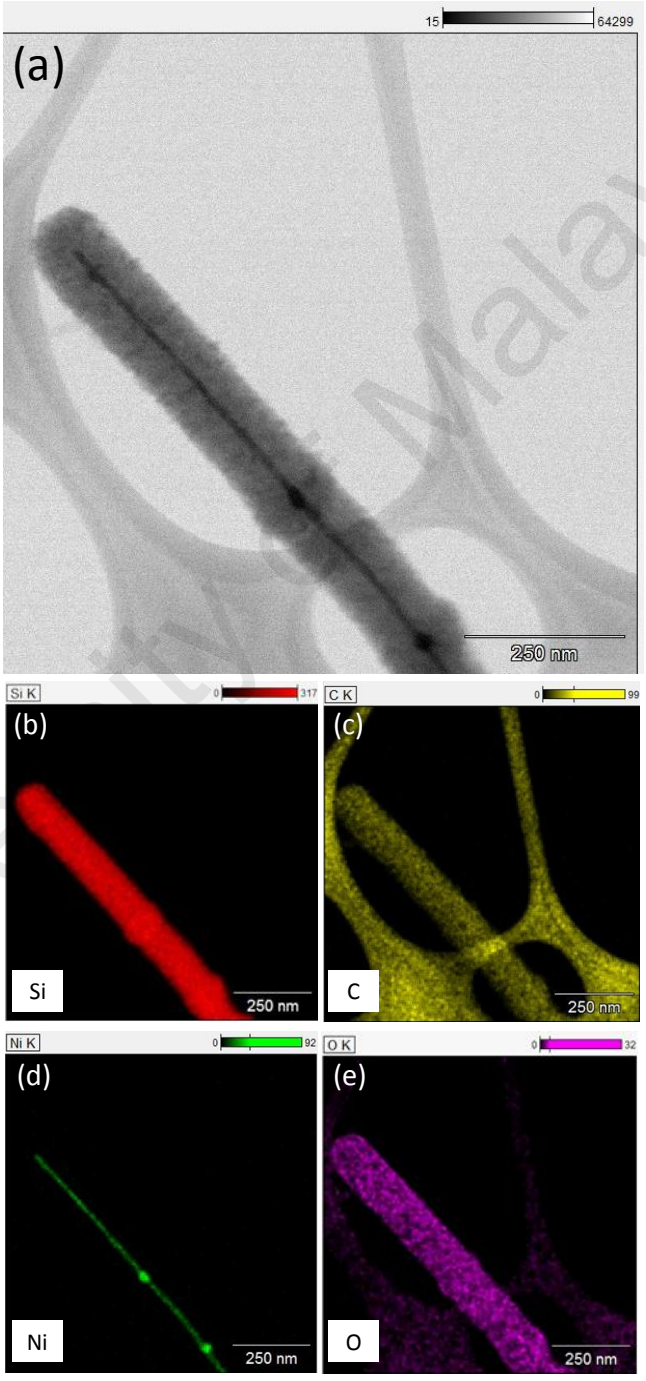

Figure 4.19: (a) Bright-field STEM image of NiSi/SiC core-shell nanowire prepared by HWCVD at CH_4 flow rate of 1.5 sccm. (b-e) EDS element maps of the core-shell nanowire.

University of Malaya

The microstructure of NiSi/SiC core-shell nanowires was investigated by TEM and HRTEM images as shown in Figure 4.20. These nanowires were prepared on top of a carbon film supported by a TEM copper-grid (Figure 4.20(a)). Figure 4.20(b) clearly illustrated the core and shell structure of the nanowire with their diameter being approximately about ~20 nm and ~120 nm respectively. The core-shell nanowires structure also proved by bright-field STEM image shown in Figure 4.19(a).

The HRTEM image near the edge of the core reveals a single-crystalline structure surrounded mainly by amorphous shell as clearly depicted in Figure 4.20(c). The NiSi core shows a single crystalline structure with lattice spacing of 0.21 nm corresponding to Ni_2Si (310) crystallographic plane [JCPDS card No. 01-073-2092]. This single crystalline Ni_2Si structure was further revealed by a Fast Fourier Transform (FFT) image, as shown in the inset. Figure 4.20(d), a HRTEM image obtained at the sidewall of the shell clearly reveals the presence of nano-crystallites embedded within an amorphous matrix. The estimated lattice spacing of about 0.25 nm corresponds to 3C-SiC (111) orientation [JCPDS card No. 29-1129]. The crystalline plane of 3C-SiC (111) was further revealed by the FFT image as shown in the inset. These nanocolumns were formed by the 3C-SiC nano-crystallites embedded within an amorphous matrix and the columnar structure acts as a shell of the nanowires.

University of Malaya

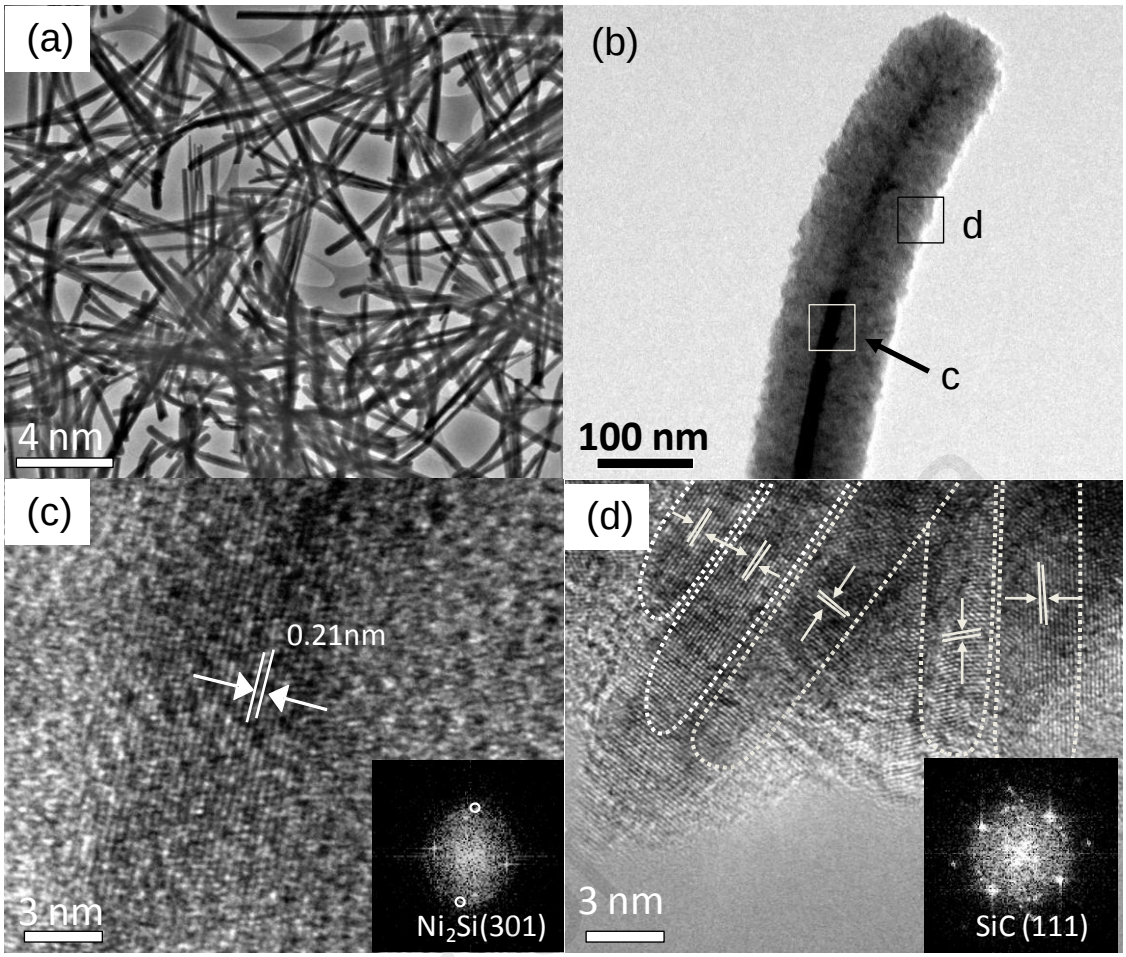

Figure 4.20: (a) TEM image of the NiSi/SiC core-shell nanowires grown at 2.0 sccm CH_4 flow rate. (b) A high magnification of a typical single NiSi/SiC core-shell nanowire as in (a). (c&d) HRTEM images obtained at the positions which are labeled in (b). Insets represent the FFT images of the respective figure in (c&d).

The Raman scattering spectra of the nanowires prepared at different CH_4 flow rates from 0.5 sccm to 3.5 sccm are shown in Figure 4.21 where Figure 4.21(a) represents the Raman scattering spectrum of the sample prepared at CH_4 flow rate at 0.5 sccm. It is clearly presented by crystalline Si TO band at 520 cm^{-1} in the spectrum (demonstrated in the inset). A small amount of amorphous components also presence in the spectra located at 150 cm^{-1}, 300 cm^{-1}, and 960 cm^{-1} corresponding to the transverse acoustic (TA), longitudinal acoustic (LA), and second-order of transverse optic (2TO) modes respectively (Liu et al., 2004). The presence of Si components indicates that there is a formation Si layer on top of the substrate. Therefore, the Ni nanoparticles as shown in Figure 4.16(a) are actually grown on top of the Si layer.

Figure 4.21(b) shows the Raman scattering spectra of the nanowires prepared at CH_4 flow rates of 1.5 sccm, 2.0 sccm, 2.5 sccm, and 3.5 sccm. The appearance of sharp crystalline NiSi excitation bands at 193 cm^{-1} and 210 cm^{-1} were clearly observed for the sample prepared above 0.5 sccm indicating the formation of the NiSi core in the nanowires (Lee et al., 2004). Moreover, at CH_4 flow rate of 2.5 sccm, a crystalline Ni_2Si excitation band at 140 cm^{-1} was also observed at this sample (Sasaki et al., 2006). In addition, the Raman spectra also showed two broad Raman excitation bands at 780 cm^{-1} and 910 cm^{-1} corresponding to transverse optic (TO) and longitudinal optic (LO) of SiC phases respectively (Monika et al., 2005). The position and the width of these bands did not significantly change with the increase in CH_4 flow rates. This implies a formation of SiC shell of the nanowires. Presence of these broad SiC excitation bands indicates a formation of SiC nano-crystallites embedded within an amorphous matrix in the shell as reported previously (Panda et al., 2010).

University of Malaya

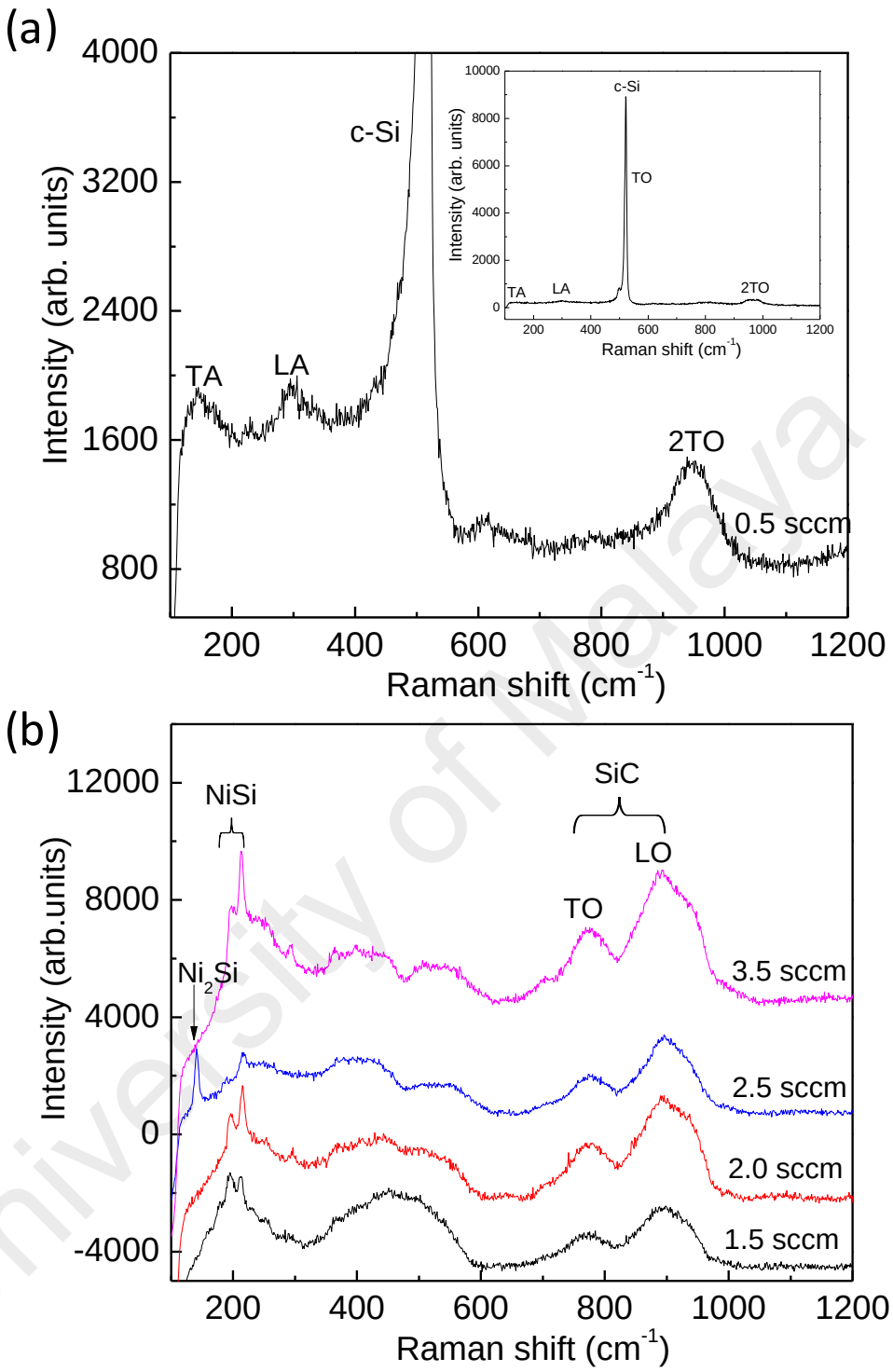

Figure 4.21: (a) Raman spectrum for NiSi/SiC core–shell nanowires prepared at 0.5 sccm. (b) Raman spectra for NiSi/SiC nanowires prepared at 1.5 sccm, 2.0 sccm, 2.5 sccm, and 3.5 sccm. Inset of (a) shows a whole Raman spectrum at 0.5 sccm.

University of Malaya

Figure 4.22 shows the XRD pattern of the core-shell nanowires prepared at different CH_4 flow rates. At low CH_4 flow rate (0.5 sccm), Si and NiSi peaks present in the nanowires. The Si phase located at 28.60°, 47.41°, and 56.33° belong to (111), (220), and (311) crystalline planes according to JCPDS card No. 01-077-2111. The appearance of NiSi phase located at 31.67°, 36.06°, 45.83°, and 51.44° which belong to (011), (102), (112), and (103) crystalline planes according to JCPDS card No. 38-0844. As CH_4 flow rate increases to 1.5 sccm, the Ni_3Si_2 and NiSi peaks appear in these spectra. The Ni_3Si_2 phases located at 28.04°, 29.19°, and 42.59° correspond to the (112), (400), and (023) crystalline phases according to JCPDS card No. 14-0429.

As CH_4 flow rate increases to 1.5 sccm, the Ni_3Si_2 and NiSi peaks appear in these spectra. The Ni_3Si_2 phases located at 28.04°, 29.19°, and 42.59° correspond to the (112), (400), and (023) crystalline phases according to JCPDS card No. 14-0429. As CH_4 flow rates increased to 2.0 sccm, the crystalline Ni_2Si and SiC peaks appears at these spectra. The crystalline Ni_2Si located at (111), (211), (310), (220), (301), (311), and (320) crystalline planes according to JCPDS card No. 01-073-2092. A broad SiC hump appeared at 35.7° belonging to the (111) crystalline plane of 3C-SiC according to the JCPDS card No. 29.1129. The same phases also appeared as CH_4 flow rates increased to 2.5 sccm. The higher intensity of diffraction for SiC peak at 2.5 sccm indicates higher crystallinity of SiC at higher CH_4 flow rate. The higher intensity of diffraction for SiC peak at 2.5 sccm indicates higher crystallinity CH_4 flow rate attributing to the higher gas-phase reactions.

By using Scherrer's equation, the crystallite size of the 3C–SiC can be estimated from the relation of $D = k\lambda / \beta \cos \theta$, where k, λ, β, and θ are the Scherrer's constant, the wavelength of X-ray (1.5402 Å), the full width at half maximum (FWHM), and the Bragg angle of the diffraction peak, respectively (Schubert et al., 2002). The estimated crystalline sizes for the nanowires grown at 2.0 sccm and 2.5 sccm are 6.77 nm and 6.99

University of Malaya

nm, respectively. An increased in CH_4 flow rate enhances the crystallite growth of SiC. At CH_4 flow rate of 3.5 sccm, only NiSi phase located at 31.59°, 36.06°, 45.83°, 47.28°, 51.44°, and 56.33° correspond to (002), (202), (103) and (013) crystalline planes. The formation of more stabilized NiSi phase were observed in the pattern indicating the presence of a crystalline NiSi core. However, no crystalline SiC diffraction peaks are observed in the pattern at high CH_4 flow rates. As compared to the Raman spectra, SiC is not significant in XRD patterns since it's forming amorphous SiC layer.

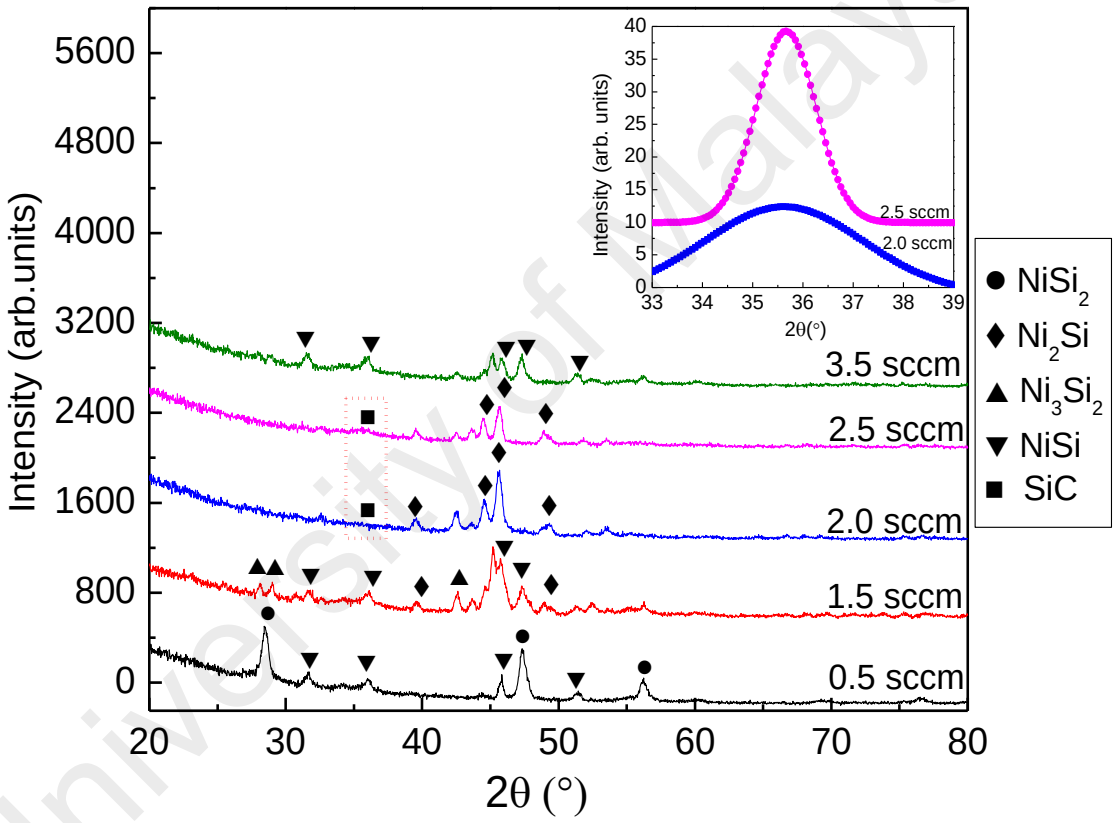

Figure 4.22: XRD spectra for NiSi/SiC core-shell nanowires prepared in different CH_4 low rates.

The chemical bonding states of NiSi/SiC core-shell nanowires was studied using x-ray photoelectron spectroscopy (XPS) analysis. Figure 4.23(a) shows the XPS wide scan of NiSi/SiC core-shell nanowires at different CH_4 flow rates from 0.5 sccm to 3.5 sccm. This spectrum clearly shows the presence of three main compositions such as

University of Malaya

silicon (Si 2p), carbon (C 1s) and oxygen (O 1s). Figure 4.23(b) shows high resolution XPS spectra of Si 2p peaks for various CH_4 flow rates. At lowest CH_4 flow rate (0.5 sccm), the Si 2p spectra exhibit two main peaks which are assigned to elemental NiSi (99.5 eV) and SiO_x (103.2 eV) peaks, respectively. The formation of Si-Ni bonds proved that the formation of NiSi nanoparticles were surrounded by SiO_x layer on the substrate surface at lowest CH_4 flow rate. When CH_4 flow rate increased to 3.5 sccm, the NiSi peak shifted to SiC peaks.

Furthermore, there are also overlap peaks in between NiSi and Si. Figure 4.23 (c-e) shows the chemical composition of NiSi/SiC core-shell nanowires by using XPS spectra at CH_4 flow rate of 2.0 sccm. The deconvolution of Si 2p band as shown in Figure 4.23(c) revealed that the band consists of four major components at 98.5 eV, 99.5 eV, 100.7 eV and 103.2 eV correspond to Si-Si (24.46%), Si-Ni (23.40%), Si-C (41.34%) and Si-O_x (7.28%) chemical states respectively. Figure 4.23(d) shows the deconvolution of the C 1s band into four chemical states of C-Si (11.65%), C=C (21.90%), C-C (64.28%) and O-C=O (2.16%) at 283.2 eV, 284.4 eV, 285.9 eV and 288.8 eV respectively. Figure 4.23(e) shows the deconvolution of the O 1s band. The spectrum can be decomposed to three Gaussian components located at 531.2 eV, 532.6 eV and 533.8 eV. These three O states are attributed to O=C (21.10%), O=Si (74.57%) and O-O (4.28%) (Tseng et al., 2013). The O=Si and oxide related bands are attributed to the formation of SiO_x layer on the surface of the nanowires. Figure 4.23(f) shows a graph of the normalized integrated area intensities for the NiSi, SiC, Si and SiO_x peaks as a function of CH_4 flow rates.

At lowest CH_4 flow rate (0.5 sccm), NiSi and SiO_x shows highest normalized integrated area intensities. Normalized integrated area intensities of SiC shows highest values at 0.47 as CH_4 flow rates increased to 3.5 sccm. This is because the addition of the CH_4 flow rate favors the SiH_4 as well as CH_4 dissociation, resulting in an increase of

University of Malaya

concentration of the SiH_n and CH_n radicals during the deposition process, that causes a higher Si-C bond (Lien et al., 2011). The largest percentages of Si-C and Si-Ni chemical states in the spectrum imply the formation of SiC shell and NiSi core in the nanowires respectively. Moreover, the integrated area intensities of SiO_x only quantified at a few percent and do not exceed 10% of total bonding for all CH_4 flow rates. Therefore, small amount of O content in the samples is expected no chemical reactions.

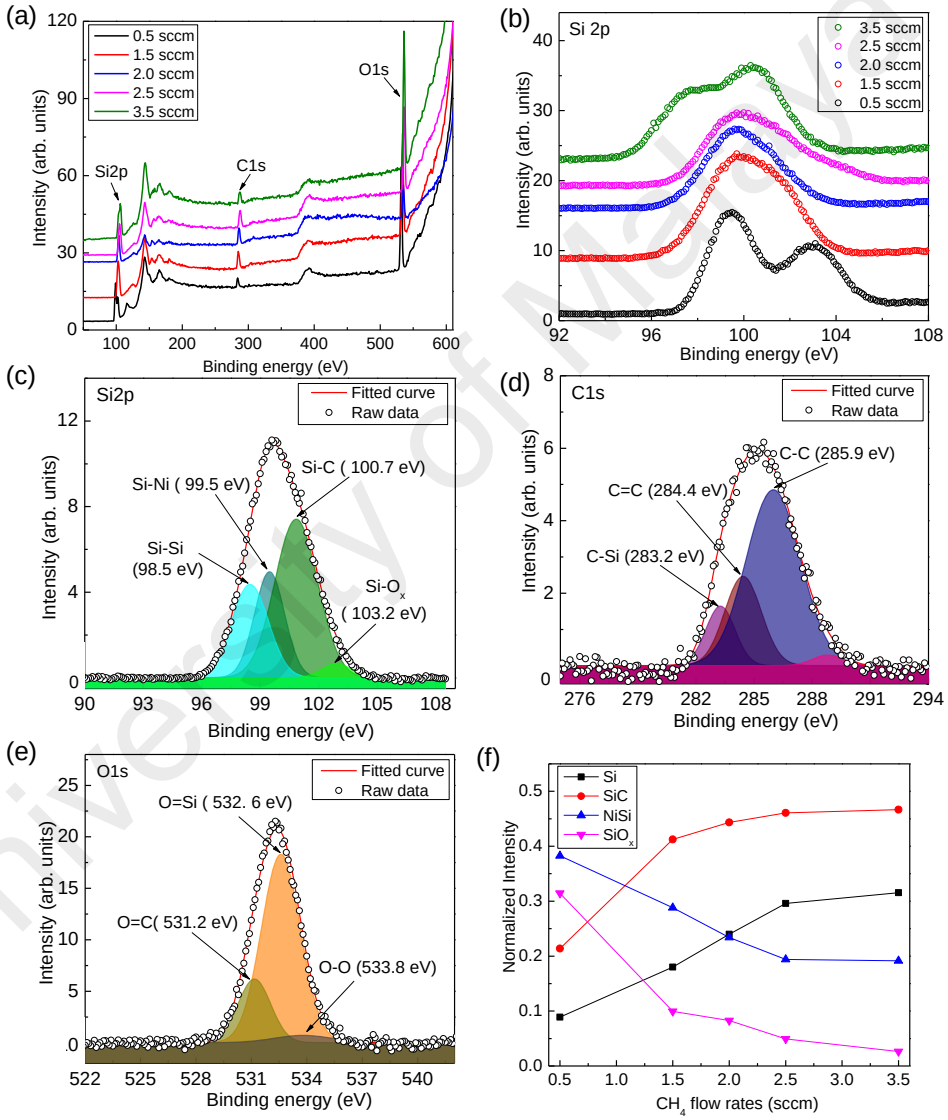

Figure 4.23: A wide scan of NiSi/SiC core-shell nanowires at different CH_4 flow rates. (b) XPS spectraof Si 2p for the nanowires grown at different CH_4 flow rates. (c) A typical deconvolution spectra of Si 2p for the NiSi/SiC core-shell nanowires. (d) A typical deconvolution spectra of C 1s for the NiSi/SiC core-shell nanowires. (e) A typical deconvolution spectra of O 1s for the NiSi/SiC core-shell nanowires. (f) The normalizes integrated area intensities for the Si 2p at different CH_4 flow rates.

University of Malaya

4.3.2 Supercapacitor performances

The electrochemical properties of the NiSi/SiC core-shell nanowires grown on Ni foil by HWCVD were studied in a standard three-electrode configuration by using 1.0 M KOH electrolytes over potential window of 0-0.6 V. Figure 4.24(a&b) shows the cyclic voltammetry (CV) curves of the bare Ni foil and NiSi/SiC core-shell nanowires at 2.0 sccm CH_4 flow rate at different scan rates of 10, 25, 50, and 100 mV/s. The shapes of the CV curves clearly confirmed the pseudocapacitive characteristics of NiSi/SiC core-shell nanowires due to the occurrence of the faradic oxidation and reduction reactions between the nanowires and OH^- ions in the alkaline electrolytes (Guo et al., 2015; Wang et al., 2011). In addition, for bare Ni foil electrode, the response current is relatively very weak, which can be neglected in contrast to that of the as-prepared NiSi/SiC core-shell electrode. Figure 4.24(c) shows the comparison of CV properties of NiSi/SiC core-shell nanowires at different CH_4 flow rates at 10 mV/s. Obviously, NiSi/SiC core-shell nanowire electrode at 2.0 sccm CH_4 flow rate shows higher current density and CV curve area than others flow rates. Figure 4.24(d) shows calculated specific capacitance of NiSi/SiC core-shell electrodes as a function of scan rates at different CH_4 flow rates.

The NiSi/SiC core-shell nanowire electrode at 2.0 sccm CH_4 flow rate possess high specific capacitance up to 819.74 mF/cm^2, 611.9 mF/cm^2, 409.11 mF/cm^2 and 234.13 mF/cm^2 at 10 mV/s, 25 mV/s, 50 mV/s and 100 mV/s, followed by 1.5 sccm (376.43 mF/cm^2, 291.39 mF/cm^2, 236.34 mF/cm^2, and 179.66 mF/cm^2), 2.5 sccm (232.79 mF/cm^2, 184.86 mF/cm^2, 159.37 mF/cm^2, and 133.27 mF/cm^2) and 3.5 sccm (168.35 mF/cm^2, 135.93 mF/cm^2, 117.43 mF/cm^2, and 98.71 mF/cm^2), respectively while formation of NiSi nanoparticles that grown at 0.5 sccm CH_4 flow rates shows lowest specific capacitance (126.5 mF/cm^2, 101.75 mF/cm^2, 88.97 mF/cm^2, and 74.69 mF/cm^2). It is well accepted that the rate capability is a vital factor for the

University of Malaya

supercapacitor in high power applications. The decline of the specific capacitance with increasing scan rate can be attributed to electrolytic ions diffusing and migrating into the active materials at low scan rates (Li et al., 2013).

As compared to other flow rates, nanowire electrode at 3.5 sccm shows the lowest specific capacitance due to its highest lengths. An increase the length of transport channel for electrons, resulting in large equivalent series resistance and poor electrochemical property (Gu et al., 2015). In addition, according to Soam et al. (2016), thickness of the shell are absolutely required to extract superior performance from the capacitor. As compared to other flow rates, nanowire electrode at 3.5 sccm has thicker nanowires shell structures that is at 120 nm (shown in the Appendix A). A large thickness of the shell causes a large potential drop across it owing to its poor electrical conductivity, thereby leading to the low value of the capacitance.

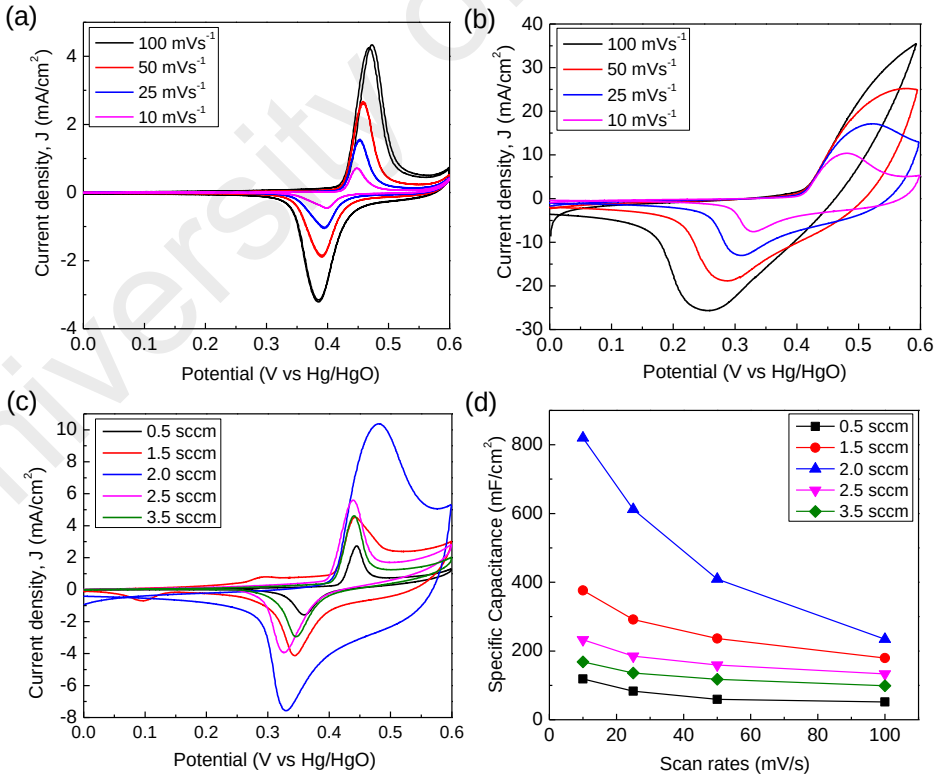

Figure 4.24: (a) CV curves of bare Ni foil at different scan rates, (b) CV curves of NiSi/SiC core-shell nanowires at 2.0 sccm CH_4 flow rate. (c) CV curves of NiS/SiC core-shell nanowires at different CH_4 flow rate at a scan rate of 10 mV/s. (d) The specific capacitances of NiSi/SiC core-shell nanowires different scan rates.

University of Malaya

Based on the measurements, the NiSi/SiC core-shell nanowire electrode at 2.0 sccm shows excellent supercapacitor performance as compared to other flow rate. The excellent supercapacitor performance of the NiSi/SiC core-shell nanowire electrode at 2.0 sccm CH_4 flow rates can be attributed to higher accessible surface area that mainly due to presence of high densities of the nanowires. The high density of nanowires reported to have an extremely large specific surface area that increased the electrochemically contact areas between the electrodes and electrolyte ions. Thus, enhanced the energy storage and good rate capability (Wang & Yan, 2014; Zhang et al., 2014). As shown in Figure 4.16(c), the presence of bumps along the nanowires that caused by the formation of NiSi nanoparticles on the surfaces of the nanowires could potentially grow nanowire branches. According to Gaboriau et al. (2016), the presence of high densities of branches can increased the electron conductivity within the nanowire electrode. Moreover, branches nanowires also have the merits of high specific capacitance, short electron and ion-transport pathways and good electrolyte infiltration, that would be promising for further improvement of the overall performance of pseudocapacitors (Zou et al., 2015).

Besides that, having thin SiC shell as compared to others flow rates at 34.38 nm (as shown in the table of Appendix B), help them to increase their supercapacitor performance. As reported previously, thin nanowires shell structure can enhance the electrochemical utilization of active sites as well as enable fast and reversible faradic reactions by shortening the ion diffusion path (Li et al., 2014; Yan et al., 2010). Hence, thin SiC shell could effectively shorten the transport path of ion diffusion through the solid phase and decrease the contact resistance between the SiC and NiSi which can significantly improve the charge transfer ability between the SiC shell and NiSi core.

University of Malaya

CHAPTER 5: CONCLUSION AND FUTURE WORKS

5.1 Conclusion

In this work, NiSi/SiC core-shell nanowires have been successfully grown by using home-built hot-wire chemical vapor deposition (HWCVD) system. The system has shown one of the most promising techniques for growing Si based nanowires at low temperature with high deposition rate and large-area deposition. It was found that the growth and structural of NiSi/SiC core-shell nanowires are consistently influenced by the substrate temperatures and CH_4 flow rates.

5.1.1 Effect of substrate temperatures on the growth, structural and electrochemical properties of the NiSi/SiC core-shell nanowires

The growth, structural and electrochemical properties of NiSi/SiC core-shell nanowires that prepared by HWCVD at different substrate temperature have been presented and investigated. High density of NiSi/SiC core-shell nanowires has been grown by HWCVD at a substrate temperature above 350°C. Further increased of substrate temperature has produced high density of vertically well aligned nanowires with smaller diameter and longer length of nanowires uniformly distributed on the substrate surface. Based on the structural and microstructure properties analysis, it clearly reveals that these heterostructure core-shell nanowires were constructed by a single crystalline NiSi core and an amorphous SiC shell. The shell clearly reveals polycrystalline structure of nanocolumn. The solid-diffusion of NiSi followed the nucleation limited silicide reaction, and the surface-migration of SiC formed these single crystalline NiSi and amorphous SiC core-shell nanowires respectively.

The NiSi/SiC core-shell nanowires electrode exhibited an excellent electrochemical performance as compared to the blank Ni foil and NiSi nanowires. The core-shell nanowire electrode showed a highest specific capacitance of approximately 75 mF/cm^2

University of Malaya

which nearly three times higher than the NiSi nanowires electrode (21 mF/cm^2) and four times higher than blank Ni foil electrode (17 mF/cm^2) at the highest scan rate (100 mV/s). The superior supercapacitor performances of the core-shell nanowire electrode can be attributed to its unique heterostructure core-shell together with their synergetic effect of the NiSi core and SiC shell, and also the formation of high density vertically aligned of nanowires.

5.1.2 Effect of CH_4 flow rates on the growth, structural and electrochemical properties of the NiSi/SiC core-shell nanowires

The growth, structural and electrochemical properties of NiSi/SiC core-shell nanowires prepared by HWCVD at different CH_4 flow rates have been presented and investigated. The production of H radicals that was form during decomposition of SiH_4 and CH_4 gases affects the formation of the nanowires. As increased CH_4 flow rate up to 2.0 sccm, the high density of nanowires uniformly distributed on the substrate surface due to comparable amount of SiH_n and CH_n radicals reaching the growth sites. As results, there are increased in the precipitation of the nanowires. However, increased CH_4 flow rate up to 3.5 sccm, significantly limited the number of Si and H radicals due to reduction of partial pressure of SiH_4 gas that consequently reduced the formation of the nanowires. The structural and microstructures properties also studies in this research. The microstructure of these nanowires reveals that they demonstrate single crystalline NiSi core and nanocrystalline SiC shells formed by SiC nanocolumns within an amorphous matrix. In addition, different CH_4 flow rates also affect the diameter of core and thickness of shell. Lowest diameter of core and thickness of shell of nanowires form at 2.0 sccm while increased CH_4 flow rate to 3.5 sccm increased the diameter of core and thickness of shell of nanowires.

University of Malaya

Moreover, increased of CH_4 flow rates significantly change from Si-rich silicides to NiSi phase. The formation of more stabilized NiSi leading to a deviation in the growth of the nanowires The NiSi/SiC core-shell nanowire electrodes at 2.0 sccm exhibited an excellent electrochemical performance as compared to other flow rates. The core-shell nanowire electrode showed a highest specific capacitance of approximately 234.13 mF/cm^2 at highest scan rate (100 mV/s). The excellent supercapacitor performance of the core-shell nanowire electrode can be attributed to higher accessible surface area that mainly due to presence of high densities of the nanowires and also due to lowest thickness of the shell that could effectively shorten the transport path of ion diffusion thus significantly improve the charge transfer ability between the SiC shell and NiSi core.

5.2 Future works

The results in this work can be strengthened further if more in-depth investigations especially on the electrochemical properties of the nanowire electrode such as cycle stability, conductivity and electrochemical reproducibility can be done. A few electrochemical measurements such as galvanostatic charge/discharge and cyclic performance will be taken in the future in order to confirm the improvement of supercapacitor performance of the electrode.

University of Malaya

REFERENCES

Agarwal, H. S. J. P. (2015). Highly crystalline silicon carbide thin films grown at low substrate temperature by HWCVD technique. *Journal of Materials Science: Materials in Electronics, 26*, 1381–1388.

Alet, P.-J., Eude, L., Palacin, S., & Cabarrocas, P. R. i. (2008). Transition from thin gold layers to nano-islands on TCO for catalyzing the growth of one-dimensional nanostructures. *Physica Status Solidi (A), 205*(6), 1429-1434.

Alper, J. P., Kim, M. S., Vincent, M., Hsia, B., Radmilovic, V., Carraro, C., & Maboudian, R. (2013). Silicon carbide nanowires as highly robust electrodes for micro-supercapacitors. *Journal of Power Sources, 230*(0), 298-302.

Alper, J. P., Vincent, M., Carraro, C., & Maboudian, R. (2012). Silicon carbide coated silicon nanowires as robust electrode material for aqueous micro-supercapacitor. *Applied Physics Letters, 100*(16), 163901.

Attolini, G., Watts, B. E., Fabbri, F., Rossi, F., Salviati, G., & Bosi, M. (2010). *Cubic SiC nanowires: Growth, characterization and applications*: INTECH Open Access Publisher.

Bai, X. D., Zhi, X., Liu, S., & Wang, E. G. (2005). Aligned 1D silicon nanostructure arrays by plasma etching. *Science and Technology of Advanced Materials, 6*(7), 804.

Bechelany, M., Brioude, A., Cornu, D., Ferro, G., & Miele, P. (2007). A Raman spectroscopy study of individual SiC nanowires. *Advanced Functional Materials, 17*(6), 939-943.

Bogner, A., Jouneau, P. H., Thollet, G., Basset, D., & Gauthier, C. (2007). A history of scanning electron microscopy developments: towards "wet-STEM" imaging. *Micron, 38*(4), 390-401.

Briggs, D. (1981). Handbook of X-ray Photoelectron Spectroscopy C. D. Wanger, W. M. Riggs, L. E. Davis, J. F. Moulder and G. E.Muilenberg Perkin-Elmer Corp., Physical Electronics Division, Eden Prairie, Minnesota, USA, 1979. . *Surface and Interface Analysis, 3*(4), v-v.

Calizo, I., Balandin, A., Bao, W., Miao, F., & Lau, C. (2007). Temperature dependence of the Raman spectra of graphene and graphene multilayers. *Nano Letters, 7*(9), 2645-2649.

Campos, L. C., Tonezzer, M., Ferlauto, A. S., Grillo, V., Magalhães-Paniago, R., Oliveira, S., Ladeira, L. O., & Lacerda, R. G. (2008). Vapor–solid–solid growth mechanism driven by epitaxial match between solid AuZn alloy catalyst particles and ZnO nanowires at low temperatures. *Advanced Materials, 20*(8), 1499-1504.

University of Malaya

Cao, L., Xu, F., Liang, Y. Y., & Li, H. L. (2004). Preparation of the novel nanocomposite $Co(OH)_2$/ultra-stable Y Zeolite and its application as a supercapacitor with high energy density. *Advanced Materials, 16*(20), 1853-1857.

Castner, E. W. (2005). Modern Spectroscopy, 4th Edition (J. Michael Hollas). *Journal of Chemical Education, 82*(1), 43.

Cavallotti, C., Di Stanislao, M., & Carrà, S. (2004). Interplay of physical and chemical aspects in the PECVD and etching of thin solid films. *Progress in Crystal Growth and Characterization of Materials, 48*, 123-165.

Chang, C.-H., Hsia, B., Alper, J. P., Wang, S., Luna, L. E., Carraro, C., Lu, S.-Y., & Maboudian, R. (2015). High-temperature all solid-state microsupercapacitors based on SiC nanowire electrode and YSZ electrolyte. *ACS Applied Materials & Interfaces, 7*(48), 26658-26665.

Chen, C., Shehata, S., Fradin, C., LaPierre, R., Couteau, C., & Weihs, G. (2007). Self-directed growth of AlGaAs core-shell nanowires for visible light applications. *Nano Letters, 7*(9), 2584-2589.

Chen, J., Zhang, J., Wang, M., Gao, L., & Li, Y. (2014). SiC nanowire film grown on the surface of graphite paper and its electrochemical performance. *Journal of Alloys and Compounds, 605*(0), 168-172.

Chen, K., Huang, Z., Huang, J., Fang, M., Liu, Y.-g., Ji, H., & Yin, L. (2013). Synthesis of SiC nanowires by thermal evaporation method without catalyst assistant. *Ceramics International, 39*(2), 1957-1962.

Chen, X., Guan, J., Sha, G., Gao, Z., Williams, C. T., & Liang, C. (2014). Preparation and magnetic properties of single phase Ni_2Si by reverse Rochow reaction. *RSC Advances, 4*(2), 653-659.

Chen, Y. Q., Zhang, K., Miao, B., Wang, B., & Hou, J. G. (2002). Temperature dependence of morphology and diameter of silicon nanowires synthesized by laser ablation. *Chemical Physics Letters, 358*(5–6), 396-400.

Cheng, H., Tu, R., Zhang, S., Han, M., Goto, T., & Zhang, L. (2017). Preparation of highly oriented β-SiC bulks by halide laser chemical vapor deposition. *Journal of the European Ceramic Society, 37*(2), 509-515.

Cheng, Q., Xu, S., Long, J., Huang, S., & Guo, J. (2007). Homogeneous nanocrystalline cubic silicon carbide films prepared by inductively coupled plasma chemical vapor deposition. *Nanotechnology, 18*(46), 465601.

Cheng, S.-L., & Chen, M.-F. (2012). Fabrication, characterization, and kinetic study of vertical single-crystalline CuO nanowires on Si substrates. *Nanoscale Research Letters, 7*(1), 1.

Chikkaraddy, R., Patra, P. P., Tripathi, R. P. N., Dasgupta, A., & Kumar, G. V. P. (2016). Plasmon-controlled excitonic emission from vertically-tapered organic nanowires. *Nanoscale, 8*(31), 14803-14808.

University of Malaya

Chiu, W.-L., Chiu, C.-H., Chen, J.-Y., Huang, C.-W., Huang, Y.-T., Lu, K.-C., Hsin, C.-L., Yeh, P.-H., & Wu, W.-W. (2013). Single-crystalline δ-Ni_2Si nanowires with excellent physical properties. *Nanoscale Research Letters, 8*(1), 1-5.

Choi, H.-J. (2012). Vapor–Liquid–Solid growth of semiconductor nanowires. In Yi, G.-C. (Ed.), *Semiconductor nanostructures for optoelectronic devices: Processing, characterization and applications* (pp. 1-36). Berlin, Heidelberg: Springer Berlin Heidelberg.

Chong, S. K., Goh, B. T., Aspanut, Z., Muhamad, M. R., Dee, C. F., & Rahman, S. A. (2011a). Effect of rf power on the growth of silicon nanowires by hot-wire assisted plasma enhanced chemical vapor deposition (HW-PECVD) technique. *Thin Solid Films, 519*(15), 4933-4939.

Chong, S. K., Goh, B. T., Aspanut, Z., Muhamad, M. R., Dee, C. F., & Rahman, S. A. (2011b). Effect of substrate temperature on gold-catalyzed silicon nanostructures growth by hot-wire chemical vapor deposition (HWCVD). *Applied Surface Science, 257*(8), 3320-3324.

Chopra, N., Wu, J., & Agrawal, P. (2015). Synthesis of nanoscale heterostructures comprised of metal nanowires, carbon nanotubes, and metal nanoparticles: Investigation of their structure and electrochemical properties. *Journal of Nanomaterials, 2015*, 1-13.

Choudhary, N., Li, C., Chung, H.-S., Moore, J., Thomas, J., & Jung, Y. (2016). High-performance one-body core/shell nanowire supercapacitor enabled by conformal growth of capacitive 2D WS_2 layers. *ACS Nano, 10 (12)*, 10726-10735.

Colli, A., Fasoli, A., Beecher, P., Servati, P., Pisana, S., Fu, Y., Flewitt, A. J., Milne, W. I., Robertson, J., Ducati, C., Franceschi, S. D., Hofmann, S., & Ferrari, A. C. (2007). Thermal and chemical vapor deposition of Si nanowires: Shape control, dispersion, and electrical properties. *Journal of Applied Physics, 102*(3), 034302.

Cui, L.-F., Ruffo, R., Chan, C. K., Peng, H., & Cui, Y. (2008). Crystalline-amorphous core−shell silicon nanowires for high capacity and high current battery electrodes. *Nano Letters, 9*(1), 491-495.

Djokoto, S. S., & Karimi, H. R. (2011, 17-19 Oct. 2011). *Modeling and simulation of a high pressure roller Crusher for silicon carbide production.* Paper presented at the 11t^h International Conference on Electrical Power Quality and Utilisation.

Dorp, D. H. v., Weyher, J. L., & Kelly, J. J. (2007). Anodic etching of SiC in alkaline solutions. *Journal of Micromechanics and Microengineering, 17*(4), S50-S55.

Doyle, J., Robertson, R., Lin, G. H., He, M. Z., & Gallagher, A. (1988). Production of high-quality amorphous silicon films by evaporative silane surface decomposition. *Journal of Applied Physics, 64*(6), 3215-3223.

Duan, X., Huang, Y., Agarwal, R., & Lieber, C. M. (2003). Single-nanowire electrically driven lasers. *Nature, 421*(6920), 241-245.

University of Malaya

Fan, H. J., Werner, P., & Zacharias, M. (2006). Semiconductor nanowires: From self-organization to patterned growth. *Small, 2*(6), 700-717.

Fang, B., & Binder, L. (2006). A modified activated carbon aerogel for high-energy storage in electric double layer capacitors. *Journal of Power Sources, 163*(1), 616-622.

Fang, S., Wang, H., Yang, J., Lu, S., Yu, B., Wang, J., & Zhao, C. (2016). Formation of Si nanowires by the electrochemical reduction of porous Ni/SiO_2 blocks in molten $CaCl_2$. *Journal of Physics and Chemistry of Solids, 89*, 1-6.

Farghaly, O., Hameed, R. A., & Abu-Nawwas, A.-A. H. (2014). Analytical application using modern electrochemical techniques. *International Journal of Electrochemical Science, 9*, 3287-3318.

Fu, W., Wang, Y., Han, W., Zhang, Z., Zha, H., & Xie, E. (2016). Construction of hierarchical $ZnCo_2O_4@Ni_xCo_{2x}(OH)_{6x}$ core/shell nanowire arrays for high-performance supercapacitors. *Journal of Materials Chemistry A, 4*(1), 173-182.

Fultz, B., & Howe, J. (2013). Diffraction and the X-Ray powder diffractometer. In *Transmission Electron Microscopy and Diffractometry of Materials* (pp. 1-57). Berlin, Heidelberg: Springer Berlin Heidelberg.

Gaboriau, D., Aradilla, D., Brachet, M., Le Bideau, J., Brousse, T., Bidan, G., Gentile, P., & Sadki, S. (2016). Silicon nanowires and nanotrees: Elaboration and optimization of new 3D architectures for high performance on-chip supercapacitors. *RSC Advances, 6*(84), 81017-81027.

Goh, B. T., & Saadah Abdul Rahman. (2014). Study of the growth, and effects of filament to substrate distance on the structural and optical properties of Si/SiC core–shell nanowires synthesized by hot-wire chemical vapor deposition. *Materials Chemistry and Physics, 147*(3), 974-981.

Goh, B. T., Zarina, A., Muhamad, M. R., & Saadah, A. R. (2012). Optical properties and crystallinity of hydrogenated nanocrystalline silicon (nc-Si:H) thin films deposited by rf-PECVD. *Vacuum, 86*(8), 1195-1202.

Goldstein, J., Newbury, D. E., Echlin, P., Joy, D. C., Romig Jr, A. D., Lyman, C. E., Fiori, C., & Lifshin, E. (2012). *Scanning electron microscopy and X-ray microanalysis: a text for biologists, materials scientists, and geologists*: Springer Science & Business Media.

Gomez-Martinez, A., Márquez, F., & Morant, C. (2016). Synthesis and characterization of amorphous SiO_2 nanowires directly grown on Cu substrates. *Journal of Sol-Gel Science and Technology*, 1-6.

Grob, J.-J. (2013). Ion Implantation. In *Silicon Technologies* (pp. 103-153): John Wiley & Sons, Inc.

Gu, L., Wang, Y., Fang, Y., Lu, R., & Sha, J. (2013). Performance characteristics of supercapacitor electrodes made of silicon carbide nanowires grown on carbon fabric. *Journal of Power Sources, 243*, 648-653.

University of Malaya

Gu, L., Wang, Y., Lu, R., Wang, W., Peng, X., & Sha, J. (2015). Silicon carbide nanowires/$Ni(OH)_2$ core–shell structures on carbon fabric for supercapacitor electrodes with excellent rate capability. *Journal of Power Sources, 273*(0), 479-485.

Gülpen, J. H., Kodentsov, A.A., Van Loo, F.J.J., et al. (1995). Growth of silicides in Ni-Si and Ni-SiC bulk diffusion couples. *Z. Metallkd., 86*(8), 530-539.

Guo, D., Ren, W., Chen, Z., Mao, M., Li, Q., & Wang, T. (2015). $NiMoO_4$ nanowire@MnO_2 nanoflake core/shell hybrid structure aligned on carbon cloth for high-performance supercapacitors. *RSC Advances, 5*(14), 10681-10687.

Guo, Y., Li, J., Chen, M., & Gao, G. (2015). Facile synthesis of vanadium pentoxide@ carbon core–shell nanowires for high-performance supercapacitors. *Journal of Power Sources, 273*, 804-809.

Hastak, R. S., Sivaraman, P., Potphode, D. D., Shashidhara, K., & Samui, A. B. (2012). High temperature all solid state supercapacitor based on multi-walled carbon nanotubes and poly[2,5 benzimidazole]. *Journal of Solid State Electrochemistry, 16*(10), 3215-3226.

Hofmann, S., Sharma, R., Wirth, C. T., Cervantes-Sodi, F., Ducati, C., Kasama, T., Dunin-Borkowski, R. E., Drucker, J., Bennett, P., & Robertson, J. (2008). Ledge-flow-controlled catalyst interface dynamics during Si nanowire growth. *Nature Materials, 7*(5), 372-375.

Hong, W., Wang, J., Li, Z., & Yang, S. (2015). Hierarchical Co_3O_4@Au-decorated PPy core/shell nanowire arrays: An efficient integration of active materials for energy storage. *Journal of Materials Chemistry A, 3*(6), 2535-2540.

Hsia, B., Kim, M. S., Luna, L. E., Mair, N. R., Kim, Y., Carraro, C., & Maboudian, R. (2014). Templated 3D ultrathin CVD graphite networks with controllable geometry: Synthesis and application as supercapacitor electrodes. *ACS Applied Materials & Interfaces, 6*(21), 18413-18417.

Hu, P., Dong, S., Zhang, D., Fang, C., & Zhang, X. (2016). Catalyst-assisted synthesis of core–shell SiC/SiO_2 nanowires via a simple method. *Ceramics International, 42*(1, Part B), 1581-1587.

Hu, Y., Liu, X., Zhang, X., Wan, N., Pan, D., Li, X., Bai, Y., & Zhang, W. (2016). Bead-curtain shaped SiC@SiO_2 core-shell nanowires with superior electrochemical properties for lithium-ion batteries. *Electrochimica Acta, 190*, 33-39.

Huang, L., Chen, D., Ding, Y., Feng, S., Wang, Z. L., & Liu, M. (2013). Nickel–cobalt hydroxide nanosheets coated on $NiCo_2O_4$ nanowires grown on carbon fiber paper for high-performance pseudocapacitors. *Nano Letters, 13*(7), 3135-3139.

Huang, M., Zhang, Y., Li, F., Zhang, L., Wen, Z., & Liu, Q. (2014). Facile synthesis of hierarchical Co_3O_4@MnO_2 core–shell arrays on Ni foam for asymmetric supercapacitors. *Journal of Power Sources, 252*, 98-106.

University of Malaya

Huang, Y., Shi, T., Jiang, S., Cheng, S., Tao, X., Zhong, Y., Liao, G., & Tang, Z. (2016). Enhanced cycling stability of $NiCo_2S_4$@NiO core-shell nanowire arrays for all-solid-state asymmetric supercapacitors. *Scientific Reports, 6*, 38620.

Huang, Z., Liu, H., Chen, K., Fang, M., Huang, J., Liu, S., Huang, S., Liu, Y.-g., & Wu, X. (2014). Synthesis and formation mechanism of twinned SiC nanowires made by a catalyst-free thermal chemical vapour deposition method. *RSC Advances, 4*(35), 18360-18364.

Jenkins, R. (2006). X-Ray Techniques: Overview. In *Encyclopedia of Analytical Chemistry*: John Wiley & Sons, Ltd.

Jha, H. S., & Agarwal, P. (2015). Highly crystalline silicon carbide thin films grown at low substrate temperature by HWCVD technique. *Journal of Materials Science: Materials in Electronics, 26*(3), 1381-1388.

Jiang, H., Li, C., Sun, T., & Ma, J. (2012). High-performance supercapacitor material based on $Ni(OH)_2$ nanowire-MnO_2 nanoflakes core-shell nanostructures. *Chemical Communications, 48*(20), 2606-2608.

Jiang, H., Ma, J., & Li, C. (2012). Hierarchical porous $NiCo_2O_4$ nanowires for high-rate supercapacitors. *Chemical Communications, 48*(37), 4465-4467.

Jiang, Y., Li, Z., Li, B., Zhang, J., & Niu, C. (2016). Ni_3Si_2 nanowires grown in situ on Ni foam for high-performance supercapacitors. *Journal of Power Sources, 320*, 13-19.

Joyce, H. J., Gao, Q., Tan, H. H., Jagadish, C., Kim, Y., Zhang, X., Guo, Y., & Zou, J. (2007). Twin-free uniform epitaxial GaAs nanowires grown by a two-temperature process. *Nano Letters, 7*(4), 921-926.

Kamble, M. M., Waman, V. S., Mayabadi, A. H., Ghosh, S. S., Gabhale, B. B., Rondiya, S. R., Rokade, A. V., Khadtare, S. S., Sathe, V. G., Shripathi, T., Pathan, H. M., Gosavi, S. W., & Jadkar, S. R. (2014). Hydrogenated silicon carbide thin films prepared with high deposition rate by hot wire chemical vapor deposition method. *Journal of Coatings, 2014*, 11.

Kamins, T. I., Williams, R. S., Chen, Y., Chang, Y.-L., & Chang, Y. A. (2000). Chemical vapor deposition of Si nanowires nucleated by $TiSi_2$ islands on Si. *Applied Physics Letters, 76*(5), 562-564.

Kang, K., Kim, D. A., Lee, H.-S., Kim, C.-J., Yang, J.-E., & Jo, M.-H. (2008). Low-temperature deterministic growth of Ge nanowires using Cu solid catalysts. *Advanced Materials, 20*(24), 4684-4690.

Kern, W. (1970). Cleaning solutions based on hydrogen peroxide for use in silicon semiconductor technology. *RCA Review, 31*, 187-206.

Khongwong, W., Yoshida, K., & Yano, T. (2010). Fabrication and properties of core-shell Ttype SiC/SiO_2 nanowires through low-cost production technique. In *Nanostructured Materials and Nanotechnology IV* (pp. 51-62): John Wiley & Sons, Inc.

University of Malaya

Kim, C. J., Kang, K., Woo, Y. S., Ryu, K. G., Moon, H., Kim, J. M., Zang, D. S., & Jo, M. H. (2007). Spontaneous chemical vapor growth of NiSi nanowires and their metallic properties. *Advanced Materials, 19*(21), 3637-3642.

Kim, J. (2012). Thermodynamic mechanism of nickel silicide nanowire growth. *Applied Physics Letters, 101*(23), 233103.

Kim, J., Anderson, W. A., Song, Y.-J., & Kim, G. B. (2005). Self-assembled nanobridge formation and spontaneous growth of metal-induced nanowires. *Applied Physics Letters, 86*(25), 253101.

Kim, J., Bae, J.-U., Anderson, W. A., Kim, H.-M., & Kim, K.-B. (2006). Solid-state growth of nickel silicide nanowire by the metal-induced growth method. *Journal of Materials Research, 21*(11), 2936-2940.

Kim, M., & Kim, J. (2014). Development of high power and energy density microsphere silicon carbide-MnO_2 nanoneedles and thermally oxidized activated carbon asymmetric electrochemical supercapacitors. *Physical Chemistry Chemical Physics, 16*(23), 11323-11336.

Kodas, T. (1994). Chemical vapor deposition: Principles and applications. Edited by M. L. Hitchman and K. F. Jensen, Academic Press, London 1993, 677 pp.,Advanced Materials., 6: 87–88. *Advanced Materials, 6*(1), 87-88.

Komura, Y., Tabata, A., Narita, T., Kanaya, M., Kondo, A., & Mizutani, T. (2007). Film properties of nanocrystalline 3C–SiC thin films deposited on glass substrates by hot-wire chemical vapor deposition using CH_4 as a carbon source. *Japanese Journal of Applied Physics, 46*(1R), 45.

Kong, D., Cheng, C., Wang, Y., Wong, J. I., Yang, Y., & Yang, H. Y. (2015). Three-dimensional Co_3O_4@C@Ni_3S_2 sandwich-structured nanoneedle arrays: Towards high-performance flexible all-solid-state asymmetric supercapacitors. *Journal of Materials Chemistry A, 3*(31), 16150-16161.

Korenblit, Y., Kajdos, A., West, W. C., Smart, M. C., Brandon, E. J., Kvit, A., Jagiello, J., & Yushin, G. (2012). In situ studies of ion transport in microporous supercapacitor electrodes at ultralow temperatures. *Advanced Functional Materials, 22*(8), 1655-1662.

LaLonde, A. D., Norton, M. G., Zhang, D., Gangadean, D., Alkhateeb, A., Padmanabhan, R., & McIlroy, D. N. (2011). Controlled growth of gold nanoparticles on silica nanowires. *Journal of Materials Research, 20*(11), 3021-3027.

Langford, J. I., Louër, D., Sonneveld, E. J., & Visser, J. W. (1986). Applications of total pattern fitting to a study of crystallite size and strain in zinc oxide powder. *Powder Diffraction, 1*(03), 211-221.

Laserna, J. (2006). Raman Spectroscopy: Introduction. In *Encyclopedia of Analytical Chemistry*: John Wiley & Sons, Ltd.

University of Malaya

Lauhon, L. J., Gudiksen, M. S., Wang, D., & Lieber, C. M. (2002). Epitaxial core-shell and core-multishell nanowire heterostructures. *Nature, 420*(6911), 57-61.

Lavoie, C., Detavernier, C., & Besser, P. (2004). Nickel silicide technology. *Ref, 2*, 95-152.

Lee, J. W., Hall, A. S., Kim, J.-D., & Mallouk, T. E. (2012). A facile and template-free hydrothermal synthesis of Mn_3O_4 nanorods on graphene sheets for supercapacitor electrodes with long cycle stability. *Chemistry of Materials, 24*(6), 1158-1164.

Lee, K. S., Mo, Y. H., Nahm, K. S., Shim, H. W., Suh, E. K., Kim, J. R., & Kim, J. J. (2004). Anomalous growth and characterization of carbon-coated nickel silicide nanowires. *Chemical Physics Letters, 384*(4–6), 215-218.

Lee, W.-H., Lin, J.-C., Lee, C., Cheng, H.-C., & Yew, T.-R. (2002). Effects of CH_4/SiH_4 flow ratio and microwave power on the growth of β-SiC on Si by ECR-CVD using CH_4/SiH_4/Ar at 200°C. *Thin Solid Films, 405*(1), 17-22.

Lefèvre, V. (2012). *Nanowires: Properties, Synthesis, and Applications*: Nova Science Publishers.

Lensch-Falk, J. L., Hemesath, E. R., Perea, D. E., & Lauhon, L. J. (2009). Alternative catalysts for VSS growth of silicon and germanium nanowires. *Journal of Materials Chemistry, 19*(7), 849-857.

Leonard, D. N., Chandler, G. W., & Seraphin, S. (2002). Scanning electron microscopy. In *Characterization of Materials*: John Wiley & Sons, Inc.

Li, H. B., Yu, M. H., Wang, F. X., Liu, P., Liang, Y., Xiao, J., Wang, C. X., Tong, Y. X., & Yang, G. W. (2013). Amorphous nickel hydroxide nanospheres with ultrahigh capacitance and energy density as electrochemical pseudocapacitor materials. *Nature Communications, 4*, 1894.

Li, N., Wang, J.-Y., Liu, Z.-Q., Guo, Y.-P., Wang, D.-Y., Su, Y.-Z., & Chen, S. (2014). One-dimensional ZnO/Mn_3O_4 core/shell nanorod and nanotube arrays with high supercapacitive performance for electrochemical energy storage. *RSC Advances, 4*(33), 17274-17281.

Li, S., Dong, Y.-F., Wang, D.-D., Chen, W., Huang, L., Shi, C.-W., & Mai, L.-Q. (2014). Hierarchical nanowires for high-performance electrochemical energy storage. *Frontiers of Physics, 9*, 303-322.

Lien, S.-Y., Weng, K.-W., Huang, J.-J., Hsu, C.-H., Shen, C.-T., Wang, C.-C., Lin, Y.-S., Wuu, D.-S., & Wu, D.-C. (2011). Influence of CH_4 flow rate on properties of HF-PECVD a-SiC films and solar cell application. *Current Applied Physics, 11*(1, Supplement), S21-S24.

Lin, J.-Y., Hsu, H.-M., & Lu, K.-C. (2015). Growth of single-crystalline nickel silicide nanowires with excellent physical properties. *Crystal Engineering Communications, 17*(9), 1911-1916.

University of Malaya

Lin, R., Taberna, P.-L., Fantini, S., Presser, V., Pérez, C. R., Malbosc, F., Rupesinghe, N. L., Teo, K. B. K., Gogotsi, Y., & Simon, P. (2011). Capacitive energy storage from −50 to 100°C using an ionic liquid electrolyte. *The Journal of Physical Chemistry Letters, 2*(19), 2396-2401.

Liu, C., Li, F., Ma, L. P., & Cheng, H. M. (2010). Advanced materials for energy storage. *Advanced Materials, 22*(8), E28–E62.

Liu, J., Niu, J., Yang, D., Yan, M., & Sha, J. (2004). Raman spectrum of array-ordered crystalline silicon nanowires. *Physica E: Low-Dimensional Systems and Nanostructures, 23*(1–2), 221-225.

Liu, R., Duay, J., Lane, T., & Bok Lee, S. (2010). Synthesis and characterization of RuO_2/poly(3,4-ethylenedioxythiophene) composite nanotubes for supercapacitors. *Physical Chemistry Chemical Physics, 12*(17), 4309-4316.

Long, Y.-Z., Yu, M., Sun, B., Gu, C.-Z., & Fan, Z. (2012). Recent advances in large-scale assembly of semiconducting inorganic nanowires and nanofibers for electronics, sensors and photovoltaics. *Chemical Society Reviews, 41*(12), 4560-4580.

Maboudian, R., Carraro, C., Senesky, D. G., & Roper, C. S. (2013). Advances in silicon carbide science and technology at the micro-and nanoscales. *Journal of Vacuum Science & Technology A, 31*(5), 050805.

Mahan, A. H., Bauer, G. H., Fuhs, W., Ley, L., Nelson, B. P., Salamon, S., & Crandall, R. S. (1991). Deposition of device quality, low H content a-Si:H by the hot wire technique. *Journal of Non-Crystalline Solids, 137*, 657-660.

Masarapu, C., Zeng, H. F., Hung, K. H., & Wei, B. (2009). Effect of temperature on the capacitance of carbon nanotube supercapacitors. *ACS Nano, 3*(8), 2199-2206.

Massalski, T. B., Okamoto, H., & International, A. S. M. (1990). *Binary alloy phase diagrams*. Materials Park, Ohio: ASM International.

Matsumura. (1991). Formation of polysilicon films by catalytic chemical vapor deposition (cat-CVD) method. *Japanese Journal of Applied Physics, 30*(8B), L1522.

Matsumura. (1998). Formation of silicon-based thin films prepared by catalytic chemical vapor deposition (Cat-CVD) Method. *Japanese Journal of Applied Physics, 37*(6R), 3175.

Meshram, N. P., Kumbhar, A., & Dusane, R. O. (2011). Silicon nanowire growth on glass substrates using hot wire chemical vapor deposition. *Thin Solid Films, 519*(14), 4609-4612.

Molnár, L. M., Mojzes, I., & Misák, S. (2009). 1D nanostructures grown on GaAs and InP substrates. *Periodica Polytechnica Electrical Engineering, 52*(1-2), 111-115.

University of Malaya

Monika, W., Yuejian, W., & Zerda, T. W. (2005). Raman spectra of silicon carbide small particles and nanowires. *Journal of Physics: Condensed Matter, 17*(15), 2387.

Morosanu, C. E. (2013). *Thin films by chemical vapour deposition* (Vol. 7): Elsevier.

Nash, P., & Nash, A. (1987). The Ni−Si (Nickel-Silicon) system. *Bulletin of Alloy Phase Diagrams, 8*(1), 6-14.

Ngo, P. D. (1999). Energy Dispersive Spectroscopy. In Wagner, L. C. (Ed.), *Failure analysis of integrated circuits: Tools and techniques* (pp. 205-215). Boston, MA: Springer US.

Nozaki, Y., Kitazoe, M., Horii, K., Umemoto, H., Masuda, A., & Matsumura, H. (2001). Identification and gas phase kinetics of radical species in Cat-CVD processes of SiH_4. *Thin Solid Films, 395*(1–2), 47-50.

Nur Fatin Farhanah Nazarudin, Nurul Jannah Mohd Noor, Saadah Abdul Rahman, & Goh, B. T. (2015). Photoluminescence and structural properties of Si/SiC core–shell nanowires growth by HWCVD. *Journal of Luminescence, 157*(0), 149-157.

Panda, S. K., Sengupta, J., & Jacob, C. (2010). Synthesis of β -SiC/SiO_2 core-sheath nanowires by CVD technique using Ni as catalyst. *Journal of Nanoscience and Nanotechnology, 10*(5), 3046-3052.

Park, J.-H., & Sudarshan, T. (2001). *Chemical vapor deposition* (Vol. 2): ASM International.

Patterson, A. L. (1939). The scherrer formula for X-Ray particle size determination. *Physical Review, 56*(10), 978-982.

Pawbake, A., Mayabadi, A., Waykar, R., Kulkarni, R., Jadhavar, A., Waman, V., Parmar, J., Bhattacharyya, S., Ma, Y. R., Devan, R., Pathan, H., & Jadkar, S. (2016). Growth of boron doped hydrogenated nanocrystalline cubic silicon carbide (3C-SiC) films by Hot Wire-CVD. *Materials Research Bulletin, 76*, 205-215.

Persson, A. I., Larsson, M. W., Stenström, S., Ohlsson, B. J., Samuelson, L., & Wallenberg, L. R. (2004). Solid-phase diffusion mechanism for GaAs nanowire growth. *Nature Materials, 3*(10), 677-681.

Philip, J. (2011). Silicide nanowires from coordination compound precursors. In Hashim, A. (Ed.), *Nanowires - Fundamental Research* (pp. Ch. 06). Rijeka: InTech.

Prakash, J., Dasgupta, K., Kumar, B., Ghosh, S. K., & Chakravartty, J. K. (2014). Role of SiC nanowire coating on oxidation behavior of carbon fibers: Kinetic and thermodynamic study. *Surface and Coatings Technology, 259*, 637-646.

Ruff, M., Mitlehner, H., & Helbig, R. (1994). SiC devices: Physics and numerical simulation. *IEEE Transactions on Electron Devices, 41*(6), 1040-1054.

University of Malaya

Ruud E. I, S. (2002). Advances in solar cells made with hot wire chemical vapor deposition (HWCVD): Superior films and devices at low equipment cost. *Thin Solid Films, 403–404*, 17-25.

Sasaki, T., Nishibe, S., Harima, H., Isshiki, T., Yoshimoto, M., Kisoda, K., Yoo, W. S., & Fukada, T. (2006, 10-13 Oct. 2006). *Raman study of low-temperature formation of nickel sllicide Layers.* Paper presented at the 2006 14th IEEE International Conference on Advanced Thermal Processing of Semiconductors.

Schubert, C., Kaiser, U., Hedler, A., Wesch, W., Gorelik, T., Glatzel, U., Kräußlich, J., Wunderlich, B., Heß, G., & Goetz, K. (2002). Nanocrystal formation in SiC by Ge ion implantation and subsequent thermal annealing. *Journal of Applied Physics, 91*(3), 1520-1524.

Senesky, D. G., Jamshidi, B., Cheng, K. B., & Pisano, A. P. (2009). Harsh environment silicon carbide sensors for health and performance monitoring of aerospace systems: A review. *IEEE Sensors Journal, 9*(11), 1472-1478.

Service, R. F. (2006). Materials science. New 'supercapacitor' promises to pack more electrical punch. *Science, 313*(5789), 902.

Shariatmadar Tehrani, F., Goh, B., Muhamad, M., & Rahman, S. (2013). Pressure dependent structural and optical properties of silicon carbide thin films deposited by hot wire chemical vapor deposition from pure silane and methane gases. *Journal of Materials Science: Materials in Electronics, 24*(4), 1361-1368.

Sharma, R., Bisen, D., Shukla, U., & Sharma, B. (2012). X-ray diffraction: a powerful method of characterizing nanomaterials. *Recent Research in Science and Technology, 4*(8), 77-79.

Shi, F., Li, L., Wang, X.-l., Gu, C.-d., & Tu, J.-p. (2014). Metal oxide/hydroxide-based materials for supercapacitors. *RSC Advances, 4*(79), 41910-41921.

Simon, P., & Gogotsi, Y. (2008). Materials for electrochemical capacitors. *Nature Materials, 7*(11), 845-854.

Soam, A., Arya, N., Kumbhar, A., & Dusane, R. (2016). Controlling the shell microstructure in a low-temperature-grown SiNWs and correlating it to the performance of the SiNWs-based micro-supercapacitor. *Applied Nanoscience, 6*(8), 1159-1165.

Stoffel, A., Kovács, A., Kronast, W., & Müller, B. (1996). LPCVD against PECVD for micromechanical applications. *Journal of Micromechanics and Microengineering, 6*(1), 1.

Taberna, P. L., Mitra, S., Poizot, P., Simon, P., & Tarascon, J. M. (2006). High rate capabilities Fe_3O_4-based Cu nano-architectured electrodes for lithium-ion battery applications. *Nature Materials, 5*(7), 567-573.

Tankala, K., & DebRoy, T. (1992). Modeling of the role of atomic hydrogen in heat transfer during hot filament assisted deposition of diamond. *Journal of Applied Physics, 72*(2), 712-718.

University of Malaya

Tehrani, F. S. (2015). Transformation from amorphous to nano-crystalline SiC thin films prepared by HWCVD technique without hydrogen dilution. *Bulletin of Materials Science, 38*(5), 1333-1338.

Tonokura, K., Inoue, K., & Koshi, M. (2002). Chemical kinetics for film growth in silicon HWCVD. *Journal of Non-Crystalline Solids, 299–302, Part 1*, 25-29.

Tseng, I. H., Chang, J.-C., Huang, S.-L., & Tsai, M.-H. (2013). Enhanced thermal conductivity and dimensional stability of flexible polyimide nanocomposite film by addition of functionalized graphene oxide. *Polymer International, 62*(5), 827-835.

Tu, K.-N. (2013). *Silicon and Silicide nanowires: Applications, fabrication, and properties*: Pan Stanford Publishing.

Tuan, H.-Y., Lee, D. C., Hanrath, T., & Korgel, B. A. (2005a). Catalytic solid-phase seeding of silicon nanowires by nickel nanocrystals in organic solvents. *Nano Letters, 5*(4), 681-684.

Tuan, H.-Y., Lee, D. C., Hanrath, T., & Korgel, B. A. (2005b). Germanium nanowire synthesis: An example of solid-phase seeded growth with nickel nanocrystals. *Chemistry of Materials, 17*(23), 5705-5711.

Van der Werf, C. H. M., van Veenendaal, P. A. T. T., van Veen, M. K., Hardeman, A. J., Rusche, M. Y. S., Rath, J. K., & Schropp, R. E. I. (2003). The influence of the filament temperature on the structure of hot-wire deposited silicon. *Thin Solid Films, 430*(1–2), 46-49.

Vincent, M., Kim, M. S., Carraro, C., & Maboudian, R. (2012, Jan. 29 2012-Feb. 2 2012). *Silicon carbide nanowires as an electrode material for high temperature supercapacitors.* Paper presented at the Micro Electro Mechanical Systems (MEMS), 2012 IEEE 25th International Conference on.

Wang, H., Gao, Q., & Jiang, L. (2011). Facile approach to prepare nickel cobaltite nanowire materials for supercapacitors. *Small, 7*(17), 2454-2459.

Wang, H., Song, H., Lin, Z., Jiang, X., Zhang, X., Yu, L., Xu, J., Pan, L., Wang, J., Zheng, M., Shi, Y., & Chen, K. (2016). Highly cross-linked Cu/a-Si core-shell nanowires for ultra-long cycle life and high rate lithium batteries. *Nanoscale, 8*(5), 2613-2619.

Wang, J., Chao, D., Liu, J., Li, L., Lai, L., Lin, J., & Shen, Z. (2014). Ni_3S_2@MoS_2 core/shell nanorod arrays on Ni foam for high-performance electrochemical energy storage. *Nano Energy, 7*, 151-160.

Wang, N., Cai, Y., & Zhang, R. Q. (2008). Growth of nanowires. *Materials Science and Engineering: R: Reports, 60*(1–6), 1-51.

Wang, Q., Luo, Q., & Gu, C. Z. (2007). Nickel silicide nanowires formed in pre-patterned SiO_2 trenches and their electrical transport properties. *Nanotechnology, 18*(19), 195304.

University of Malaya

Wang, R., & Yan, X. (2014). Superior asymmetric supercapacitor based on Ni-Co oxide nanosheets and carbon nanorods. *Scientific Reports, 4*, 3712.

Wang, W., Wang, Y., Gu, L., Lu, R., Qian, H., Peng, X., & Sha, J. (2015). SiC@Si core–shell nanowires on carbon paper as a hybrid anode for lithium-ion batteries. *Journal of Power Sources, 293*, 492-497.

Wang, Y., Schmidt, V., Senz, S., & Gosele, U. (2006). Epitaxial growth of silicon nanowires using an aluminium catalyst. *Nature Nanotechnology, 1*(3), 186-189.

Weng, B., Liu, S., Tang, Z.-R., & Xu, Y.-J. (2014). One-dimensional nanostructure based materials for versatile photocatalytic applications. *RSC Advances, 4*(25), 12685-12700.

Wiesmann, H., Ghosh, A. K., McMahon, T., & Strongin, M. (1979). a-Si : H produced by high-temperature thermal decomposition of silane. *Journal of Applied Physics, 50*(5), 3752-3754.

Williams, D. B., & Carter, C. B. (2009). The transmission electron microscope. In *Transmission Electron Microscopy: A Textbook for Materials Science* (pp. 3-22). Boston, MA: Springer US.

Xiao-Yong, X., Sheng-Rui, X., Jin-Cheng, Z., Zhi-Yu, L., Jun-Cai, M., Zi-Yang, L., Jun-Shuai, X., & Yue, H. (2012). Temperature dependences of Raman scattering in different types of GaN epilayers. *Chinese Physics B, 21*(2), 027803.

Xinhui Xia, J. T., Yongqi Zhang, XiuliWang, Changdong Gu, Xin-bing Zhao, and HongJinFan. (2012). High-quality metal oxide core/shell nanowire arrays on conductive substrates for electrochemical energy storage. *ASC Nano, 6*, 5531–5538.

Yan, J., Khoo, E., Sumboja, A., & Lee, P. S. (2010). Facile coating of manganese oxide on tin oxide nanowires with high-performance capacitive behavior. *ACS Nano, 4*(7), 4247-4255.

Yan, R., Gargas, D., & Yang, P. (2009). Nanowire photonics. *Nature Photonics, 3*(10), 569-576.

Yang, M.-R., Chu, S.-Y., & Chang, R.-C. (2007). Synthesis and study of the SnO_2 nanowires growth. *Sensors and Actuators B: Chemical, 122*(1), 269-273.

Yang, N., Zhuang, H., Hoffmann, R., Smirnov, W., Hees, J., Jiang, X., & Nebel, C. E. (2012). Electrochemistry of nanocrystalline 3C silicon carbide films. *Chemistry – A European Journal, 18*(21), 6514-6519.

Yang, S., Wang, L., Wang, Y., Li, L., Wang, T., & Jiang, Z. (2015). Identification and characteristics of ZnO/MgO core-shell nanowires. *AIP Advances, 5*(3), 037122.

Yu, H., Han, J., Zhu, J., & Cao, W. (2013). Catalytic synthesis of crystalline SiC nanowires from a Ni/a-C/Si sandwich configuration. *CrystEngComm, 15*(23), 4655-4659.

University of Malaya

Yu, L., O'Donnell, B., Alet, P.-J., Conesa-Boj, S., Peiro, F., Arbiol, J., & i Cabarrocas, P. R. (2009). Plasma-enhanced low temperature growth of silicon nanowires and hierarchical structures by using tin and indium catalysts. *Nanotechnology, 20*(22), 225604.

Yu, M., Zeng, Y., Zhang, C., Lu, X., Zeng, C., Yao, C., Yang, Y., & Tong, Y. (2013). Titanium dioxide@polypyrrole core-shell nanowires for all solid-state flexible supercapacitors. *Nanoscale, 5*(22), 10806-10810.

Yu, Z., Tetard, L., Zhai, L., & Thomas, J. (2015). Supercapacitor electrode materials: Nanostructures from 0 to 3 dimensions. *Energy & Environmental Science, 8*(3), 702-730.

Yuan, D.-s., Zhou, T.-x., Zhou, S.-l., Zou, W.-j., Mo, S.-s., & Xia, N.-n. (2011). Nitrogen-enriched carbon nanowires from the direct carbonization of polyaniline nanowires and its electrochemical properties. *Electrochemistry Communications, 13*(3), 242-246.

Zhang, G. Q., Wu, H. B., Hoster, H. E., Chan-Park, M. B., & Lou, X. W. D. (2012). Single-crystalline $NiCo_2O_4$ nanoneedle arrays grown on conductive substrates as binder-free electrodes for high-performance supercapacitors. *Energy & Environmental Science, 5*(11), 9453-9456.

Zhang, J., Jia, Q., Zhang, S., Huang, J., & Zhang, S. (2016). One-step molten-salt-mediated preparation and luminescent properties of ultra-long SiC/SiO_2 core–shell nanowires. *Ceramics International, 42*(2), 2227-2233.

Zhang, K., Zeng, W., Zhang, G., Hou, S., Wang, F., Wang, T., & Duan, H. (2015). Hierarchical $CuCo_2O_4$ nanowire@$NiCo_2O_4$ nanosheet core/shell arrays for high-performance supercapacitors. *RSC Advances, 5*(85), 69636-69641.

Zhang, Q., Chen, H., Wang, J., Xu, D., Li, X., Yang, Y., & Zhang, K. (2014). Growth of hierarchical 3D mesoporous $NiSi_x/NiCo_2O_4$ core/shell heterostructures on nickel foam for lithium-ion batteries. *ChemSusChem, 7*(8), 2325-2334.

Zhang, Y., Chen, J., Fan, H., Chou, K. C., & Hou, X. (2015). Characterization of modified $SiC@SiO_2$ nanocables/MnO_2 and their potential application as hybrid electrodes for supercapacitors. *Dalton Trans, 44*(46), 19974-19982.

Zhao, F. F., Zheng, J. Z., Shen, Z. X., Osipowicz, T., Gao, W. Z., & Chan, L. H. (2004). Thermal stability study of NiSi and $NiSi_2$ thin films. *Microelectronic Engineering, 71*(1), 104-111.

Zhou, W., Yan, L., Wang, Y., & Zhang, Y. (2006). SiC nanowires: A photocatalytic nanomaterial. *Applied Physics Letters, 89*(1), 013105.

Zhu, Q., Zhang, Z., Sun, Z., Cai, B., & Cai, W. (2016). Importance of cations and anions from control agents in the synthesis of silver nanowires by polyol method. *Applied Physics A, 122*(6), 618.

University of Malaya

Zhuang, H., Yang, N., Zhang, L., Fuchs, R., & Jiang, X. (2015). Electrochemical properties and applications of nanocrystalline, microcrystalline, and epitaxial cubic silicon carbide films. *ACS Applied Materials & Interfaces, 7*(20), 10886-10895.

Zou, R., Yuen, M. F., Zhang, Z., Hu, J., & Zhang, W. (2015). Three-dimensional networked $NiCo_2O_4/MnO_2$ branched nanowire heterostructure arrays on nickel foam with enhanced supercapacitor performance. *Journal of Materials Chemistry A, 3*(4), 1717-1723.

University of Malaya

LIST OF PUBLICATIONS AND PAPERS PRESENTED

[1] **Najwa binti Hamzan**, Farah Nadiah Binti Nordin, Saadah Abdul Rahman, Huang Nay Ming and Goh Boon Tong. (2015). Effects of substrate temperature on the growth, structural and optical properties of NiSi/SiC core – shell nanowires. *Applied Surface Science*, 343, 70–76.

University of Malaya